8-2023

Experimental and numerical studies of laser powder-bed fusion process with ti-6al-4v powder: (1) porosity and mechanical properties, and (2) transient phenomena in one- and two-dimensional fabrications.

Santosh K. Rauniyar
University of Louisville

EXPERIMENTAL AND NUMERICAL STUDIES OF LASER POWDER-BED FUSION PROCESS WITH TI-6AL-4V POWDER: (1) POROSITY AND MECHANICAL PROPERTIES, AND (2) TRANSIENT PHENOMENA IN ONE- AND TWO-DIMENSIONAL FABRICATIONS

By

Santosh K. Rauniyar

A Dissertation
Submitted to the Faculty of the
J.B. Speed School of Engineering of the University of Louisville
in Partial Fulfillment of the Requirements
for the Degree of

Doctor of Philosophy
in Industrial Engineering

Department of Industrial Engineering
University Of Louisville
Louisville, Kentucky, USA

August 2023

EXPERIMENTAL AND NUMERICAL STUDIES OF LASER POWDER-BED FUSION PROCESS WITH TI-6AL-4V POWDER: (1) POROSITY AND MECHANICAL PROPERTIES, AND (2) TRANSIENT PHENOMENA IN ONE- AND TWO-DIMENSIONAL FABRICATIONS

By

Santosh K. Rauniyar

A Dissertation Approved on

August 09, 2023

By the following Dissertation Committee:

_____
Dissertation Director: Dr. Kevin Chou

_____
Dr. Thomas L. Starr

_____
Dr. Li Yang

_____
Dr. Erin Gerber

DEDICATION

This dissertation is dedicated to my parents

Shiv Rauniyar and Mira Rauniyar

for their continuous support and unwavering encouragement.

ACKNOWLEDGEMENTS

First and foremost, I wish to express my deepest appreciation to my esteemed advisor, Dr. Kevin Chou, for his continuous guidance and mentorship throughout this study. Through his expertise, support, and motivation, I have developed a better understanding of research activities and additive manufacturing.

I am indebted to the members of my committee, Dr. Thomas Starr, Dr. Li Yang and Dr. Erin Gerber for their time, feedback, and support during this project.

I would like to extend my appreciation to the National Institute of Standards and Technology (70NANB16H029), the Small Business Technology Transfer program (18-009 N68335-18-C0371 and N68335-21-C-0168), and the National Science Foundation (1921263) for their financial assistance at various stages of my research.

I also want to acknowledge and thank my fellow lab mates, Dr. Subin Shrestha, Aref Vali, Dr. Shanshan Zhang, Dr. Ben Fotovvati, Dr. Ethan Le and Nismath VH, whose camaraderie and encouragement have been instrumental in shaping my research and making the journey enjoyable.

I am grateful for the opportunity to utilize the equipment in the AMIST lab as well as the assistance from the faculty and administrative staff of the Industrial Engineering department during my doctoral program.

I am deeply thankful to my parents, Shiv Rauniyar and Mira Rauniyar, for their unwavering love and support. I am grateful to my siblings, Ramita Rauniyar and Ramanuj Rauniyar, for their companionship and valuable advice throughout this journey. I would like to thank my brother-in-law Birendra Rauniyar for his words of encouragement.

I am also indebted to all those who have knowingly and unknowingly aided me during my time at the University, helping me work towards the achievement of this Ph.D. degree.

ABSTRACT

EXPERIMENTAL AND NUMERICAL STUDIES OF LASER POWDER-BED FUSION PROCESS WITH TI-6AL-4V POWDER: (1) POROSITY AND MECHANICAL PROPERTIES, AND (2) TRANSIENT PHENOMENA IN ONE- AND TWO-DIMENSIONAL FABRICATIONS

Santosh Kumar Rauniyar

August 09, 2023

Laser powder bed fusion (L-PBF) process represents a form of metal additive manufacturing (AM) where micron-level powdered material is selectively melted and fused layer by layer to create intricate three-dimensional parts. This process involves rapid melting and solidification, leading to intense thermocapillary convection within the molten pool. The melt pool is a crucial element of the L-PBF process and refers to the localized region where the powder particles are melted and solidified to form each layer of the printed part. The shape and dimensions of the melt pool directly influence the accuracy and surface finish of the printed part. Precise control of the melt pool geometry is essential for achieving the desired dimensions and avoiding defects in the final part. Optimizing process parameters and achieving high-quality printed parts require a deep understanding of the dynamics governing the melt pool. In this regard, both experimental and simulation

methods were employed to study the melt pool geometry and its variations, considering various parameter combinations and different length scales. The printed parts were also examined for defects like porosity and to analyze their surface characteristics.

The study started with an initial implementation of a simplified three-dimensional model of a powder bed using ANSYS Fluent. The simulation setup was based on a custom user defined function that integrated a volumetric heat source, temperature-dependent material properties, and volume of fluid method for identifying the free surface. The simulation setup was then employed to investigate the impact of varying powder size distributions on the formation of a melt pool. The results show that the size and distribution of particles in the powder mixture play a crucial role in shaping the evolution and geometry of the molten pool. Smaller particles encourage a consistent and uninterrupted flow within the molten pool. However, the presence of voids promotes fluid convection in the downward direction, leading to a temporary increase in the depth of the molten pool. This finding highlights the importance of understanding the role of particle size and distribution in shaping the characteristics of the melt pool during the L-PBF process.

The evolution of the melt pool in the L-PBF process is closely related to pore formation in the final printed parts. Porosity refers to the presence of voids or empty spaces within the printed parts during the AM processes. Several factors related to melt pool dynamics, such as insufficient energy input, balling phenomenon, insufficient overlapping, gas entrapment, and overheating can contribute to pore formation. When the energy density is high, there is a possibility of forming keyhole pores. This occurs when excessive energy input from the laser causes deep penetration of the molten material into the powder bed, resulting in an elongated shape cavity resembling a keyhole shape. Multiple tensile

coupons were printed with various parameters to understand pore morphology before and after fracture. A non-destructive technique of micro-CT scan method was utilized to analyze the porosity. The findings indicate that the energy density and build orientation significantly influence the porosity of the as-built printed samples, while the impact of the location change is observed to be minimal. After undergoing tensile testing, the samples exhibit a notable increase of more than nine percent in both pore volume and porosity percentage compared to their initial as-built counterparts. These results emphasize the importance of carefully controlling energy input and optimizing build orientation to mitigate porosity and enhance the quality of L-PBF printed parts.

During the L-PBF process, a laser with a spot size ranging in the hundreds of microns interacts with metal powder to form tracks. The laser follows predefined scan paths in each layer, and the behavior of the melt pool during each scan is heavily influenced by the laser power and scan speed. The melting process can occur in three modes: incomplete melting, conduction mode melting, and keyhole mode melting, depending on the combination of these two parameters. Only conduction and keyhole mode melting result in the formation of continuous and complete tracks. The length of the scan determines whether the scanned track reaches a quasi-steady state or not. Regardless of the laser power and scan speed values used, a transient region exists at the start and end of long scan vectors. The melt pool geometry in this transient region displays distinct characteristics compared to the quasi-steady region in the middle. The physics of the melt pool dynamics in these transient states remain largely unexplored. Understanding the characteristics of the melt pool in the transient region is essential to ensure the quality of smaller-dimensional parts in the L-PBF process. Improving our knowledge in this area can

lead to better control over the printing process and enhanced quality of the final printed components.

The research involved conducting experiments on one-dimensional line scans, referred to as single tracks, using an extensive design of experiment (DOE) approach for process parameters and multiple replicates with several builds. The surface data from these as-built tracks were collected using a non-contact optical profilometer, the WYKO NT1100. The analysis of the single tracks revealed that the track width and surface height varied along the scan line. Particularly, the track width at both the start and end of the track demonstrated distinct characteristics with significant fluctuations. The region in the middle, referred to as quasi-steady region, showed uniform width with relatively low variation. The transient and quasi-steady regions were quantified based on the track width variations along the scan line. Additionally, the length of the transient region was not constant for all the parameters but varied with power and scan speed settings. The analysis results show that the transient length at the start ranged from 300 microns to 1400 microns, for the power and scan speed values used in the experiment.

Following the analysis of results from the single track experiment, the research progressed to fabricating two-dimensional raster-area scans. The findings of the single track experiment were integrated into the experimental setup of the raster scans to refine the DOE. The two-dimensional prints incorporated extra process parameters like hatch spacing and the number of scan lines. The results show that the parameters that resulted in larger transient regions for raster scans also resulted in higher surface roughness. The shorter scan lengths which only consisted of transient zones resulted in higher surface roughness and the increasing scan length reduced the average roughness. In addition to

examining the surface characteristics of the transient region, another set of experiments was conducted to analyze the surface roughness of raster scans in the quasi-steady regions. This experiment involved assessing the impact of process parameters, including laser power, scanning speed, and hatch spacing, on the surface characteristics of single-layer raster scan areas through the design of experiment and multiple replicates. The result revealed that raster scan areas with lower laser power, higher scanning speed, and higher hatch spacing have higher surface roughness. Moreover, among the three main parameters, laser power played the most significant role in determining the surface roughness value.

TABLE OF CONTENTS

LIST OF TABLES

LIST OF FIGURES

CHAPTER 1

INTRODUCTION

1.1 Background and Motivation

Laser Powder Bed Fusion (L-PBF), alternatively referred to as Selective Laser Melting, Direct Laser Metal Sintering or Laser Cusing is a metal based additive manufacturing process. The process initiates with the disintegration of the CAD model into numerous thin layer details, which are consecutively fed into the L-PBF machine. The layer-by-layer process involves scanning, melting, solidification, and ultimately produces a fully functional part. The powder melting process is a complex phenomenon, during which heat and mass transfer occurs [1]. In addition, the continuous localized heating and cooling of the powder bed lead to evolution of residual stress.

L-PBF process has been employed with numerous commercial metallic powders such asIn718, Ti6Al4V, AlSi10Mg, Mg-9%Al, Fe- Al , Fe-Ni, Fe-cr, Fe-Ni-Cu- P, 304 Stainless steel, 316L Stainless steel etc. It has emerged as one of the primary metal additive manufacturing technologies used for many applications including medical, cooling, automotive, and aerospace sectors. L-PBF offers a wide range of advantages over conventional manufacturing techniques like a near-net-shape production, direct production based on a CAD model, and a high level of flexibility. Moreover, the L-PBF process is

capable of producing complex geometrical features that cannot be fabricated using conventional manufacturing processes [2].

Several other additive manufacturing (AM) processes can be used for metal parts fabrication. The AM processes like Binder Jetting, Metal Extrusion, Sheet Lamination, Direct energy Deposition etc. can also be used for the fabrication of metal parts. Binder jetting (BJ) and Electron Beam Melting (EBM) processes uses powder as a raw material along with the L-PBF process. EBM process works in a controlled vacuum environment where the metal powder is melted by a powerful electron beam [3]. However, the working principle of BJ process is quite different from the powder bed fusion process (L-PBF and EBM). Instead of melting the powder particles, a conventional sintering mechanism is applied to fuse the adjacent powder particles with the application of thermal energy. The types of materials and alloys used in those processes are different due to the differences in their work principle. It is important to select the right process in the manufacturing of metal parts with specific materials. These processes have their own pros and cons. L-PBF process has high cooling rates, varying between ~104 and 106 Ks−1 [4]. In addition, the parts fabricated by the L-PBF process tend to show improved mechanical, tribological, and corrosion properties compared to their cast counterparts. EBM uses a hot bed and hence does not produce a fine microstructure like the L-PBF process [4]. L-PBF and EBM achieve a significantly finer microstructure due to faster cooling rates compared to the BJ process.

The mechanical properties and surface finish of the L-PBF part are highly influenced by process parameters such as powder layer thickness, powder particle size,

beam speed, and scanning strategy, among others. However, the qualitative and quantitative effects of all these parameters are not fully understood yet. The L-PBF process is associated with several commonly observed issues, including the buildup of thermal stress due to a high temperature gradient, part deformation, and delamination caused by high residual stress [5]. Despite the L-PBF process's significant potential as an additive manufacturing technique, its broad application is often hindered by the high thermal gradient and residual stress that occurs during the build process. Thus, to establish the L-PBF process as a reliable manufacturing process for functional parts, it is essential to have a better understanding of the process physics and precise control over process parameters.

Modeling and simulation provide a cost-effective alternative to expensive experimental investigations for understanding the process physics of the L-PBF. Numerical methods have been applied to model the process and capture the thermal response during the building process [7]. Simulation techniques have been developed to measure the residual stress distribution and part deformation resulting from the temperature gradient [8]. However, numerical analysis involves simplifications and approximations, and most of the research work on numerical simulation of the L-PBF process has been conducted under single-layer conditions to make computational work feasible and quick [8].

A typical L-PBF machine layout is shown in Figure 1.1, which is the assembly of the building platform, dispenser platform, collector platform, laser unit, mirror scanner, and recoater. The powder layer, generally 20 to 100μm thick, is spread over the build platform by a recoater blade. The dispenser platform unit ensures an even distribution of powder particles during each spreading of a powder layer. L-PBF machine then employs a

computer guided scanning laser beam as a heat source applied to selectively melt the powder particles. The powder layer spraying and scanning occurs simultaneously until the final dense part is obtained. L-PBF process should be run in an inert atmosphere which is maintained by either argon or nitrogen gas. Once the part is built, powder particles are removed from the build platform and the build plate with the attached part is taken out.

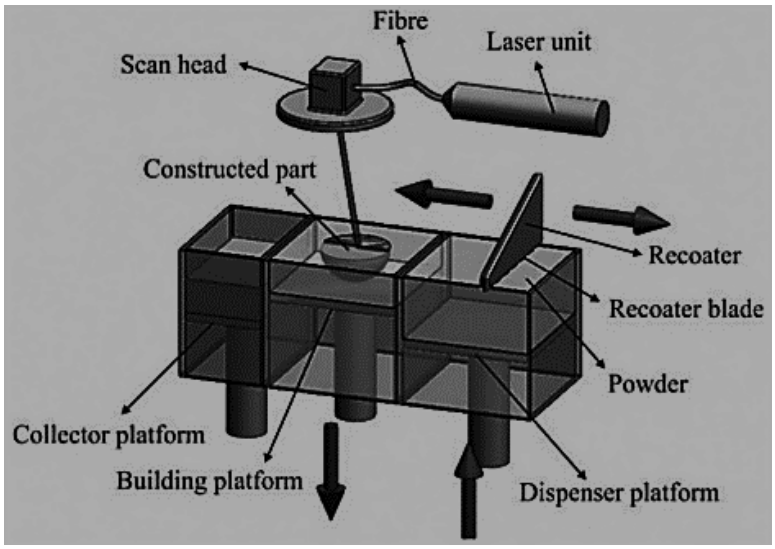

Figure 1.1 A typical L-PBF process [9].

1.2 Research Objective and Scope

L-PBF is a highly versatile AM technique for producing complex metal components directly from CAD model, without expensive tooling, and with minimal material waste. Advances in AM technologies have made it possible to fabricate thin and micron level structures with high strength. AM process can be used to print lightweight cellular structures that feature intricate designs and small dimensions. These structures hold great promise for a variety of engineering applications, ranging from biomedical implants

to aerospace parts. However, ensuring quality and repeatability of parts produced through the L-PBF process can be challenging. There are multiple variable process parameters in any L-PBF machine including laser power, scan speed, laser spot size, and others. The use of a combination of the different process parameters will result in a unique temperature cycle within the build during the print. The thermal cycle within the build during fabrication will also affect the microstructure, residual stress, and defects distribution within the fabricated part. Understanding the thermal cycles at any combination of process parameters will help in selecting the best design process parameter for the desired quality and microstructure. The change in just one parameter can lead to a significant difference in the quality.

In addition, the melt track for long passes shows different characteristics at the start, the middle and at the end. The melt pool geometry will reach a quasi-steady state, with less variations, after the laser beam travels a certain distance given that the scanning direction is unchanged. The geometry of the melt track at the start and at the end of a long scan have distinct characteristics compared to the quasi-steady state in the middle. In addition, the laser beam goes through a phase of acceleration or deceleration at turn points at which the melt pool exhibits different properties. There is a lack of comprehensive research examining the geometry and characteristics of the melt pool for short scans. This study aims to enhance the understanding of this topic through the evaluation of one-dimensional line scans and two-dimensional raster-area scans.

This study represents an initial effort to investigate the size effect in producing small, structures of reliable quality using Ti-6Al-4V (Ti64) powder material

through metal laser powder bed fusion process. The experiment was carried out in an EOS M270 machine with a range of process parameters. Discrete element method and thermo-fluid simulation work was performed using both freeware and commercially available software. Surface properties of the samples were assessed using optical interferometry, while micro-CT was employed to analyze the porosity of the printed samples. This study provides qualitative and quantitative difference between short and long scans.

The recoating process is simulated using an open-source variant of the LIGGGHTS software, employing the discrete element method to generate the distribution of the powder bed. The powder distribution from the DEM simulation was exported to the thermo-fluid setup in Fluent and Flow3D. The initial phase of the computational work involves the utilization of user-defined functions (UDFs) within ANSYS Fluent. Subsequently, in the later chapters, a high-fidelity Volume of Fluid (VOF) model is developed in FLOW-3D. This advanced model incorporates complex physics such as the Marangoni effect, recoil pressure, and evaporation, multiple reflections, and temperature depended properties for the powder material to generate a comprehensive understanding of the laser to metal interaction. The melt pool geometry from simulation on a single track was contrasted with the experimental results. The model was used to preform simulation of single tracks, raster scans, and multi-layer cases.

The layout of this proposal is mentioned below:

In Chapter 2, an extensive review of the literature is provided, focusing on the L-PBF process. The review encompasses various process parameters, the utilization of

different materials in metal additive manufacturing, the occurrence of part defects in the built components, and the mechanical testing of the printed parts.

In Chapter 3, the focus is on the utilization of user-defined functions within the ANSYS Fluent software. These UDFs are employed to delve into the behavior of the melt pool across varying particle size ranges. The study specifically investigates the changes observed in the melt pool when employing three distinct particle size ranges of powder particles during the creation of single tracks. All of these tracks are subjected to identical process conditions, allowing for a comparative analysis of the melt pool characteristics.

In Chapter 4, an in-depth examination is conducted on the porosity of tensile coupons that are manufactured utilizing three different power levels and two distinct scan speeds. The chapter provides insights into the variations in porosity levels and the morphology of pores present in the tensile coupons, both before and after undergoing a tensile test.

Chapter 5 demonstrates the melt pool shape of a single track has distinct characteristics at the start, the middle, and the end. According to the study, the melt track reaches a quasi-steady state with reduced variations only after a certain length of scanning has been completed. The shape and variation in the melt pool geometry along the scan length is explored for different parameters.

In Chapter 6, the transient behavior in two dimensions along the x- and y-axis is thoroughly examined. This study specifically delves into the quasi-steady state of raster scanning, considering various hatch spacing scenarios. The results highlight the substantial impact of scan length on surface characteristics.

Chapter 7 of the study focuses on exploring the impact of parameters on the surface characteristics of single-layer raster scanning deposits. The primary objective of this chapter is to examine the relationship between the surface roughness of raster scans and the parameters involved in the L-PBF process through experimental work.

Chapter 8 presents the conclusion drawn from this study and also present the possible future research.

CHAPTER 2

LITERATURE REVIEW

2.1 Powder Characteristics

Powder property has a detrimental effect on the mechanical properties and microstructures of the parts. It will significantly impact on the spreading performance, the packing ability among others while, the quality of powder will affect the part's mechanical property and surface finish [10]. A typical SEM image of titanium alloy Ti-6Al-4V powder is shown in Figure 2.1 (a). Generally spherical or near spherical particles result in close packing of powder which leads to more efficient densification during the L-PBF process as shown in Figure 2.1(b). Ti6Al4V powder produced by plasma atomization with particle size between 5 and 50μm have been used for the L-PBF process [2] and In718 particles produced by argon gas atomization with average particle size of 26 μm, 45μm [11].

Table 2.1 shows the chemical composition of In718 super alloy, which is one of the popular alloys for the L-PBF process [12]. Powder density, which is also an important factor, usually depends upon the particle size variation in the powder sample. Specifically for Inconel 718, the powder density is around 60% of the bulk density. Typically, Inconel 718 super alloy has been developed and applied in wrought, cast and powder metallurgy forms. The Inconel 718 parts using these methods have demonstrated the superior mechanical properties and performances [12].

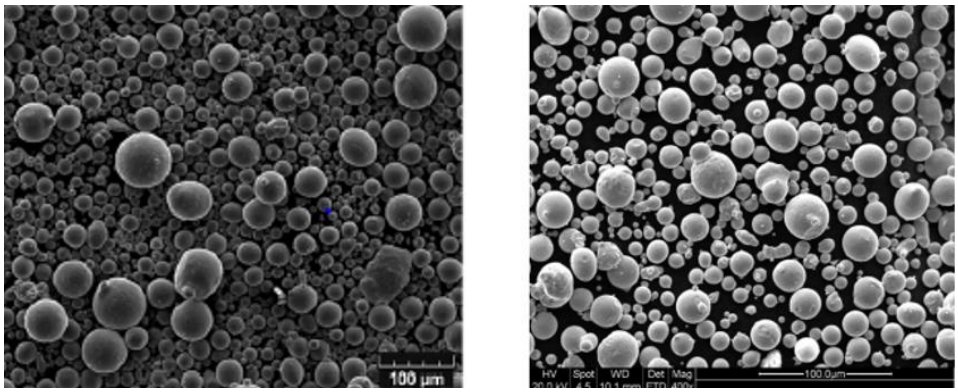

Figure 2.1 (a) Powder Morphology of Ti6Al4V[13] and (b): Powder Morphology of Inconel 718 [14].

Table 2.1 Inconel 718 powder composition [12].

Element	C	Cr	Mo	Al	Ti	Fe	Nb	Ni
Wt%	0.025	18.2	3.1	0.29	0.9	18.9	5.1	Balance

There is difference in particle size distribution for new and recycled versions of powder as shown in figure. L-PBF powder contains large amount of coarse particles even after recycling [15]. This may be due to smallest particles being dusted away in the gas stream during the building process [15]. Particle size distribution for new and recycled powders for the L-PBF process are shown in Figure 2.2.

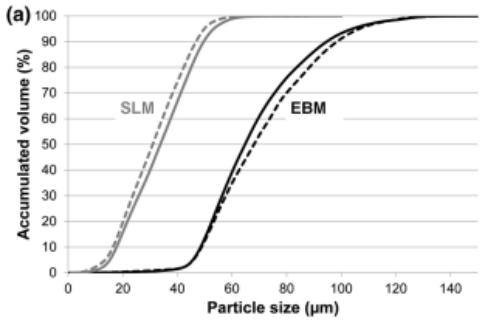

Figure 2.2 Particle size distribution; dotted line=new powder, full line=recycled powder.

2.2 Machines

The growth in the research interests of the L-PBF process has led to increase in the number of manufacturers of the L-PBF machines. The distribution of systems for 2014 is shown in Figure 2.3.

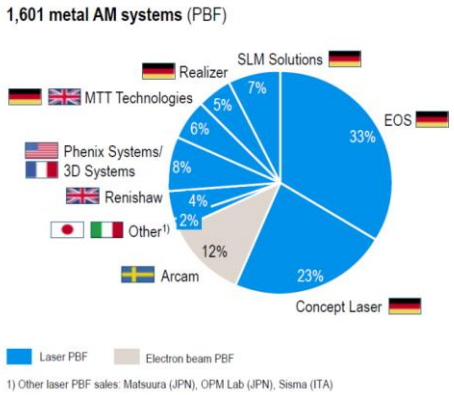

Figure 2.3 Metal AM systems market share by companies [16].

There is a constant increase in the number of research papers with keywords "selective laser melting" in Science Direct directory, the trademark name for the L-PBF process, from 2 in 2004 to 166 in 2016. [17] The rise in research interest has also been reflected with increase in the number of the L-PBF system sold as well as the increase in metal additive manufacturing market. This 2014 data shows that German manufacturers provide almost 70% of the machines for Powder Bed Fusion market sold worldwide.

2.3 Process Parameters

Process parameters should be controlled during the fabrication process. Generally, these factors are categorized into four main sets [18]. Laser-related parameters determine the amount of energy required for fabrication process. Scan-related parameters characterize

the fabrication speed and thermal distortion during the fabrication process. Powder-related factors also contribute to the mechanical properties and final part quality. Temperature-related parameters determine the key factors to ensure that the manufacturing chamber temperature is uniform and under control. Figure 2.4 depicts the major process parameters of the L-PBF process. Table 2.2 describes each factor's contribution to the fabrication process. It should be emphasized that some of these factors interact together and this interaction should be controlled for fabrication process.

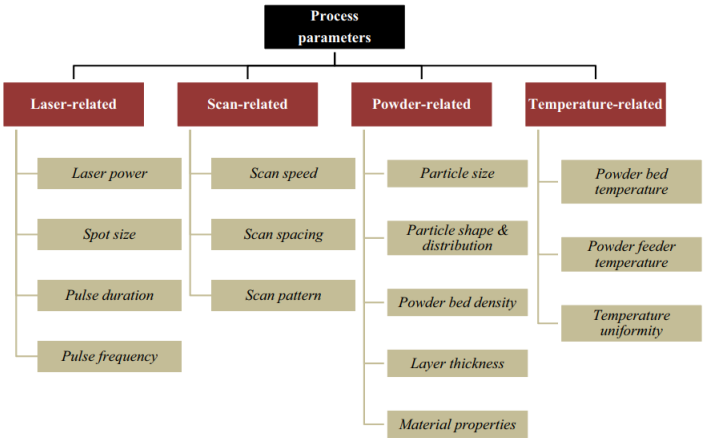

Figure 2.4 Controlling parameters in the L-PBF process [18].

Following Table 2.2 describes the factors in more detail:

Table 2.2 Description of the parameters.

Number	Category	Parameter	Description
1	Laser-related Parameters	Laser power	Laser power defines the amount of energy that emits to the particles during the fabrication process

2		Spot size	Spot size determines the resolution of the process
3		Pulse durations	Pulse duration controls the degree of the sintering required for the powder
4		Pulse frequency	Fabrication speed is defined by the frequency of the pulses
5	Scan-related Parameters	Scan speed	Scan speed specifies the overall fabrication speed
6		Scan spacing	In order the minimize thermal distortion on the powder bed a certain space should be applied to the scanning spots
7		Scan pattern	Scan pattern or scan strategy is contributing to the internal structure of the part
8	Powder-related Parameters	Particle size	Particle size defines the surface quality of the fabricated parts
9		Particle shape & distribution	Particle shape and distribution is related to the morphology of the powder
10		Powder bed density	Density is the main indicator of the finial mechanical properties of the powder

11		Layer thickness	Layer thickness usually is in the range of 20 to 50 micron which defines the accuracy of the part features
12	Temperature-related Parameters	Powder bed temperature	A certain pre heat should be applied to the powder to decrease the thermal distortion during the fabrication process
13		Powder feeder temperature	Powder feeder needs to have constant temperature with the in bed powder
		Temperature uniformity	The uniformity of the temperature should be maintained in entire build chamber to reduce the applied thermal stress

L-PBF is a complex process which involves dynamical phenomena driven by a time dependent temperature profile [19]. We can understand the process by either in-situ sensing or through computational methods. L-PBF process is accompanied by high thermal stresses caused by Temperature Gradient Mechanism (TGM). Therefore, it is important to detect the thermal distribution and deformation in the earliest possible stage since this causes the part to fail. In recent years, researchers have developed sensors for monitoring of the laser beam and delivery optics, chamber pressure, melt pool temperature and dynamics, optical emissions and substrate temperature [20]. It is possible to map the melt pool data (intensity,

area, length, and width) on the build plane. Figure 2.5 shows the optical set-up of the melt pool monitoring system developed by LM-Q machine of KU Leuven [21].

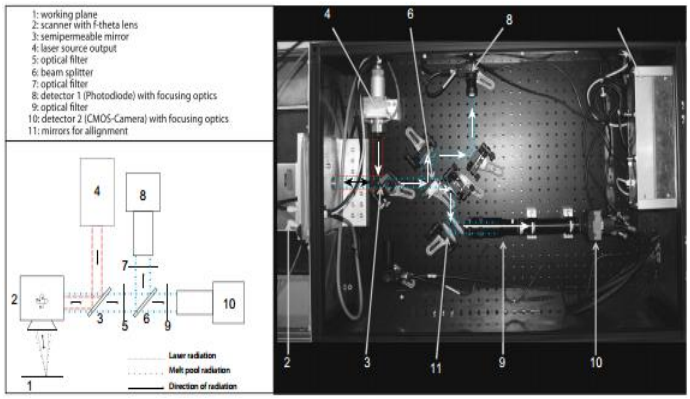

Figure 2.5 Optical setup of the monitoring system[2].

The reliability of the in situ quality control (observed data) has been demonstrated by comparing with the experimental data (actual defects) after manufacturing parts of Ti6Al4V, ALSi10Mg and NiTinol. This system in combination with the feedback control can improve the quality of down-facing surfaces in overhang structures where melt pool is located above loose metal powder region having lower thermal conductivity [22].

A control methodology is successfully used to improve surface finish of an overhang in a metal part from the feedback [9]. A photodiode sensor in a Lagrangian monitoring modality is used a first-generation feedback control system for a laser melting process that dynamically adjusts laser power based on photodiode response. It gives a promising result and prompts to research for other process conditions and geometries to determine how generally it may be applied [9].

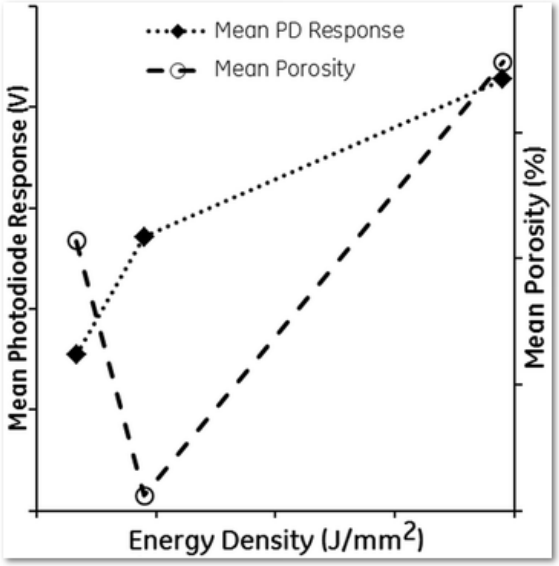

Figure 2.6 Photodiode response and sample porosity vs energy density in a laser melting process at GE Aviation.

It is expensive and time consuming to rely solely on experimental trial-and-error to guide the additive manufacturing effort. The scientific community applies numerical methods to create models of the consolidation process and validate against the experiment. The majority of these numerical approaches undertaken are for fundamentally homogeneous models [23]. Modeling and simulation capability have been validated in capturing the process physics of the L-PBF process [24]. Modeling and simulation of the L-PBF process can be used to predict the temperature distribution and melt pool shapes. Figure 2.7 shows the temperature distribution during scanning of single track [7]. Numerical model have also been used to predict residual stress and deformations. The surface morphology of the L-PBF produced parts has also been compared to simulated results to show the scope of simulation to understand the process physics of the L-PBF process [9].

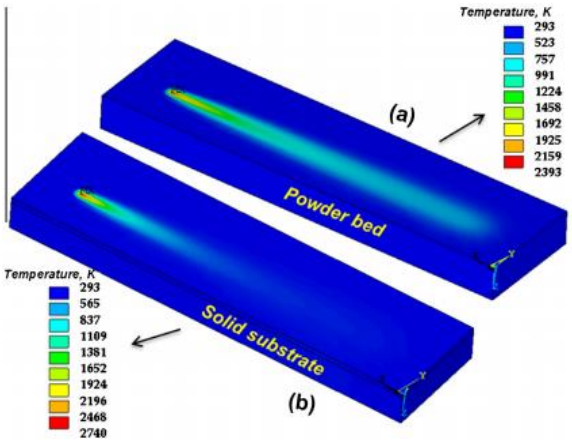

Figure 2.7 Temperature distribution obatined for a L-PBF simulation.

Process map helps to compare the process parameters and better understand the L-PBF process. The process map over entire range of experimented laser powers and scanning speed have been made by Song et. al. [25]. Three processing windows could be summarized based on the melting mechanisms: melting with cracks, continuous melting and partial melting. A perfect Ti6Al4V part has been succesfully manufactured by the L-PBF using parameters (v=0.4m/s, P=110W) within zone II as shown in Figure 2.8. The figure show three zonesi.e., zone I-melting with cracks, zone II-continuous melting, zone III-partial melting) versus laser power and scanning speed.

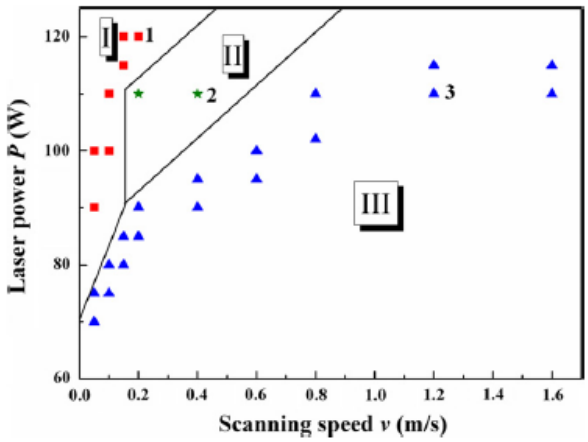

Figure 2.8 Mechanisms of single tracks for selective laser melted Ti6Al4V.

Figure 2.9 summarizes the process process parameters effect on properties of the L-PBF Mg-9%Al powder mixture [6]. The results indicated that maximum relative density of 82% can be obtained with parameters v=0.02 m/s and P=15 W.

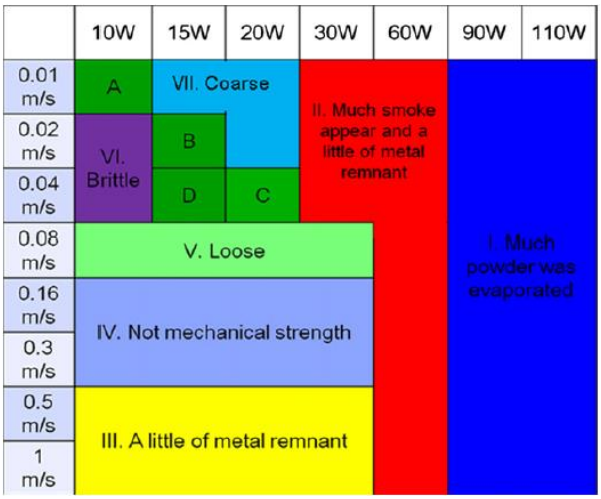

Figure 2.9 Process map for Mg-Al, results as a function of the range of laser powers and scan speeds.

2.4 Material

A majority research effort in fabricating L-PBF parts are based on steel, iron, and titanium related alloys [26]. However ceramics, composites, and polymers were subjected to more investigation in this area. Figure 2.10 presents the statistics of the research efforts with respect to material type on L-PBF. The popularity of Titanium alloys and steel-based alloys comes from their adoption in high value-added industries such as aerospace and medicine [26]. Investigated materials in L-PBF could be classified into three major clusters. Metals are the most widely used materials in L-PBF. Titanium alloys, Iron alloys, stainless steel alloys and nickel based alloys are the mostly practiced sets in L-PBF.

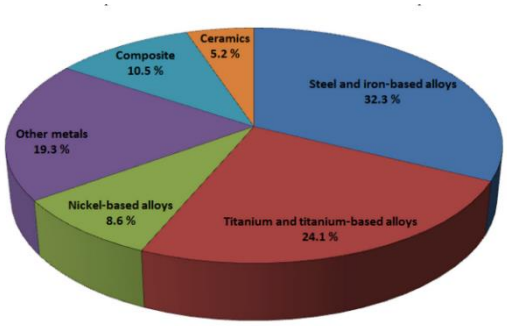

Figure 2.10 Research publications on L-PBF of various materials [26].

Several efforts have been taken to adopt ceramics for the L-PBF process. Alumina and Zirconia as well as Calcium and Silicon composites were the investigating materials for L-PBF process [27]. Although, some parts have been fabricated with the L-PBF process following are the main challenges in build ceramic parts with this manufacturing process [27]:

1. Ceramic parts that were fabricated with L-PBF exhibited rather high porosity. It is due to the incomplete fusion of ceramics particles in L-PBF process. Also entrapment of air bubbles is another contributing factor in ceramics fabrication. Consequently, the low density of these parts led to inadequate strength in final parts.
2. Inadequate surface quality of the parts were a major issue compared to binder jetting or Stereolithography (SLA) fabricated parts. Sintering profile adopted in furnace generates complete sintering for particles and this phenomena creates a more smooth surface finish for the parts.
3. High sintering and melting point of ceramics is another major issue in parts fabrication. Ceramics have two or three times higher sintering or melting point compared to the metals. Due to this, build chamber should be also capable of tolerating high temperature operations. This characteristic considerably increase the cost required for ceramic fabrication.
4. Low ductility of ceramics asserts lower scan speed for ceramic fabrication. Since ceramics are generally brittle materials, high fabrication speed introduces cracking in the parts. Consequently, a low scan speed is required to prevent breaking of the parts.

There also has been some attempts to fabricate polymers with L-PBF process. L-PBF polymer fabrication parts showed comparable mechanical properties to injected parts [27]. Table 2.3 sums up the list of materials that were used in L-PBF fabrication process.

Table 2.3 Investigated materials in L-PBF process [27].

Material Category	Material
Metals	Fe-AI intermetallic
	Fe3Al
	Fe-Ni
	Fe-Ni-Cr
	Fe-Ni-Cu-P
	304L stainless steel
	316L stainless steel
	H20 tool steel
	M2 high speed steel
	Maraging steel
	Ultra high carbon steel
Ceramic	Li2o-Al2O3-SiO2 (LAS)
	AI2O3 Alumina
	Silica (SiO2)
	Yttria-Stabilized Zirconia (YSZ)
	Tri-Calcium-Phosphate (TCP)
	Alumina-Zirconia Mixture
	Dental Porclain
	Alumina-silica mixture
	Silicon Carbide
	Silicon Monoxide
Polymers	Acrylic styrene
	Polyamide (Nylon)

2.5 Final Parts Defects

Major defects in L-PBF parts are porosity, cracking, oxide inclusion, and loss of alloying elements [28]. One of the reasons for porosity is the insufficient fusion during the

sintering/melting process [28]. Insufficient fusion is a result of inadequate energy in emitted laser. Laser power, layer thickness, scanning rates, and scan spacing are the parameters which should be controlled to reduce the porosity [28]. Another possible mechanism for porosity is entrapped air during the fabrication process. A fast pace of sintering/melting process creates entrapped bubbles in the fabricated process. Also the evolution of melt pool have direct relationship with the formation of the bubbles.

Cracking is a result of quick thermal expansion and large solidification shrinkage [29]. This phenomena happens in high conductive metals such as aluminum. A high thermal difference between powder bed and absorbed energy is another contributing factor in formation of cracks [29]. Consequently, sufficient pre-heat is required for material formation.

Oxidization happens by promoting balling and disrupting inter-particulate coalescence/wetting across the laser sintered/melted layers [30]. Fabricating parts in inert gas is a key to eliminate oxidization issue for metals. In this case, a sealed fabrication chamber is required to control the flow of the inert gas.

Loss of alloying element happens when high energy of laser evaporates some of the alloy elements with low fusion points [31]. For example some alloys with low fusion points vaporize in an aluminum alloys during the laser scanning phase [31]. By controlling the beam power density distribution and pulse duration the temperature of the powder bed could be regulated.

CHAPTER 3

MELT POOL ANALYSIS AND MESOSCALE SIMULATION OF LASER POWDER BED FUSION PROCESS (L-PBF) WITH TI-6AL-4V POWDER PARTICLES

3.1 Introduction

Additive manufacturing (AM) has come a long way, transforming from a rapid prototyping to rapid manufacturing technology. It is anticipated that it will become a multibillion-dollar industry by the next decade [35]. The L-PBF process, one of the AM techniques, is quickly becoming one of the sought after processes in aerospace and biomedical industries. Interest in and research work using this technique have grown exponentially over the past few years. In particular, additive manufacturing technologies for metal have found their way into various sectors with applications in cooling and automotive parts, medical implants, and aerospace components. Various commercial metallic powders including Ti6Al4V, In718, AlSi10Mg, and 304 and 316L stainless steels are being produced and modified specifically for this process. However, new powder materials must undergo calibration tests before application, which is both costly and time consuming [36]. Such calibration is required to determine the optimal processing parameters considering the thermal properties of each material [37].

Modeling and simulation is an efficient substitute for experimental investigation, allowing understanding of the effect of process parameters on the L-PBF process. Use of numerical models to replicate the process provides enhanced understanding of the physical phenomena involved in such manufacturing techniques without actually producing any parts. Numerical models for laser–material interactions have been developed for laser beam welding since the 1980s [38]. Similar numerical methods have been utilized by researchers for the powder bed fusion process too. Although the physics of the LPBF process is similar to that of the laser beam welding process, the presence of powder particles adds significant complexity to the process [39]. Powder particles of different sizes also exhibit different absorbance properties. A Gaussian laser heat source has been used to model the L-PBF process [40]. Khairallah et al [41] used a laser ray-tracing method to model the heat source with greater accuracy. The randomness in the local distribution of particle sizes affects the heat transfer as well as the melt pool flow. The discrete element method (DEM) can be used to represent this distribution of powder particles with greater accuracy [42]. Furthermore, spreading the next layer of particles affects the bonding between two layers and the overall density of the part.

Due to the complexity of the L-PBF process, it is not possible to replicate the mutliphysics phenomena using a single numerical model. Different models and techniques are thus applied separately to study the process on macro ($> 10^{-3}$ m), meso (10^{-6} –10^{-3} m), and microscale (10^{-9} – 10^{-6} m). Some of the phenomena in the L-PBF process that have been simulated include the powder distribution, residual stresses, the temperature distribution, the melt pool flow, the effect of gas flow, and the microstructure. In the numerical model applied here, a mesoscale approach with mesh size of 5 lm was used to

simulate the thermal interaction and melt pool flow. Experimental work on the effect of the PSD on optimization of the process parameters was reported by Liu et al., [43] and Spierings et al. [44] compared the density of stainless steel 316L parts produced using different powder grades. Those studies showed that the PSD affects not only the flowability of the powder but also the density and surface finish of the final part.

In simple terms, the L-PBF process consists of repeated movement of a heat source over a metallic powder with diameter on the order of 10 μm, using various scanning patterns. Previous studies considered a single scan track to be representative of the process, to understand the process physics and melt pool flow dynamics [41, 45]. The same approach is applied here, using a model consisting of a layer of metallic powder over a thick substrate. The DEM method is used to generate a layer of spherical powders with thickness of 60 μm. Powder particles with PSD from 0 μm to 25 μm, 0 μm to 45 μm, and 15 μm to 45 μm were generated with identical parameters. The powder and substrate material are both Ti-6Al-4V.

3.2 Numerical Modeling

3.2.1 Powder distribution modeling

A 3D model with domain size 2500 μm × 600 μm × 1000 μm was created to obtain a random powder distribution of the powder bed on the build plate of a metal 3D printing machine. The powder size range shown in Figure 3.1 is referenced from AP&C, A GE additive company's brochure. Powder particles with 15 different particle diameters were created in each of the three size ranges based on their proportions. A sequential powder

addition algorithm was used to drop a constant number of particles in bulk into the domain as shown in Figure 3.2, which were then allowed to settle under gravity.

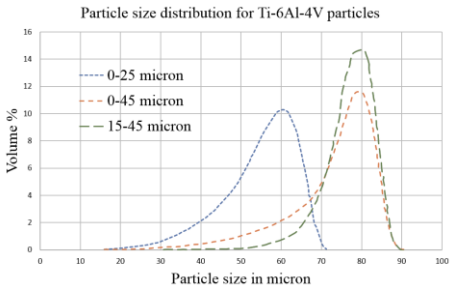

Size range	*0-25 µm*	*0-45 µm*	*15-45 µm*
Morphology	*Spherical*	*Spherical*	*Spherical*
Size distribution	*µm*	*µm*	*µm*
d10	*8*	*14*	*20*
d50	*15*	*32*	*34*
d90	*24*	*47*	*46*

Figure 3.1 Particle size distribution for different categories (graphical representation and tabular data) [46].

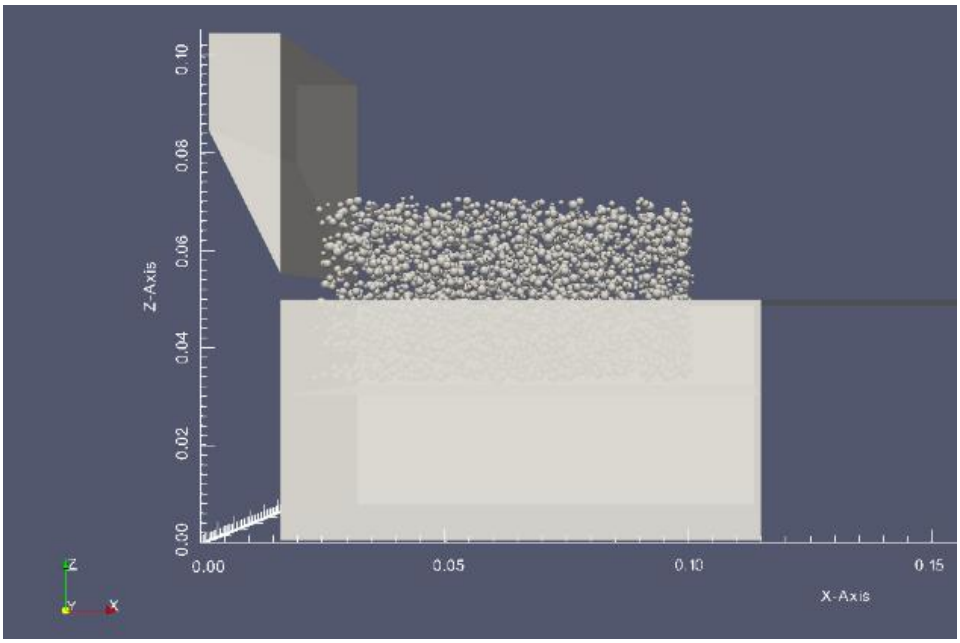

Figure 3.2 Side view of particle addition in bulk.

Once the particles had settled, the bottom platform (collector) will move up and the recoater will spread the particles in the positive X-direction, as shown in Figure 3.3. The result for the three different powder size distributions is quite different. The powder with size range of 0–25 µm shows comparatively less void space because the particles of smaller

diameter fill in the void space, as shown in Figure 3.4. The particles with size range of 0–45 µm and 15–45 µm showed a similar distribution of powder particles, but with more void space in between the particles.

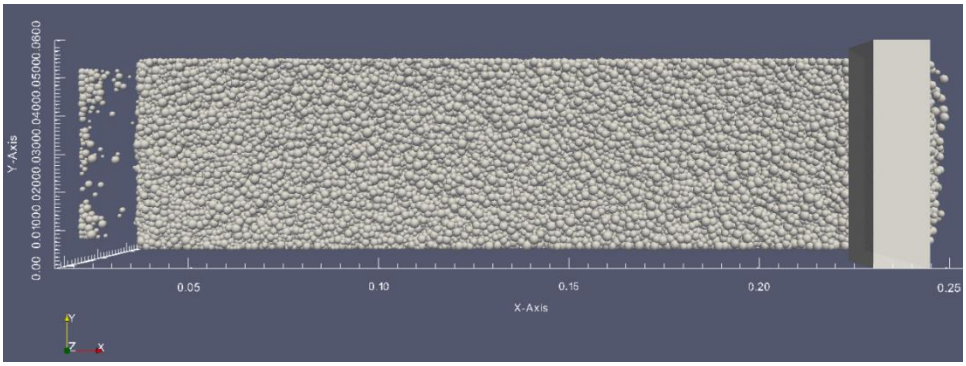

Figure 3.3 Top view of the domain with the powder spread.

(a) **(b)** **(c)**

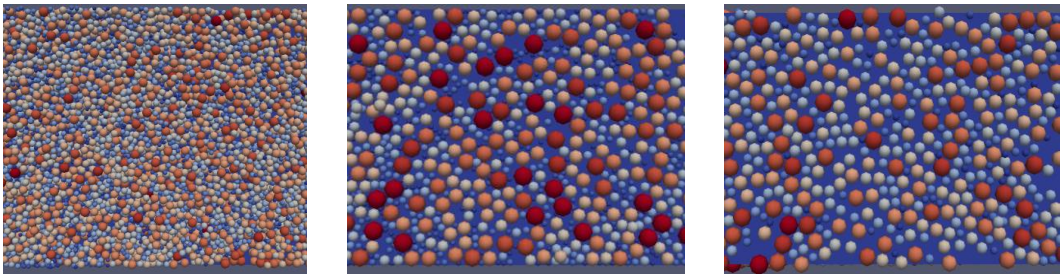

Figure 3.4 Zoomed view of generated powder layer (a) 0-25 µm, (b) 0-45 µm, and (c) 15-45 µm.

3.2.2 Equations for heat transfer and fluid flow

A conical volumetric heat source was modeled, as given in equation 1, to represent the heat energy from the laser. It is important to identify the free surface in the mesh-based simulation to apply the appropriate volumetric heat source. Since there are two phases in the model, viz. gas as phase 1 and Ti-6Al-4V as phase 2, the free surface was tracked after

each iteration using an UDF in FLUENT, before applying the heat energy for the next iteration. The volume of fluid equation used to track the free surface during melting and solidification is given in equation 2, where α represents the volume fraction of a fluid in a cell where 0< α <1. In each control volume, the volume fractions of all phases sum to unity.

$$\dot{\boldsymbol{Q}}_{(\boldsymbol{x},\boldsymbol{y},\boldsymbol{z})} = \boldsymbol{\eta} \times \frac{\boldsymbol{H_S} \times \boldsymbol{I_Z}}{\boldsymbol{S}} \tag{1}$$

$$\boldsymbol{I_z} = \frac{\mathbf{1}}{\mathbf{0.75}}\left(-\mathbf{2.25}\left(\frac{\boldsymbol{z}}{\boldsymbol{S}}\right)^{\mathbf{2}} + \mathbf{1.5}\left(\frac{\boldsymbol{z}}{\boldsymbol{S}}\right) + \mathbf{0.75}\right),$$

$$\boldsymbol{H_s} = \frac{\boldsymbol{2P}}{\boldsymbol{\pi d^2}}\,\mathbf{exp}\left\{-\frac{\mathbf{2}\left[(\boldsymbol{X}-\boldsymbol{X_s})^2+(\boldsymbol{Y}-\boldsymbol{Y_s})^2\right]}{\boldsymbol{d^2}}\right\}.$$

Where η is the absorption efficiency, P is the laser power, S is the penetration depth, d is the beam diameter, X_S, and Y_S define the position of the center for the heat source. Hs is the horizontal Gaussian distribution for the heat source and I_z describes the decay of the heat source magnitude in the vertical direction.

$$\frac{\boldsymbol{\partial \alpha}}{\boldsymbol{\partial t}} + \vec{\boldsymbol{v}}.\boldsymbol{\nabla \alpha} = \mathbf{0} \tag{2}$$

The boundary condition at the interface is given as

$$\frac{\boldsymbol{\partial(\rho H)}}{\boldsymbol{\partial t}} + \frac{\boldsymbol{\partial(\rho u_i H)}}{\boldsymbol{\partial x_i}} = \frac{\boldsymbol{\partial}}{\boldsymbol{\partial x_i}}\left(\boldsymbol{k}\frac{\boldsymbol{\partial T}}{\boldsymbol{\partial x_i}}\right) + \dot{\boldsymbol{Q}}(\boldsymbol{x},\boldsymbol{y},\boldsymbol{z}) - \boldsymbol{hA}(\boldsymbol{T}-\boldsymbol{T}_\infty) - \boldsymbol{\sigma A}\varepsilon(\boldsymbol{T^4}-\boldsymbol{T_\infty^4}) \tag{3}$$

where H is the enthalpy, k is thermal conductivity, $\dot{\boldsymbol{Q}}_{(\boldsymbol{x},\boldsymbol{y},\boldsymbol{z})\boldsymbol{int}}$ is the heat source applied at the interface, h is heat transfer coefficient, $\boldsymbol{\sigma}$ is the Stefan-Boltzmann constant and ε is the emissivity which is used to account for the radiation through the top surface and A is the free surface area of cell. Adiabatic boundary conditions are applied on all walls

of the domain. It follows the assumption that no heat transfer across the boundary in the simulated domain.

The density, specific heat, and thermal conductivity are functions of temperature. These temperature-dependent material properties for Ti-6Al-4V were included in the model using piecewise-linear functions [47]. For liquid metal, a constant viscosity value was used. Also, a variable surface tension was included using a UDF, given by equation 4.

$$\boldsymbol{\gamma = \gamma_m + \frac{d\gamma}{dT}\Delta T} \tag{4}$$

where γ is the surface tension at a given temperature past melting point temperature, $\boldsymbol{\gamma_m}$ is the surface tension at the melting point, $\boldsymbol{\frac{d\gamma}{dT}}$ is the surface tension gradient, and $\boldsymbol{\Delta T}$ is the temperature difference between the given temperature and the melting temperature. In this study, the default value of the surface tension and surface tension gradient for Ti6Al-4V resulted in strong depression of the melt pool, i.e., inadequate pull force. Therefore, both of these values were reduced by incorporating a factor into the UDF. The thermophysical properties of the material and the L-PBF processing parameters are presented in Figure 3.5 and Table 3.1. The default properties of argon gas pre-loaded in fluent were used for calculation of the model.

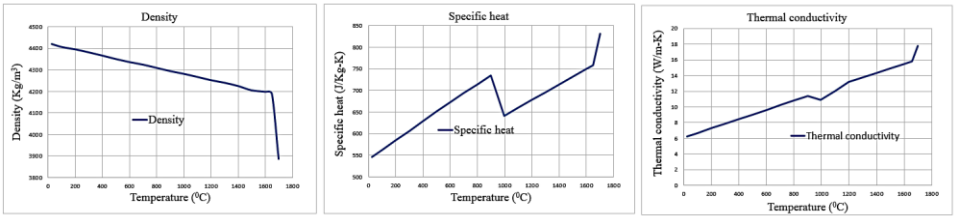

Figure 3.5 Temperature dependent material properties of Ti-6Al-4V [47, 48]

Table 3.1 Material properties of Ti-6Al-4V and processing parameters

Parameters	Values
Solidus temperature, T_S (°C)	1605
Liquidus temperature, T_L (°C)	1655
Latent heat of fusion, L_f (kJ/Kg)	440
Beam diameter, d (μm)	100
Power (W)	195
Scan speed (mm/s)	600
Viscosity(kg/m-s)	0.049
Ambient temperature (°C)	25
Emissivity, ε	0.5 [49]
Stefan-Boltzmann constant, σ (kg s^{-3} K^{-4})	5.67×10^{-8}

3.2.3 Thermo-fluid Modeling

The computational work was performed in a domain size of 1200 μm* 400 μm *250 μm. The powder particle coordinates along with their diameter data were imported from the result of DEM simulation. The imported layer of powder particles with layer thickness 60 μm lies on a 110 μm thick substrate. A constant mesh size of 5 μm was used to generate hexahedral mesh in the whole domain as shown in Figure 3.6 (a). The total number of elements in the domain was approximately 1 million.

a

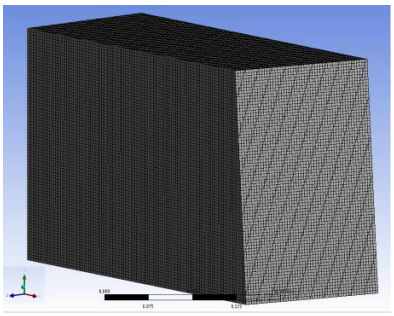

b

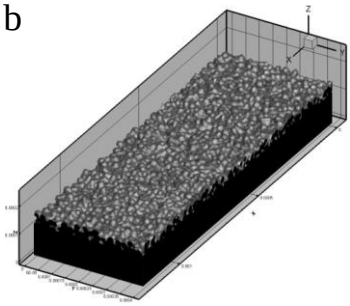

Figure 3.6 (a) Meshed domain cross-section; (b) Isometric view with cut section of model

Figure 3.6 (b) shows an isometric view of the model. Black color represents the thick substrate, while the grey color on the top represents the powder particles. The rest of the domain is filled with argon gas. In this study, argon gas is considered as phase 1 and Ti-6Al-4V as phase 2. The free surface lies between the substrate and the gas with volume fraction value ranging from 0 to 1.

3.3 Results and Discussion

3.3.1 Melt pool

The melt pool flow dynamics is described with the result for the case using powder particles with size range of 0-25 µm with scan speed of 600 mm/s, power of 195 W, and laser absorption coefficient of 0.38. The results for two other cases and their comparison is discussed later in the document. The application of heat source (laser power) increases the temperature of a certain volume of powder. The center portion from the incident laser beam will have the highest temperature with temperature gradient around it. Increase in the temperature melts the powder particle at the center which is then followed by the melting of surrounding powder particles as seen in Figure 3.7 (a). Smaller powder particles in the mixture melt before larger powder particles. The melted powder fills the voids

present between the powder particles due to the continuous flow of molten liquid, and the melt pool becomes dense. The melt pool then cools down and solidifies with the progress in time as the heat source moves from left to right. This process of melting and solidification continues, forming a single track. In case of high energy density, the temperature may exceed the boiling point of the material. This would result in evaporation and greater depression below the heat source. Such a scenario is not considered herein, and the effect of recoil pressure is also not included.

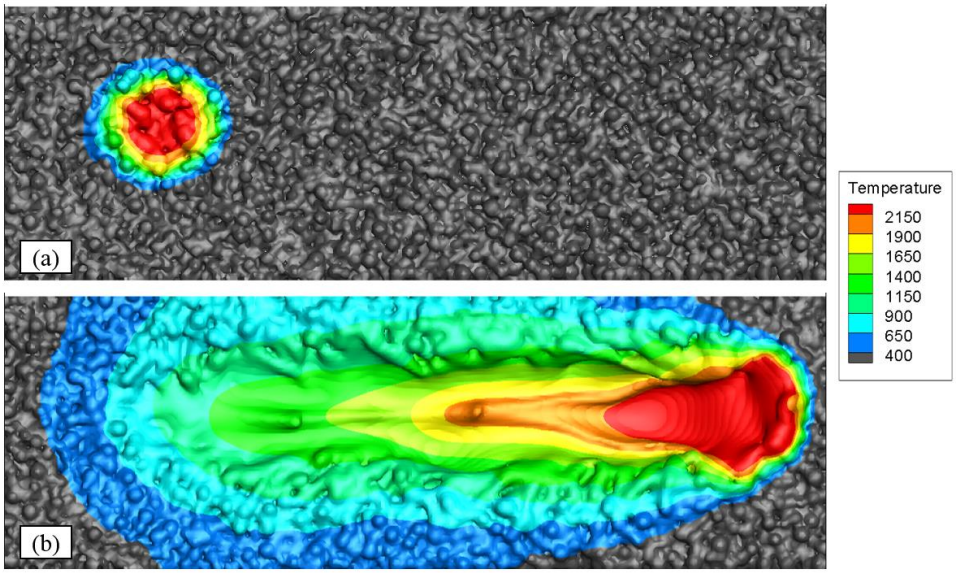

Figure 3.7 Top view of powder bed showing (a) the melt pool at t= 100 μs and (b) the solidified track and melt pool at t= 1500 μs along with the temperature (^{0}C) distribution.

In the melting process, the flow of liquid metal is outwards, i.e., from higher to lower temperature, due to the surface tension gradient. As the heat source moves from left to right, the rear portion starts to cool due to thermal diffusion. During solidification, the melt flow changes direction from outer to inner, which contributes to the formation of a

bead. This continuous process of melting and solidification leads to a continuous single track.

Figure 3.8 illustrates the transient behavior of the melt flow during single track formation, showing the volume fraction of fluid in a slice from a transverse cross-sectional view. The laser beam is the energy source and heats the powder at the center of the powder bed. The spherical powder slowly starts to change its shape at t= 300s µs. The melt pool depth keeps increasing up to t= 600 µs. During solidification, the melt flow is pulled in the upward direction to form a track, as seen in t = 900 µs. The melt pool increases in depth during the heating period and then the flow reverses under the effect of increasing surface tension to form a solid track.

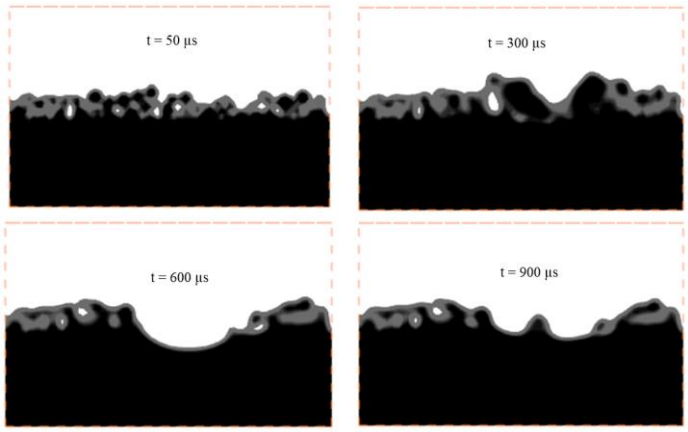

Figure 3.8 Melt pool flow with time progression.

A single track experiment was carried out in an EOS M270 machine with Ti-Al6-V4 powder of size distribution 15-40 µm to quantitatively study the effect of scan speeds on the track width. Then surface of the formed track was analyzed using white light interferometer to obtain the melt pool width. Detail of that study were presented in another publication [50]. The track width value obtained from the experiment followed the trend

and was in good agreement with the computational result. At 600 mm/s, the width value from the experiment is 202.36 μm versus the simulation result of 200±10 μm.

3.3.2 Comparison of the result of the different range of powder distribution

The powder with size distribution in the range of 0-25 μm showed comparatively less void space. The particles with smaller diameter filled the void space, whereas in other two cases, there was more space between particles. Another factor affecting the void space is the lower and upper value of the particle diameter, as is evident by the powder distribution result presented in Figure 3.9. The size range of the powder simulated in this study shows that lower value of particle diameter and lower size range of powder resulted in a more consistent and continuous melt pool flow, as shown in Figure 3.9. For the same power, particles with larger diameter take more time to melt completely in comparison with those of smaller diameter. Thus, there is incompletely melted powder in the melt pool. The edges of the melt pool boundary also contain incompletely melted powder, giving rise to a coarser surface finish in the final part. Also, in the case of powder particles with larger diameter, the melt pool depth increases temporarily in the region where there are more large particles.

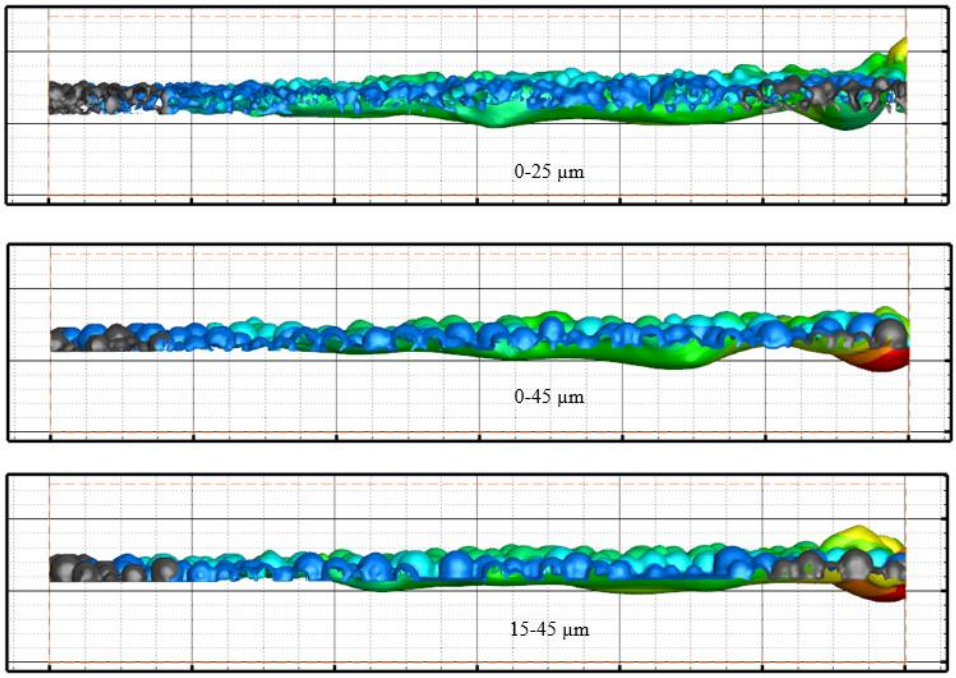

Figure 3.9 Snapshot of temperature contour along with the solidified track at t = 2000 µs for three size ranges of powder distribution.

3.4 Conclusion

A DEM method was used to simulate powder particles of different size ranges and their distribution on a build plate. A 3D thermo-fluid model was developed and completed with the powder particle distribution and user-defined functions to model the heat source as well as to input other necessary parameters. The model was meshed at 5 µm to capture the melt pool flow dynamics at mesoscale level. Metallic powder with three size ranges was simulated under an identical condition to observe the effect of the powder distribution on the melt pool flow dynamics. The computational results lead to the following conclusions:

- The powder particle size and particle size distribution play an important role in the final part manufactured using the L-PBF process.

- Presence of particles of smaller diameter in the powder mix supports a consistent and continuous melt pool flow, while any kind of void enhances fluid convection in the downward direction, causing a temporal increase in melt pool depth.

- This model can be applied to predict the effect of key process parameters including the scan speed, power, and laser absorptivity on the melt pool dimensions.

  This study was carried out for power of 195 W and scan speed of 600 mm/s. Simulation results for powder distributions with different size ranges and different power intensities could also be analyzed for broader understanding.

One limitation of this model is that it assumes that all the powder particles are perfectly spherical, which is not the case for metal powders. Though no experimental work has been done during this study to validate the effect of the different ranges of powder particles, the model was successfully applied for quantitative analysis of the track width for various scan speed at a constant power.

CHAPTER 4

POROSITY ANALYSIS AND PORE TRACKING OF METAL AM TENSILE SPECIMEN BY MICRO-CT

4.1 Introduction

Material porosity is inherent in the parts manufactured by the L-PBF process. It is desirable for some biomedical implants but undesirable for aerospace and automotive components as porosity can lead to unexpected failure [51]. It is necessary to understand the effect of process parameters on the pores, which in turn will allow the user to control the porosity to some extent in the built parts. Multiple techniques have been used by researchers to evaluate the porosity. The most common approach, which is destructive to the specimen, is to cut the specimens and observe the polished cross-sections [52]. A non-destructive technique to characterize the porosity is by using computed tomography [53].

X-ray computed tomography (XCT) can be utilized to obtain a complete three-dimensional structure of a sample with the help of high-resolution scanned images. Though primarily used in the field of life sciences and art conservation, its use in the field of engineering and material science has increased in recent years [54]. Improvement in the pixel size resolution and quicker reconstruction time has led to an increase in the availability as well as the use of XCT [55].

Thompson et al. [56] trace back the use of XCT in additive manufacturing (AM) to 1990 and categorizes the subsequent years in four different timelines. Their review states that from 2010 onwards the use of XCT as an inspection and dimensional measurement tool has increased significantly in the field of AM. Recently, it has also been used by several researchers to detect any internal defects, visualize pore distribution in the samples as well as to analyze the morphometry of pores. However, the accuracy of the results from XCT is highly dependent on the pixel resolution of the scan. Leuders et al [57] used HIP processing to reduce the pore size of Ti64 samples and showed a relative density of 100% for a scan of 22 μm resolution. Spierings et al [58] compared different density measurement techniques for metallic AM parts and found the result from the XCT method as satisfactory. Wits et al [59] concluded in their study that the CT predicts systematically higher relative density due to several reasons, but the CT results are comparable with results from the Archimedes method along with the added capability of investigating pore morphology. Siddique et al [60] showed that there was no significant difference in the result for critical pores obtained from metallographic study and CT scan of voxel resolution of 4.8 μm for AlSi12 samples. Maskery et al [61] concluded that the statistical quality obtained by the data from CT would not be achievable by conventional cross-sectioning and microscopy due to the requirement of a large number of micrographs for their study of 5 mm cube AlSi10Mg samples. Duplesis et al. [62] emphasized the use of CT for quality control in AM in a series of papers describing a standard method for porosity analysis.

Porosity is one of the common defects in the L-PBF produced parts. It leads to poor density and has an impact on the mechanical properties of the built part [63]. The porosity in the built parts is due to the lack of fusion, keyholing or trapped gas [64]. This study is

focused on the analysis of keyhole pores from as-built tensile samples and after the tensile testing. Keyhole pores are formed when excess energy is imparted to the melt pool by the laser source. Although keyhole pores are stochastic in nature, there is a higher possibility of their formation at the end of a scan line. Shrestha et al [65] studied the keyhole porosity for different linear energy density values analyzing data from micro-CT analysis of single tracks. Martin et al [66] presented a mitigation strategy to prevent the formation of keyhole pores at the laser turn points. Results from the CT scan are analyzed to examine the effect of porosity on the tensile strength of the samples. The pore morphology is also studied before and after the tensile test.

4.2 Methodology

The tensile test specimen design is based on standard test methods for tension testing of metallic materials ASTM E8 [67]. The original dimension has been scaled by approximately 50% to reduce the build time. The sample is designed to have a gripping width of 10 mm and is 3 mm thick. Eighteen unique samples were built at different locations and in different orientations with a change in energy density. The scan speed is kept constant at 600 mm/s, and the laser power is varied at 85 W, 100W, and 150 W. The combination of the scan speed and three power values is labeled as low, medium, and high respectively for this study. The samples were built with Ti64 powder supplied by LPW technology in an EOSINT M 270 system. Layer thickness and hatch spacing were fixed to 30 µm and 100 µm, respectively. The parameters are presented in Table 4.1. Additionally, the specimens were built at three different locations; location A- closer to the chamber window, location B- on the opposite end of the chamber window and location C- at a height

of 35 mm from the build plate on the opposite end of the chamber window. The samples were built in an orientation of 45° (slant-build) and 90° (vertical-build). Three replicates were built for each sample in the same build. Although tensile testing was done for all three sets of replicates, CT scan was done on only one replicate set i.e., replicate set 3. Further details and diagrams of this experiment are presented in a study by Zhang et al. [68].

Table 4.3 Experimental parameters for tensile samples

Parameters	Levels	Values
Location	3	A, B, C
Power (Watt)	3	85(L), 100 (M), 150 (H)
Scan speed		600 mm/s
Orientation	2	Slant (S), Vertical (V)
Unique	18	

Computed tomography involves taking x-ray projection images of a sample from many angles around the sample. The projection images are taken over a rotation of either 180 or 360 degrees around the sample with small angular increments. These projection images are then mathematically converted into a stack of cross sectional images. The combination of those cross sectional images will generate a three-dimensional volumetric image of the sample.

The CT scanner used in this study is a Bruker micro-CT SkyScan 1173 scanner. The scanner and the zoomed view of the sample with the sample holder inside the scanner are shown in Figure 4.1. The scanner is equipped with a 130KV Hamamatsu X-ray source and a 5 MP flat panel sensor camera detector. The x-ray generated from the X-ray source passes through a 0.25 mm thick brass filter, which absorbs the radiation below a certain

energy level. An appropriate amount of x-ray transmission is required to obtain a better dynamic image contrast in the scanned images. The low transmission will increase the noise level while the higher transmission will reduce the contrast between different densities in the images. The required transmission for high density metallic samples is in the range of 20% to 40%. In the study, the transmission varied around 30% to 35%.

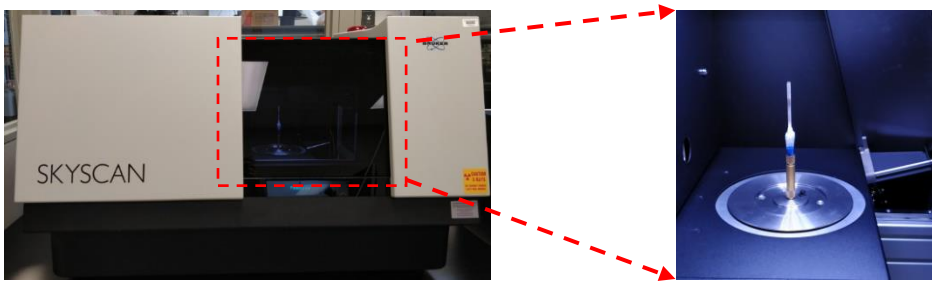

Figure 4.1 Image of the CT scanner system used in the study along with the zoomed view showing the sample holder and the sample on the stage

The sample was put in a sample holder and wrapped around with paraffin tape to restrict any movements of the sample during the scanning process. During the scan, the sample is rotated with an angular increment of 0.2 degrees from 0 to 360 degrees. One TIF image is generated for each rotation degree totaling to 1800 images from a complete scan. Only the gage portion of the samples was selected for the scan process at a voxel resolution of 6.1 μm. All the scans in this study were completed at 130 KV, 60 μA and exposure time up to 1020 ms.

The projection scan images are converted into 2D cross-sectional grayscale images using reconstruction software called NRecon. Reconstructed images are saved as 8-bit bitmap image files. During the reconstruction process, the user aims to reduce the artifacts

that are inherent to the CT scan process including beam hardening, ring artifact, and misalignment. This process usually requires user experience to produce the best reconstructed images. Furthermore, pores present in the sample were visualized and the pore morphology was studied using Bruker's analysis software package.

4.3 Results and Discussion

4.3.1 As-built samples scan result

All eighteen samples were scanned at 6.1 μm voxel resolution in as-built condition before the tensile test. It is the highest resolution possible from the Skyscan 1173 micro-CT scanner. At this resolution, approximately 13.5 mm of the gage length is scanned. Figure 4.2 (a) shows a typical sample, (b) shows the preview of the sample in the CT system and (c) gage length scanned at 6.1 μm voxel resolution.

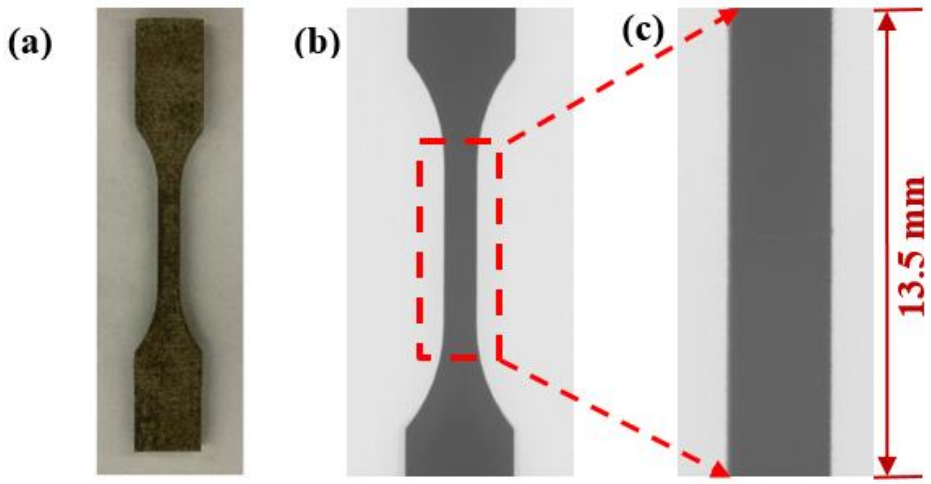

Figure 4.2 (a) As-built sample built from the L-PBF process; (b) Preview of the sample in the CT system; (c) Scanned gage region.

The scanned perpendicular projection image set was reconstructed using the system's software package to produce cross-sectional images of the eighteen unique samples. Visualization of the cross-sectional images show that there is a relatively large number of pores in the high energy samples and almost no pores in the medium and low energy samples. The pores in the high energy samples are stochastic in nature. In the Figure 4.3, the dark black dots represent lower density (pore), and the brighter grey color represents the area with a higher density (solid).

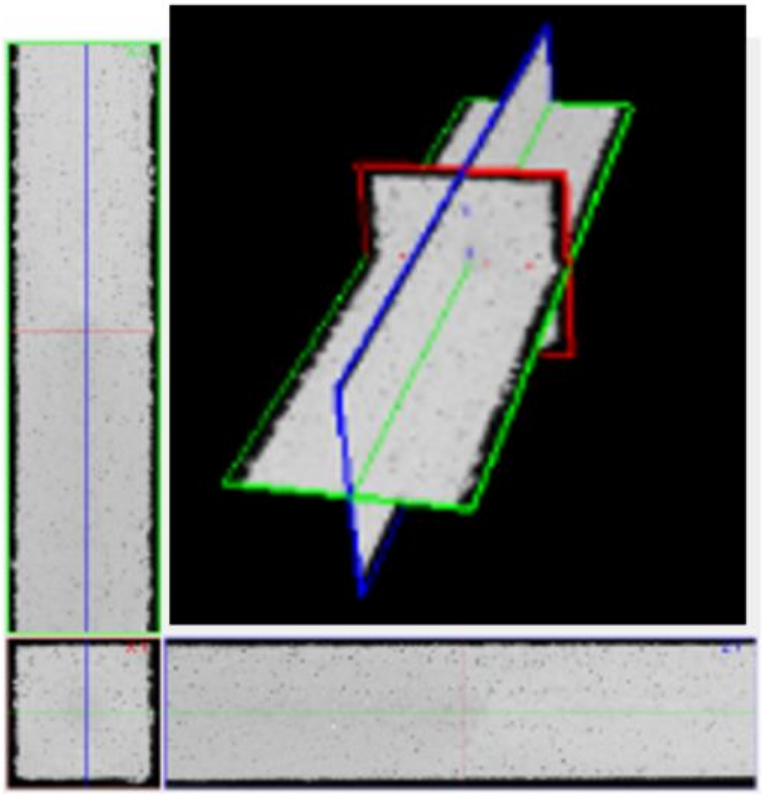

Figure 4.3 Three cross-sectional views of the middle of the gage region for a typical high energy case

Transverse and Coronal views of the as-built sample cases are presented in Figure 4.4, Figure 4.5and Figure 4.6 below. The samples are identified using alphabet codes to represent the energy density, location, and build orientation, respectively. Three replicates were built for each process condition in the powder bed experiment, but only one of the replicates was scanned using the CT system. The number after the three alphabets represents the replicate that was scanned. For example, HAV3 is the code for a high energy sample built at location A and in vertical orientation. The number 3 represents the third set of replicates which was used for the CT scan. The alphabet codes are also mentioned in Table 1. Among the high energy cases, it is apparent from a visual comparison that the specimen at location B has comparatively fewer pores.

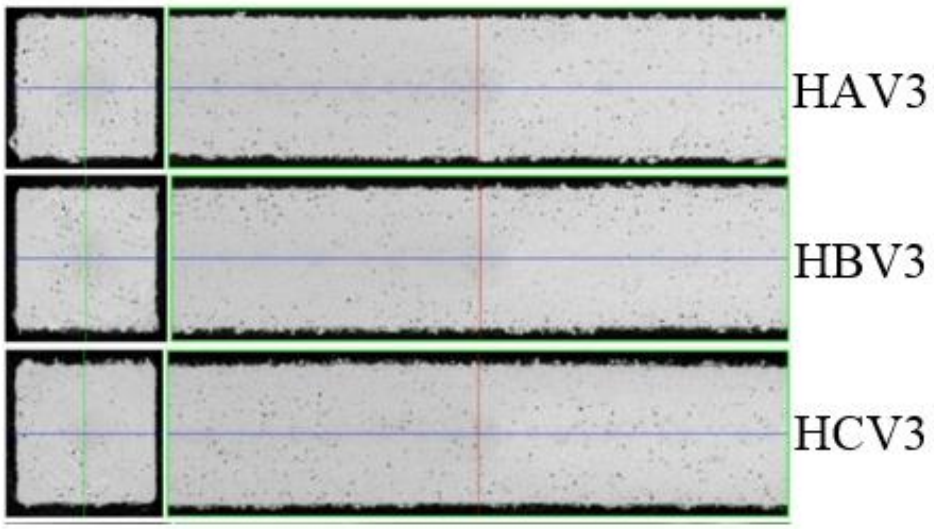

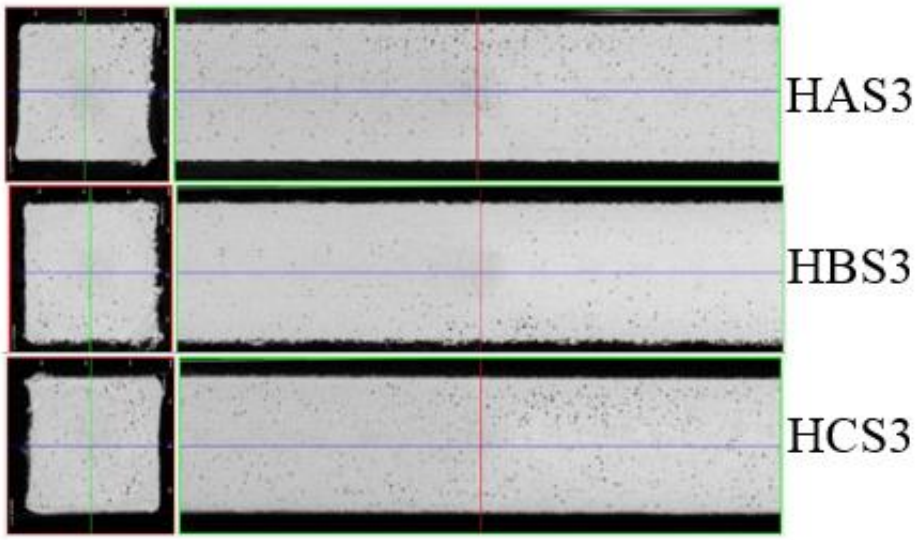

Figure 4.4 Transverse and Coronal views of high-level energy density vertical-build specimens (top) and slant-build specimens (bottom) at different build locations

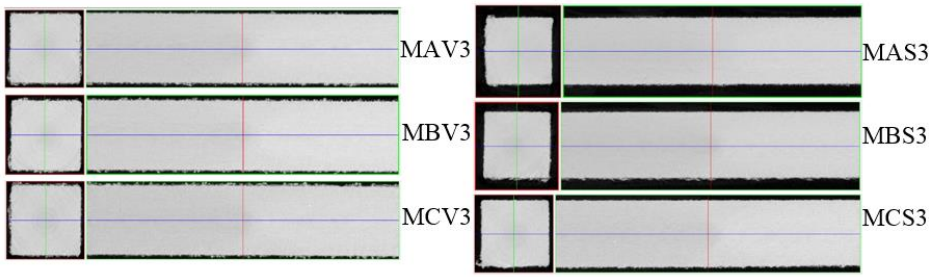

Figure 4.5 Transverse and Coronal views of medium-level energy density vertical-build specimens (left) and slant-build specimens (right) at different build locations

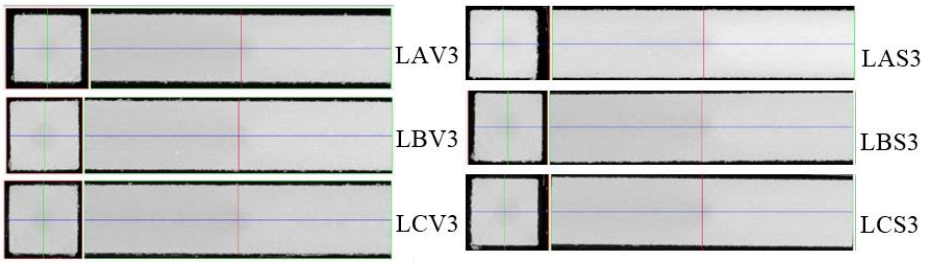

Figure 4.6 Transverse and Coronal views of low-level energy density vertical-build specimens (left) and slant-build specimens (right) at different build locations

4.3.2 Comparison based on energy level, location, and build orientation

Porosity is analyzed from the reconstructed images for all as-built unique samples. There are approximately 2230 reconstructed cross-sectional image slices in the scanned result of each case. A region of interest is defined, and the image set is converted into binary for the quantification of the porosity. An example of an image slice and its corresponding binary image is shown in Figure 4.7. An average grayscale threshold is also applied to all the image slices in the next step.

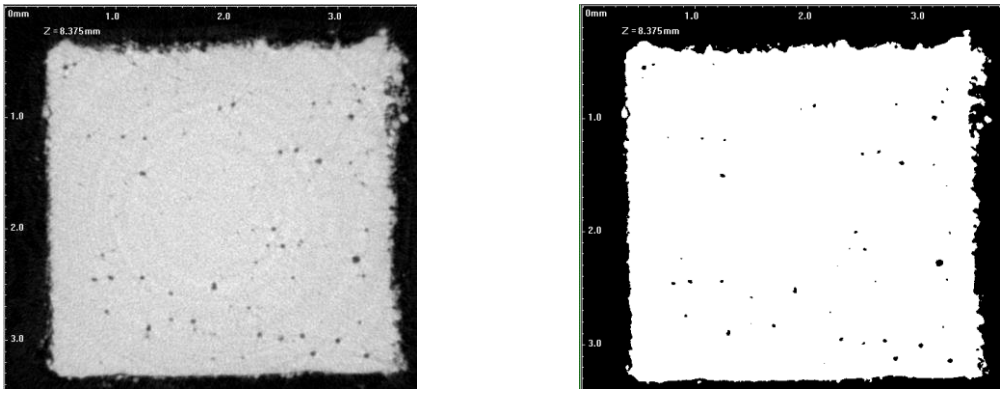

Figure 4.7 Example of one image slice and its corresponding binary image

Figure 4.8 shows the raw image of one slice and binary images for the same slice for a representative high, medium, and low energy case, respectively. Only closed pores are considered for porosity analysis. For this analysis, a closed pore in 3D is a connected assemblage of space (black) voxels that is fully surrounded in 3D by solid (white) voxels. Despeckling of 7 voxels is done in the 3D space to reduce noise before performing porosity analysis.

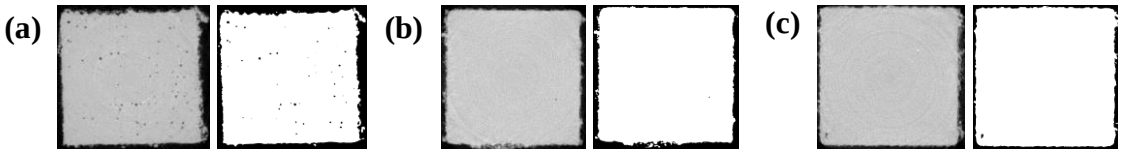

Figure 4.8 Example of one image slice and its corresponding binary image for (a) high (b) medium and (c) low energy cases

The result of the 3D pore analysis is tabulated below in Table 4.4. All the results presented in the Table 4.4 (a) are obtained without any despeckling while the results in Table 4.4 (b) are obtained after using the despeckling function. Despeckling function results in the reduction of the number of pores but no significant reduction in the pore percentage. The use of the despeckling function is recommended to remove the small volumes which generally arise due to the image defects in the reconstruction and binarization process rather than the fabrication process itself. So, further analysis and comparison are completed from the analysis result obtained after the use of the despeckling function. In this study, a despeckling of 7 voxels was performed in the entire set of images before porosity analysis. Overall, vertically built samples have a higher number of pores compared to slant-build samples for their corresponding energy level and build location

with an exception for high energy sample at Location C. This sample also has the highest pore volume and closed porosity percentage. Pore volume is the total volume of all closed pores and percentage closed porosity is the volume of closed pores as a percentage of the total of solid plus closed pore volume in the defined location of interest. The slant sample at location B has the least amount of porosity and pore volume in high-level energy density cases. For medium and low energy density samples, the porosity percentage is less than 2.5×10^{-4}%. And the highest pore volume for medium energy is in the vertically built sample at Location A (7.54×10^{5} μm^3) while for low energy it is in the vertically built sample at Location C ($2.72\times10^{5}\mu m^3$).

Table 4.4 Number of pores and porosity percentage (%) in all tensile specimens (a) without despeckling and (b) despeckling of 7 Voxels in 3D

(a) Without despeckling

Orientation	Energy density level	Number of pores in			Porosity in location		
		A	B	C	A	B	C
Vertical build	High	35846	2881	29006	0.5254	0.3939	0.4592
	Medium	863	806	872	6.7×10^{-4}	3.3×10^{-4}	8.7×10^{-5}
	Low	485	301	528	1×10^{-4}	4.5×10^{-5}	2.6×10^{-4}
Slant build	High	31792	1757	36827	0.4675	0.1917	0.5586
	Medium	680	1156	518	8.7×10^{-5}	3.5×10^{-4}	1.8×10^{-4}
	Low	18	225	596	1.6×10^{-4}	5.4×10^{-4}	1.2×10^{-3}

(b) Despeckling of 7 Voxels

Orientation	Energy density level	Number of pores in			Porosity in location		
		A	B	C	A	B	C
Vertical build	High	28225	2194	22540	0.5234	0.3922	0.4576
	Medium	58	72	32	5.9×10^{-4}	2.5×10^{-4}	8.8×10^{-5}
	Low	14	14	20	7.2×10^{-5}	2.3×10^{-5}	2.2×10^{-4}
Slant build	High	24312	1320	24355	0.4656	0.1905	0.5563
	Medium	12	57	30	3.5×10^{-5}	2.6×10^{-4}	1.3×10^{-4}
	Low	12	10	20	1.6×10^{-4}	3.5×10^{-5}	7.4×10^{-5}

4.3.3 Relation between tensile properties and the porosity of the samples

A graphical comparison between porosity percentage and ultimate tensile strength (S_{ut}) values of replicates number 3 is presented in Figure 4.9. There is no clear trend for tensile S_{ut} based on the porosity. However, one conclusion that can be drawn is that the high-energy samples built at an angle exhibit the lowest tensile strength value among all the tested samples. Focusing on the porosity of high energy samples, sample built at a slant at the location B has the least porosity percentage as presented in Table 4.5 and plotted in Figure 4.10. The variation in the tensile strength of all the replicates as well the coupled effect of the different process parameters on the mechanical properties are presented in detail in a paper by Zhang et al. [68].

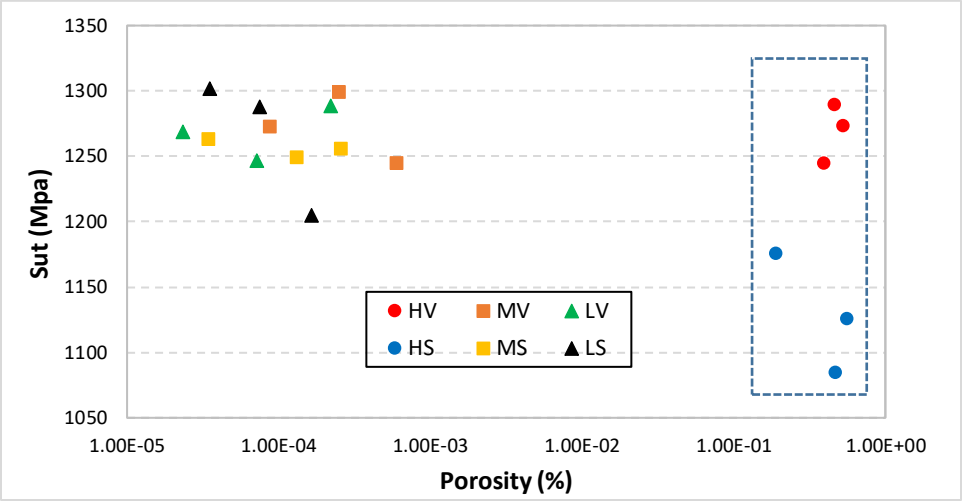

Figure 4.9 Graphical representation of S_{ut} of replicates number 3 of all sample cases vs. porosity.

Table 4.5 Data for porosity and tensile strength from replicates number 3 of high energy samples

Sample	Porosity (%)	S_{ut} (MPa)	Sample	Porosity (%)	S_{ut} (MPa)
HAV3	0.5234	1274	HAS3	0.4656	1085
HBV3	0.3922	1245	HBS3	0.1905	1176
HCV3	0.4576	1290	HCS3	0.5563	1126

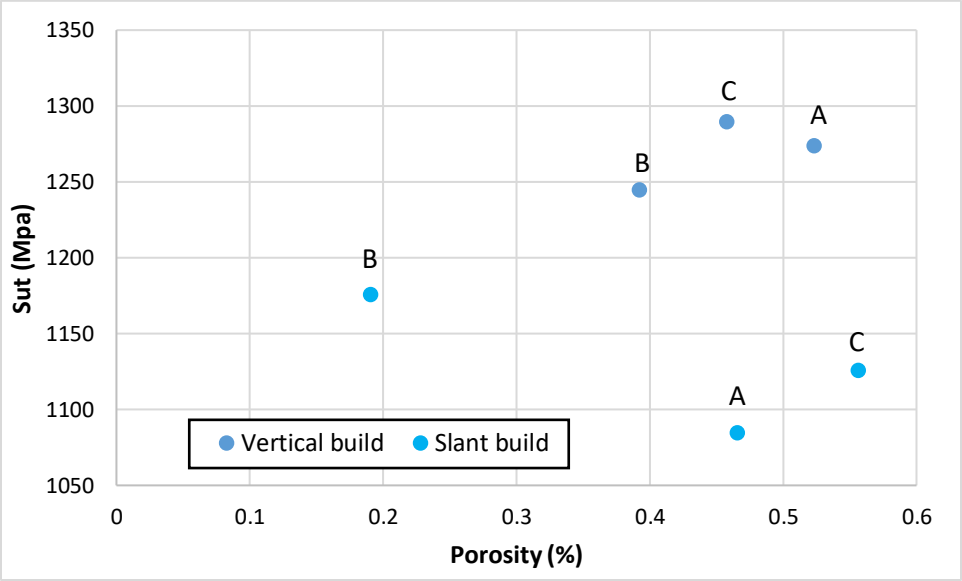

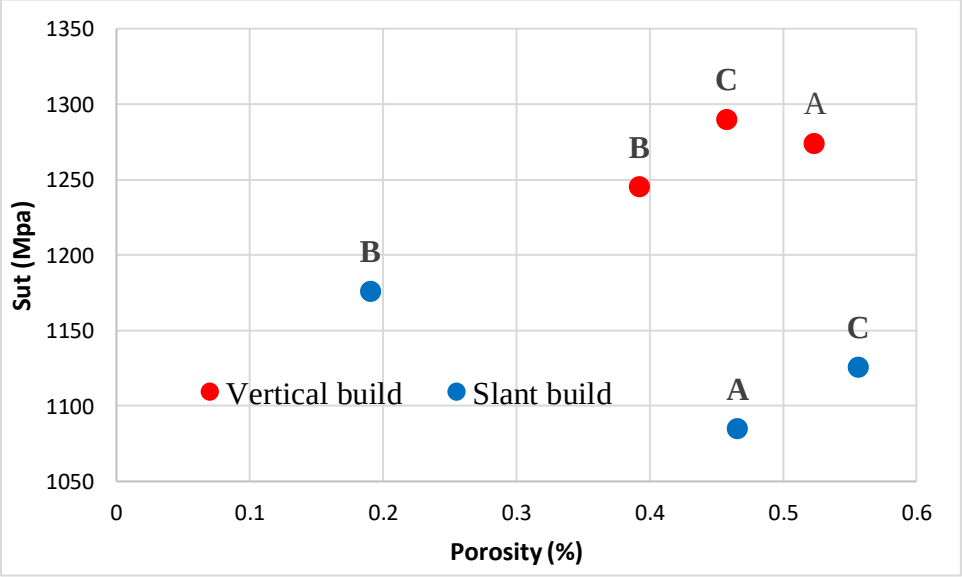

Figure 4.10 Graphical representation of S_{ut} of high energy cases of replicates number 3 vs. porosity percentage.

4.3.4 Fractured samples scan result

After the tensile testing of the samples, the fractured samples were scanned using the CT system. The scan was completed following the same process and similar scan settings as that for the as-built samples which is mentioned in the methodology section. However, the volume of the sample scanned for as-built sample and the fractured sample is different. The two parts of the fractured sample were held together with paraffin tape without the application of any external force. Some gap (appx 0.5-1.5mm) is present between those two pieces which can be clearly seen in Figure 4.11 (c). This results in a lower scan volume for the fractured samples in comparison with their corresponding as-built counterparts. Table 4.6 presents the number of pores and the porosity percentage for fractured samples. The results show both of those values have increased compared to their as-built counterparts. A detailed comparison is presented in the next section.

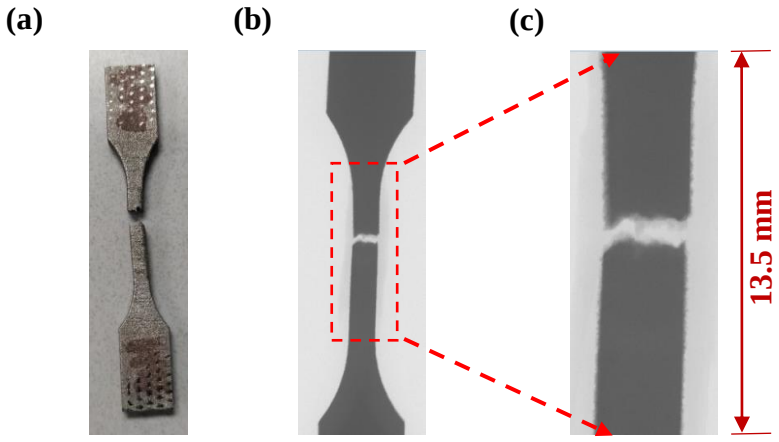

Figure 4.11 (a) Fractured sample after tensile testing; (b) Preview of the sample during the scan process and dashed region selected to scan; (c) Scanned region.

Table 4.6 Number of pores and porosity percentage (%) in nine fractured tensile specimens. (Despeckling of 7 Voxels in 3D)

Orientation	Energy density level	Number of pores in			Porosity in location		
		A	B	C	A	B	C
Vertical build	High	30687	2390	24522	0.752	0.535	0.536
	Medium	77	230	28	8.3×1	1.3×1	1.1×1
	Low	230	232	170	1.3×1	8.1×1	4.4×1

4.3.5 Porosity comparison between as-built samples and fractured samples

In the next step, the porosity percentage of the as-built sample is compared with the fractured sample. The contrast with this comparison is that the scanned region for the as-built and the fractured samples is not exactly the same. However, the comparison does give a general idea of the change in porosity in the fractured samples. The fractured counterparts of the nine samples that were built in vertical orientation were scanned and compared with the porosity result of their corresponding as-built samples. The details of the porosity comparison for the nine as-built samples and their nine fractured counterparts are presented in Table 4.7. The volume of the scan region (Volume of interest - VOI) is less for fractured samples because of the gap shown in Figure 4.11. Although the VOI has decreased for the fractured samples, the porosity percentage has increased significantly as shown in Figure 4.12. Overall, the least increase in the pore volume is 9.5 % and the porosity percentage is 17.2 % for the sample FHCV3. FHCV3 represents the fractured sample built with a high energy parameter at location C in a vertical orientation and the number 3 denotes the third

replicate. The letter F in the FHCV3 is used to indicate the fractured sample of the as-built counterpart of HCV3. The increase in the pore volume is proportional to the increase in the porosity percentage. Pore tracking shows that there is an increase in the volume of each pore. The approach for the pore tracking and the results obtained is presented in the next section. The medium and low energy samples show a significant percentage increase in their pore volume and there is an overall increase in the number of pores in the fractured samples. It could be the result of the increase in the volume of pores that were earlier not detected by the 6.1 μm resolution of the CT scan in the as-built sample.

Table 4.7 Porosity comparison (Despeckling at 7 voxels) of vertically built as-built samples and their fractured counterpart

Samples	Object volume	No. of pores	Pore volume	Porosity
AHV3	126.6	28225	0.67	0.52
FAHV3	114.1	30687	0.87	0.75
	-12.5	2462	29.8%	43.8%
BHV3	127.6	21946	0.50	0.39
FBHV3	113.0	23907	0.61	0.54
	-14.6	1961	21.1%	36.5%
CHV3	125.2	22540	0.58	0.46
FCHV3	116.8	24522	0.63	0.54
	-8.4	1982	9.5%	17.2%
MAV3	126.05	58	7.54E-04	5.98E-04
FMAV3	109.65	77	9.08E-04	8.28E-04
	-16.4	19	20.4%	38.4%
MBV3	126.12	72	3.19E-04	2.53E-04
FMBV3	111.97	230	1.44E-03	1.29E-03
	-14.2	158	352.4%	409.5%
MCV3	126.04	32	1.11E-04	8.77E-05
FMCV3	116.23	28	1.31E-04	1.13E-04
	-9.8	-4	18.5%	28.5%
LAV3	123.67	14	8.88E-05	7.18E-05
FLAV3	107.64	230	1.44E-03	1.29E-03
	-16.0	216	1524.7%	1694.4%

LBV3	123.32	14	2.88E-05	2.33E-05
FLBV3	109.19	232	8.85E-03	8.10E-03
	-14.1	218	30654.4%	34633.5%
LCV3	123.54	20	2.72E-04	2.20E-04
FLCV3	106.58	170	4.66E-03	4.37E-03
	-17.0	150	1612.2%	1884.5%

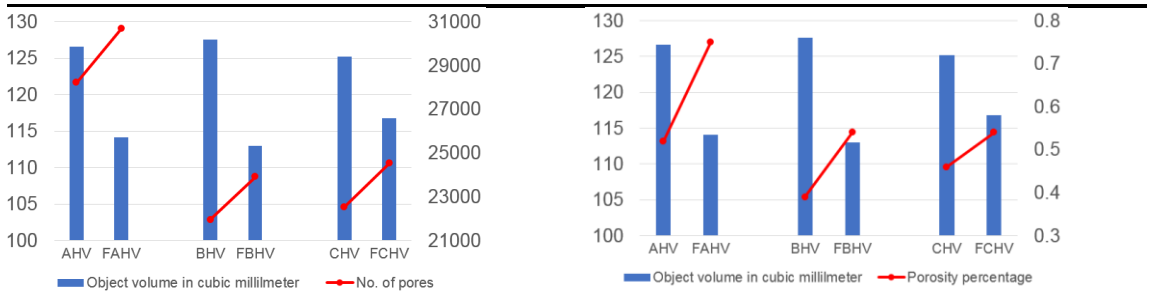

Figure 4.12 Graphical comparison of object volume with number of pores (left) and porosity percentage (right) for high energy samples and their fractured counterparts.

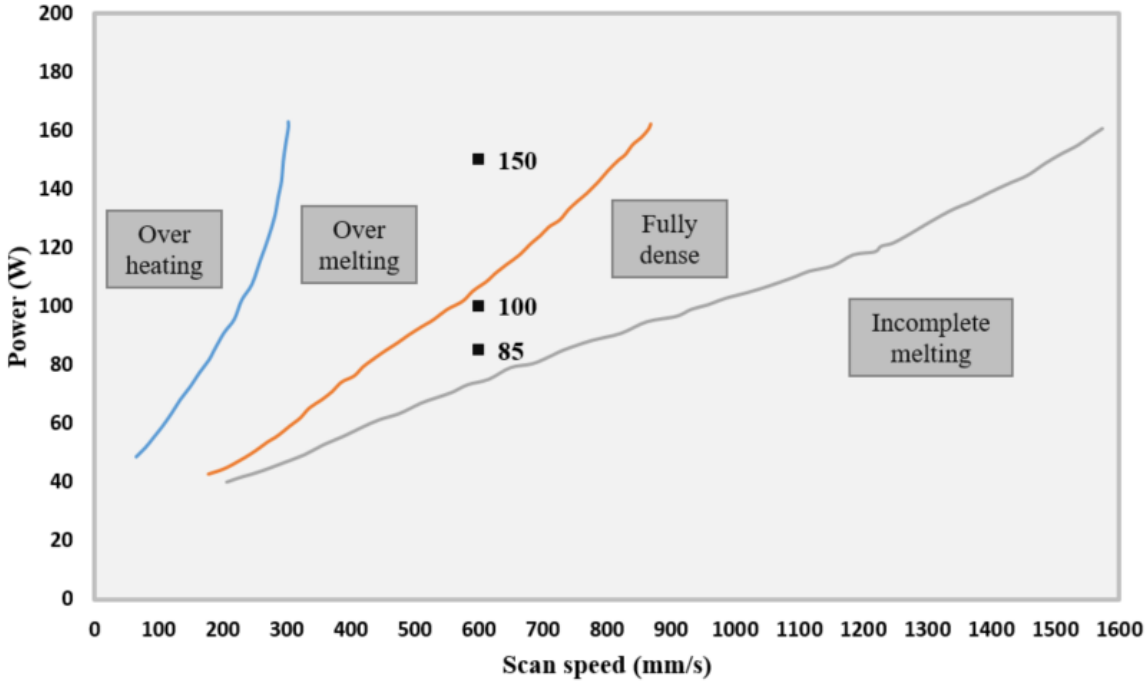

Figure 4.13 Scan parameters used in the study overlaid on the process window of the LPBF process from the reference [69].

The low and medium power values fall in the fully dense zone while the high-power value falls in the over melting zone for a constant scan speed of 600 mm/s as shown in Figure 4.13. The pore count and pore volume for the low and medium energy level before the fracture is less than 100 while that for high energy value is in thousands. However, the pore volume increase in the fractured samples for low energy case is significantly higher compared to the medium energy level. This could be again attributed to the resolution limit of the CT system. The assumption is that the pores present in the low and the medium energy as-built samples are not detected by the 6.1 μm resolution.

4.3.6 Pore tracking of the as-built and fractured samples

The change in the pore volume between the as-built and fractured samples are presented in Table 4.8. One voxel represents a volume of a cube of 6.1 microns. So, one voxel is approximately equal to 227 cubic microns. Pores volume has increased in the fractured sample but the pores with the highest diameter are not present in the fractured sample. This is because those pores in the HAV sample was opened during the tensile testing. More than eighty percent of the pore has 0.8-1 sphericity. This means the majority of the pores are Keyhole pores. Corresponding as-built sample and the fractured sample image sets were loaded simultaneously in the analysis software and compared side by side based on decreasing order of pore volume. The software generates a list of the pores including the information about pore volume, surface, sphericity, and others. Few pores were tracked for each fractured samples of high energy cases for comparison with their as-built counterparts are presented in Table 4.9.

Table 4.8 Comparison of pore volume between as-built and fractured samples.

	Number of pores					
Voxel size (cubic	HAV	FHAV	HBV	FHBV	HCV	FHCV
0-500	27572	29588	21524	23274	21901	23876
500-1000	578	960	396	590	525	585
1000-1500	64	110	25	39	46	49
1500-2000	10	19	1	4	6	10
2000-2500	1	9	-		4	2
2500-3000	-	1	-	-	-	-
Total	28225	30687	21946	23907	22540	24522

Table 4.9 Comparison of a pore present in as-built and fractured case at three different location.

Change in Pore Volume (Voxels) of the tracked pores	
HAV	**FHAV**
2018	2253
1795	2113
1756	2114
1712	1877
HBV	**FHBV**
1611	1670
1377	1640
1251	1899
HCV	**FHCV**
2204	2123
1941	1982
1835	2459

4.4 Conclusion

Eighteen tensile samples were scanned using a CT scan system. Reconstruction software was used to generate the cross-sectional images from the scanned projection images. Porosity analysis was done on the entire image set of as-built samples. After the scanning process, the tensile testing of the samples was performed. Scanning, reconstruction, and porosity analysis were carried out for fractured samples that were built vertically. Some of the large pores are tracked in the as-built and the fractured samples to compare the change in the pore morphology.

- The medium (100 W) and the low energy parameters (85 W) falls in the fully dense region of the process window. In the as-built medium and low energy samples, there are fewer number of pores which are comparatively smaller in volume. The low porosity percentage in the range of 10^{-4} is indicative of the high density.

- Although high energy (150 W) slant-built samples at locations A and C have comparatively similar porosity percentages to the vertically built samples, the tensile strength is lower. The build orientation has a significant effect on the tensile strength. However, there is no clear trend in the tensile strength values based on the variation in location.

- CT scan of the samples after tensile testing shows higher pore volume even though the scanned volume has decreased. There is a significant increase in the pore volume and porosity percentage in the fractured samples. The stress applied during the testing process causes pre-existing pores to propagate, resulting in larger pores, and increased

porosity. The resolution of the CT scan used in the study is limited to 6.1 microns. Therefore, the CT scan for the fractured samples might have detected the expanded pores that were already present in the as-built samples but not previously capture by the scan. Pore tracking of individual pores confirms the increase in the volume of the pores in the fractured samples.

CHAPTER 5

TRANSIENT MELT POOL FORMATION IN LASER-POWDER BED FUSION PROCESS

5.1 Introduction

Laser-powder bed fusion (LPBF) process can produce highly dense metals parts with complex geometrical features [70]. The advancement in this technology has enabled the user to create lightweight high-strength [71] and bio-inspired design structures [72], thin walls [73], and heat exchangers with internal features [74] that cannot be fabricated by conventional manufacturing methods. Many of these designs have small features, which have dimensions in the range of 1-2 mm or less. The characteristics of these features are not like the bulk components [75].

Three-dimensional parts are produced using the LBPF process in a layer-by-layer fashion. The laser heat source is used to selectively melt the fine metallic powders in the order of microns that are spread over a substrate. It involves rapid melting and solidification during the process. There is a complex interaction between the laser and the metallic powder, which is highly affected by the change in process parameters [76, 77]. This interaction in each layer is governed by a scanning strategy [78]. The scan strategy typically consists of many short segments instead of long passes to avoid residual thermal stress. The melt pool during the short segment scans shows variations along the scan length.

The melt pool for long passes will reach a quasi-steady state after the laser beam travels a certain distance given that the scanning direction is unchanged [79]. The melt pool geometry before the quasi-steady state i.e., the transient state is quite different. Furthermore, the laser beam goes through a phase of acceleration or deceleration at turn points at which the melt pool exhibits different properties [80].

Previous studies in the LENS and EBAM process have analyzed the melt pool geometry for different process parameters to control the melt pool size. Birnbaum et al [81] were able to achieve a desired melt pool size in the LENS^{TM} process using a process map approach. They successfully created a model to change the power or the velocity establishing a dynamic feedback control of the melt pool. Aggarangsi et al [82] further expand the process map approach to study the response of melt pool size to step change in power and velocity. Soylemez et al [83] presented a map of curves of constant melt pool cross-sectional area and length to depth ratio for electron beam additive manufacturing (EBAM) established by analytical and numerical method. Fox et al [84] studied the melt pool depth of Ti-6Al-4V single tracks for a wide range of power (1-5kW) and velocities (1-100 in /min) for the EBAM process. The power and velocities used in this study is high compared to the parameters generally used in the LBPF process.

Cheng and Chou [85] developed a thermal model to study the melt pool in Inconel 718 in the LPBF process. The simulation study concluded that the development of a melt pool is affected by the process parameters whereby a larger beam power and slower speed will cause an increase in the distance at which the melt pool reaches a quasi-steady state. Obidigbo [86] studied the melt pool dimension of Invar36 using numerical and experimental approaches. The thesis concluded that the transient length varies with the

change in process parameter and speed has more effect on the initial state of the melt pool. Powder particles are not included in both studies.

Studies have shown that the dimensional accuracy, porosity as well as the microstructure for thin features are different compared to the bulk structures [75, 87]. The thin feature structures have different thermal histories and can have a significant effect due to changes in scan parameters, powder size, and distribution. This size effect in the metal LBPF is largely unexplored. The aim of this study is to generate enough data and information to understand the variations in smaller scan lengths to build three-dimensional struts and lattice-included structures with higher dimensional accuracy and reliable quality. Overall, there are four scenarios; (a) melt pool for small features (b) smaller scan lengths due to the scan strategy (c) melt pool at the start and end of long scans (d) melt pool at laser turn points in powder bed fusion process where we can observe a transient state of the melt pool. Single tracks of small scan lengths built with skywriting ON is investigated in this paper.

5.2 Experimental Details

In this study, single tracks with lengths less than and equal to 2 mm are fabricated. The single tracks are built with Ti-6Al-4V powder particles in the EOS M270 machine. The machine is equipped with a 200-Watt Continuous wave Ytterbium fiber laser. The laser beam diameter used in this study is 100 microns. The build was completed with Skywriting ON option. The acceleration and deceleration of the laser does not occur during the scan of the single tracks. The single track information from the as-built part i.e., without

any post-processing, is captured using a white light interferometer (WLI) scan. The data acquired from the WLI scan of the single track is processed using MATLAB.

5.3 Sample design and fabrication

A semi-cylindrical design was chosen instead of a rectangular design to save material and to build the single-track deposits at a certain height instead of on the build plate. Figure 5.1 shows the basic design and dimension of the sample. The sample has raised walls on either side along the length with notches. The single tracks were arranged in between those notches.

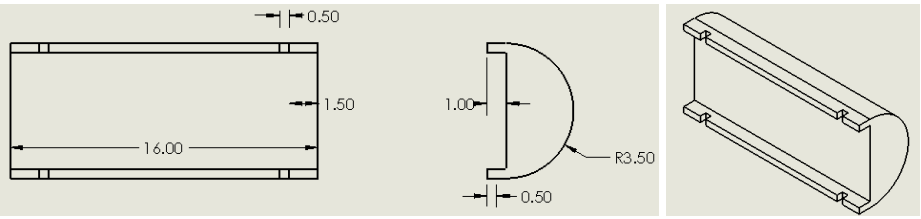

Figure 5.1 Semi- cylindrical sample with raised walls on either side (Top, side, and Isometric view).

5.3.1 Variable power and scan speed sample

Three levels of power and three levels of scan speed was chosen for the experiment. Table 1 lists the laser power and scan speed combination used in the experiment. Thirty six tracks were arranged in two semi-cylindrical samples i.e., samples X and Y. The arrangement of tracks in sample Y is shown in Figure 5.2 below. Tracks with linear energy density (LED) less than 1 were created at a 1 mm gap and with LED greater than 1 were designed at a 2 mm gap. The tracks with LED greater than 1 were kept in Sample Y. A

number and letter code was used to identify the parameters and track length respectively. For example in P1A, P1 represents the parameter combination 1 i.e., power 50 W and a scan speed of 100 mm/s and A represents the scan length of 0.25 mm. Parameter combination coding is also presented in Table 5.1. For scan length, the letters A, B, C, and D indicate 0.25, 0.5, 1, and 2 mm lengths respectively. Ten replicates were built for both samples X and Y in three separate builds. Apart from the single-track deposits, the semi-cylindrical samples were built with default parameters. Images of the samples on the build plate and zoomed view of one of the sample Y is shown in Figure 5.3.

Table 5.1 Scan parameters and linear energy density for the nine parameter combinations.

Speed (mm/s)	100	550	1000
Power (W)	Linear energy density (J/mm)		
50	0.500 (P1)	0.091 (P2)	0.050 (P3)
125	1.250 (P4)	0.227 (P5)	0.125 (P6)
195	1.950 (P7)	0.355 (P8)	0.195 (P9)

Figure 5.2 Top view of the single tracks of length 0.25,0.5,1 and 2 mm arranged in samples X and Y.

Figure 5.3 Five sets of Samples X and Y on the build plate (left), Zoomed view of the sample Y showing the single tracks (right).

5.3.2 Constant scan speed and constant linear energy density (LED) samples

Even for the same linear energy density, the single tracks in the LPBF process, show variation in the melt track geometry [88]. Therefore, single tracks with more combination of power and scan speed are built based on the constant scan speed and constant linear energy density scenarios. A preliminary study, published in [89], showed that the melt pool does not achieve a quasi-steady state in 0.25 and 0.5 mm scan length. Therefore, only 2 mm scan length was included in the design of these samples. Ten replicates were built in the experiment. Table 5.2 lists the parameter combinations based on constant scan speed and constant linear energy density cases. Table 5.3 lists the scan length, number of builds, and the total number of replicates from the two experiments.

Table 5.2 Scan parameters and linear energy density for the parameter combinations.

	P10	P11	P12	P13	P14	P15	
Power (W)	40	80	120	160	195	100	
Speed (mm/s)	200	200	200	200	200	200	Constant Speed
LED (J/mm)	0.2	0.4	0.6	0.8	0.975	0.5	

	P16	P17	P18	P19	P20	
Power (W)	40	80	120	160	195	
Speed (mm/s)	200	400	600	800	1000	
LED (J/mm)	0.2	0.2	0.2	0.2	0.195	Constant LED

Table 5.3 Scan length, number of builds and total replicates in the two stages of the experiment.

Experiment stage	Scan lengths (mm)	No. of builds	No. of replicates
1	0.25, 0.5, 1 , 2	3	10
2	2	1	10

5.4 Single-tracks surface morphology

A white light interferometer, NT1100 from Veeco Metrology, was used to collect the data of the single tracks. The instrument was calibrated using a 10 µm step-height standard. Vertical scanning interferometry (VSI) measurement mode was chosen with an objective lens of 50X and a 0.5X field of view lens. This gives an effective field of view of 0.25 mm * 0.19 mm. Therefore, multiple scans had to be done to capture the entire melt track of scan lengths 0.25, 0.5, 1, and 2 mm in a single image. Multiple scans with a back scan of 250 µm and rectangular stitching function were used to acquire the data. The pixel resolution of the acquired image is 339.5 nm in the X-axis and 396 nm in the Y-axis. Figure 5.4 Sample setup for the measurement. shows the sample setup for measurements. The semi-cylindrical sample is placed on the clay to avoid any sample movement in the duration of the WLI scan.

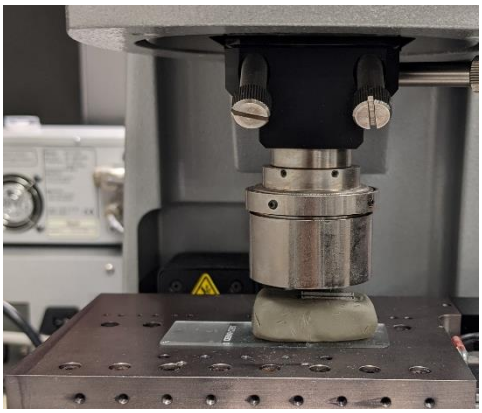

Figure 5.4 Sample setup for the measurement.

5.5 Data processing and width measurement

A typical image result from the WLI scan is shown in Figure 5.5 Image representation of the raw data acquired from the WLI scan for a typical 2mm scan length case.. The black dots in the image are the pixels for which the scan did not acquire data. The bad pixel areas up to 35-pixel points are restored using data interpolation. A typical restored image result is shown in Figure 5.6. Figure 5.7 shows the top and isometric rendered view of the surface height.

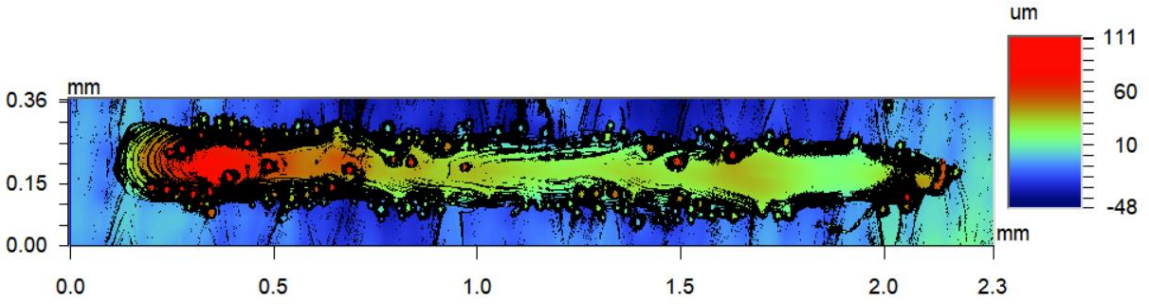

Figure 5.5 Image representation of the raw data acquired from the WLI scan for a typical 2mm scan length case.

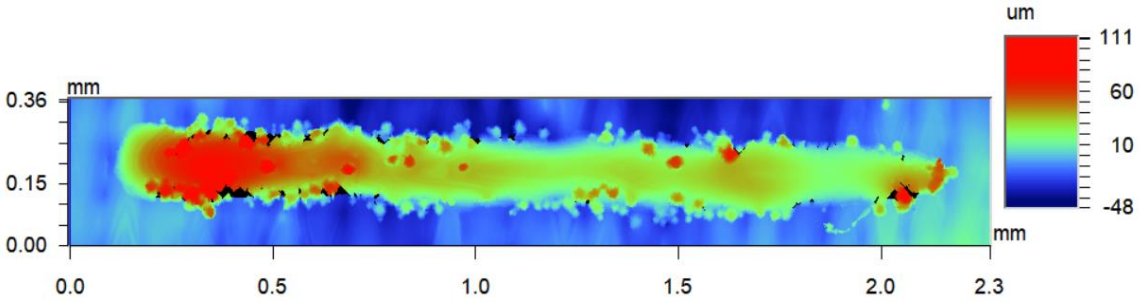

Figure 5.6 Image after the data restoration.

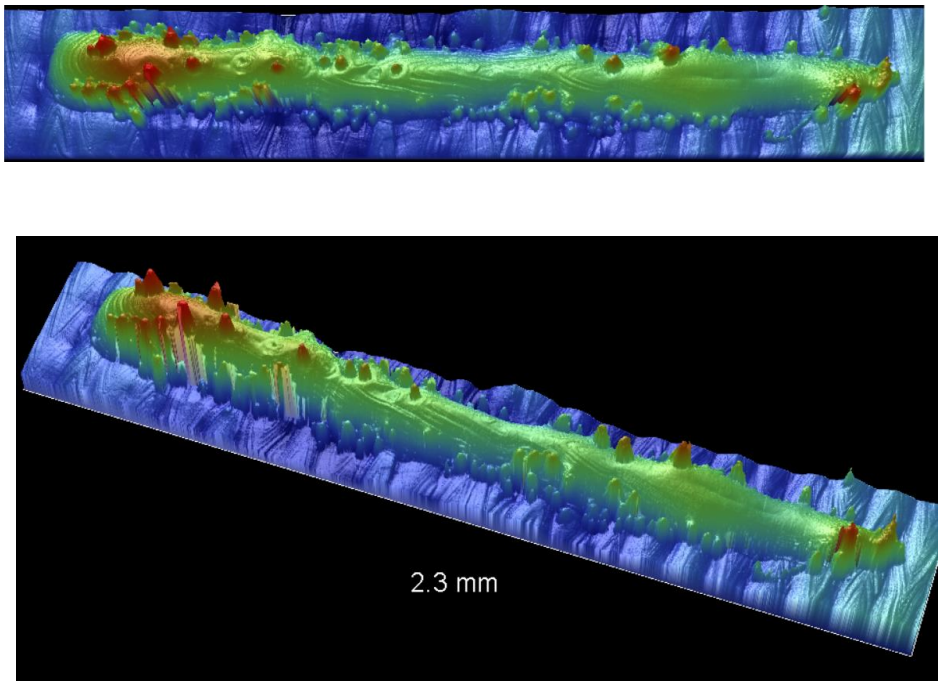

Figure 5.7 Rendered display of the melt track (top view and isometric view).

MATLAB was used to calculate the width of the deposited single tracks. The restored data matrix from the WLI scan was imported into the MATLAB. Each data in the matrix represents the surface height value for a pixel of length 0.34 µm (339.5 nm) and width 0.39 µm (396 nm). A cutoff value was used to separate the melt track from the surface over which the track is deposited. The cutoff value was established by reviewing the surface height data of the first and last five columns and rows from the matrix. In an ideal case, the

minimum value from those twenty surface height data was chosen as the cutoff value. The data obtained after applying the cutoff value is stored as a separate matrix data and considered as the melt track. The surface height data imported from WLI scan result in the MATLAB is shown in Figure 5.8. Figure 5.9 represents the separated melt track after applying the cutoff value. The numbers on the X- and Y-axis in this figure represents the column and row number respectively instead of the track dimensions. Melt track width is calculated from the separated melt track matrix data by subtracting the lower row number which indicates the lower end of the melt track from higher row number which indicates the upper end of the melt track in each column. This gives a width value for each data column in the matrix.

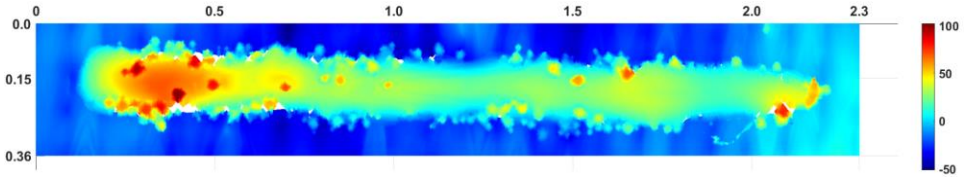

Figure 5.8 Surface height plotted from the entire data in the MATLAB.

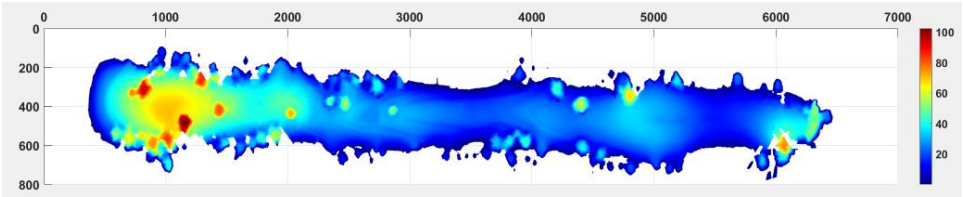

Figure 5.9 Top view of the melt track after data filtering.

5.6 Results and Discussion

A typical single track deposited from the LPBF process has a higher width and a bump/protrusion at the start of the track, followed by a decrease in surface height and slight variation in width along the scan length, and finally a depression at the end i.e., comparatively lower surface height. The single track can be separated into a transient and a quasi-steady state region. The length of the transient region is different according to the process parameters. Thousands of scans are required to build a part from the LPBF process. So, even though the transient regions are small it can significantly affect the properties of the built part. Furthermore, the bump at the start of the track can interfere with the recoater blade during the powder spreading process. And the depression at the end of the track will result in higher powder layer thickness for the next layer of scan.

5.6.1 WLI scan images

Results from WLI scan images for nine parameters from one replicate is presented in this section. The scan direction is from left to right. Parameter combinations P2 and P3 did not produce a continuous single track and was not considered for the melt track geometry analysis. Single tracks for the rest of the seven cases, shows higher surface height with semi-rounded shape while the end of the melt track is flat and has low surface height. There are powder inclusions attached to the edges of the tracks on either side as well as on other regions.

The graph in Figure 5.10 shows the process window for Ti64 powder particles [88]. The curves in the graph separate the regions for parameters that results in parts formed with over heating (OH), over melting (OM), fully dense (FD) and incomplete melting (IM) of

the powder particles respectively [88]. Parameters P2 and P3 do not form a continuous single track because of the low power and higher scan speed. It results in an incomplete melting of powder particles as seen in Figure 5.11. Parameters P4 and P7 have lower scan speed of 100 mm/s and high power values. The temperature in the melt pool goes beyond the melting pool of the powder particles because of the overheating. The single tracks formed from these paramters have a significant depression at the end with a region with lower surface height before the end of the melt pool as shown in Figure 5.12abd Figure 5.13. According to the reference [88], parameters P1, P5 and P8 results in parts with measurable porosity values whereas parts made using parameters P6 and P9 are fully dense. The top view of the single tracks from these paramteres is shown in Figure 5.14and Figure 5.15 respectively.

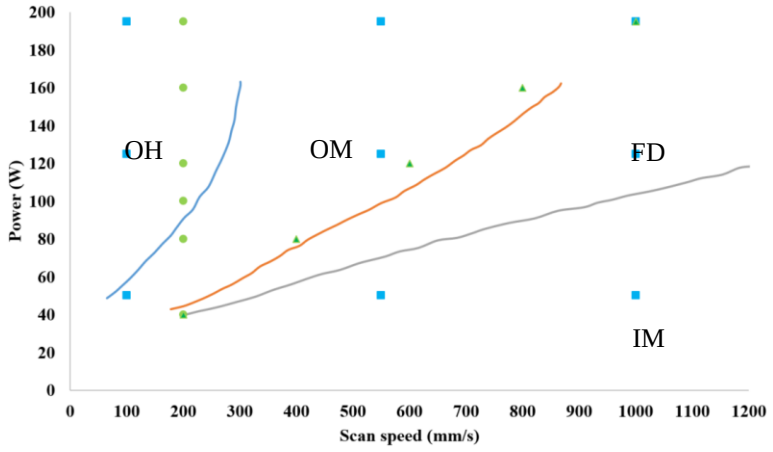

Figure 5.10 Process window for LBPF process using Ti64 powder particles [71].

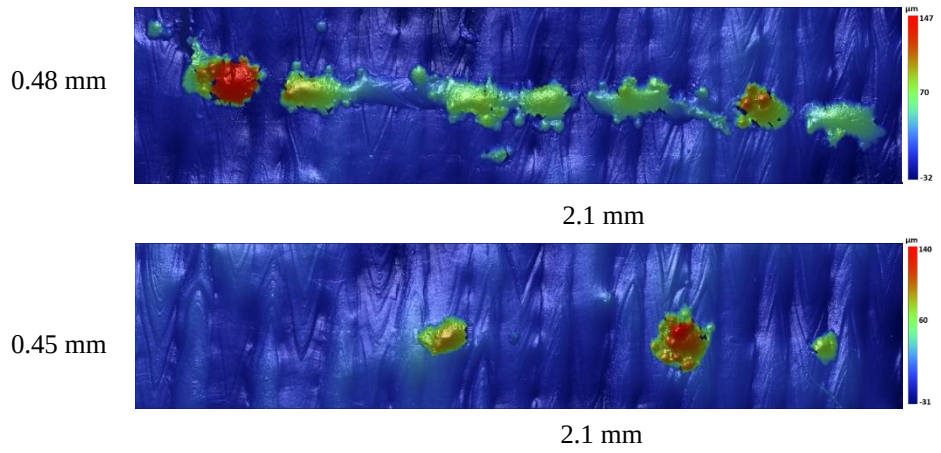

Figure 5.11 Incomplete tracks from parameter combination P2 (top) and P3 (bottom).

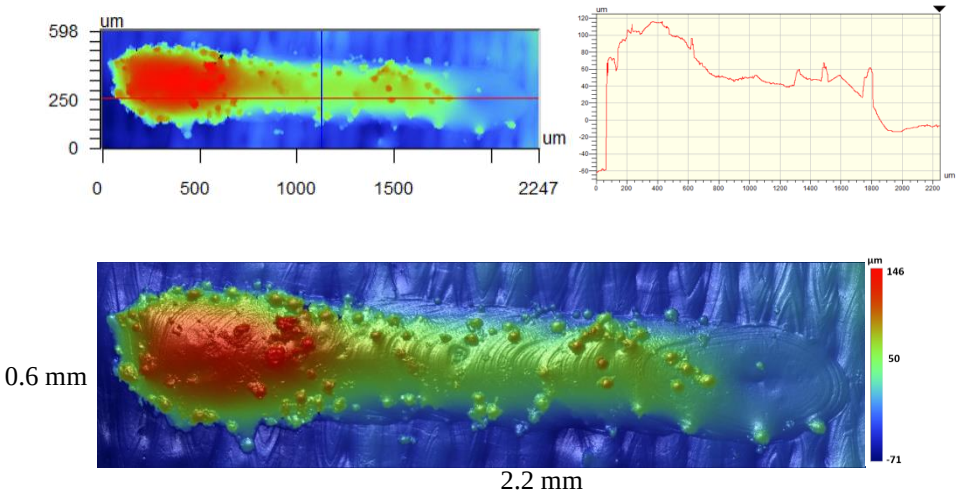

Figure 5.12 Single track from parameter P4 showing data restored image, y-profile section and top view of the rendered image.

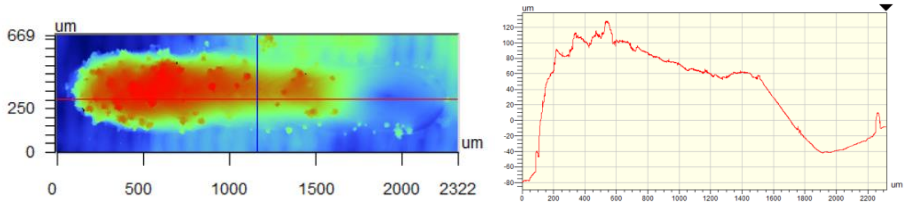

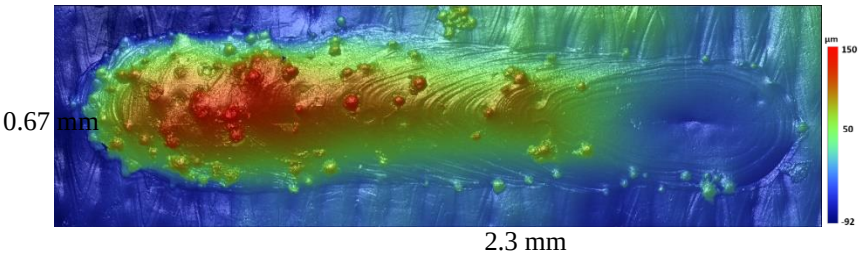

Figure 5.13 Single track from parameter P7 showing data restored image, y-profile section and top view of the rendered image.

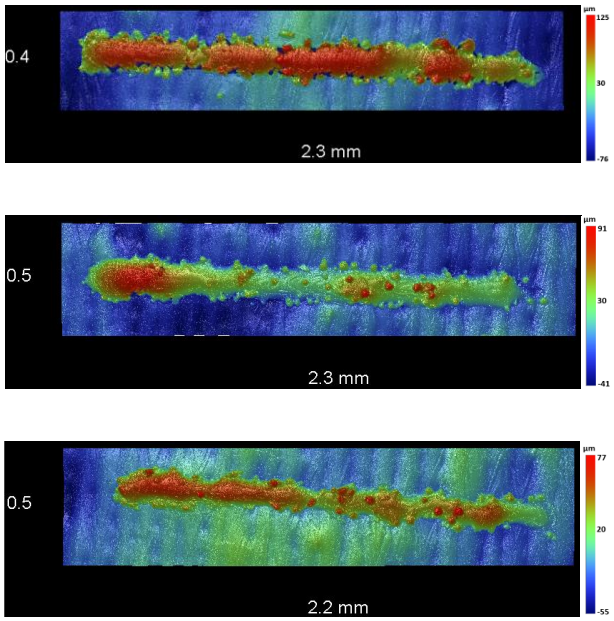

Figure 5.14 Rendered image of single tracks from parameters P1, P5 and P8 respectively

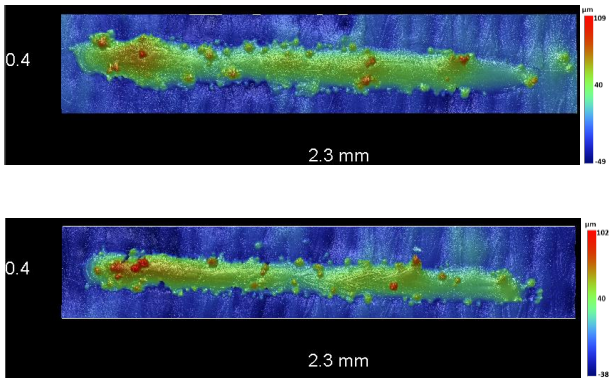

Figure 5.15 Rendered image of single tracks from parameters P6 and P9 respectively

5.6.2 Melt track width and cross-section

Melt track width was calculated after filtering out the single-track data from the data matrix imported from WLI. A single cutoff value was used to separate the melt track data. After filtering, the data points with surface height less than cutoff value were removed and only the single track is stored in a separate data matrix. It is understood that using one single cutoff value can introduce errors in some data columns because of the variable surface height all around the track. Each column has a surface height data for a pixel of length 339.5 nm. And only the initial portion of the melt track is considered to find out the transient length. Taking these factors into consideration and after reviewing the melt track curve at different cross-sections, it was established that the error will be minimum at the start of the track. Therefore, a single cutoff value was considered suitable to separate the melt track to find the transient length at this stage of the study. Because of the tilt in the acquired data, the width values in certain columns will be slightly lower. But it does not have a significant effect on the transient length value. Figure 5.16 shows the melt track cross-section of 100 columns of data (from 0.187725 mm to 0.221671 mm, 0.033946 mm length) at the start of the track before and after filtering for the case P8C discussed in section 2.3. The melt track width for these data columns is around 220µm.

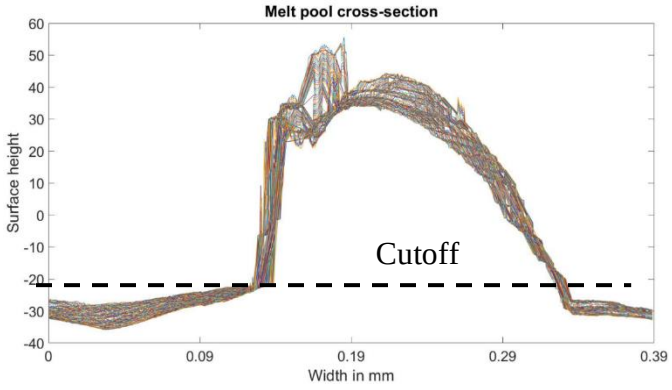

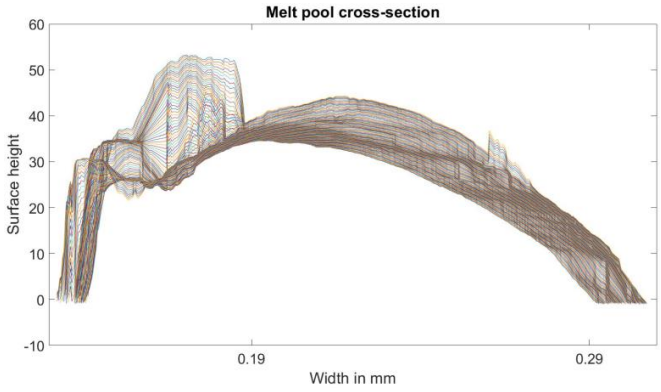

Figure 5.16 Melt track cross-section from 100 data columns before and after filtering.

From the images of single tracks in section 3.1, it is clear that the surface height for different parameter combinations is quite different. Therefore, a simple comparison of the surface height between parameter combination with lowest energy density P6 and highest energy density P7 is performed. Parameter combinations P2 and P3 are excluded while considering the lowest energy density because they did not produce a complete and consistent single track. Cross-section from a single data column in the middle region of the track is plotted in the graph presented in Figure 5.17. The graph shows that the single tracks from parameter P7 has a wider melt track (~ 0.43 mm) compared to parameter P6 (~ 0.11 mm) for the same scan length.

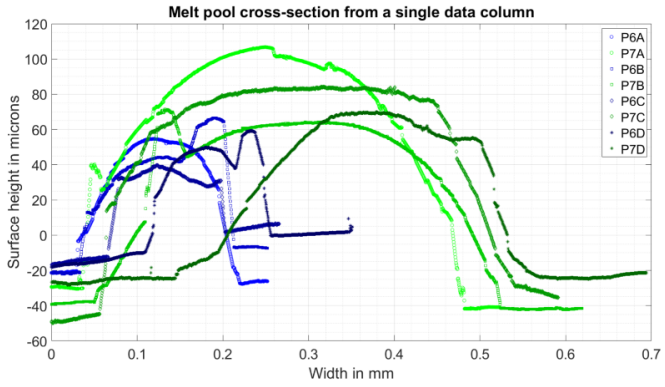

Figure 5.17 Graph showing the surface height variation as well as melt track width variation between parameter combinations P6 and P7.

The melt track shape at the start and end region of the single tracks shows different characteristics compared to the steady-state region. The melt track cross-section across the width at four different regions for the case P7D is plotted. The melt track cross-section from five adjacent data columns near the start of the track (at 0.0577 mm), the middle region of the track (at 0.9572 and 1.1270 mm) and near the end of the track (at 1.9926 mm) is plotted in Figure 5.18. The melt track width slowly starts to increase from the start zone and reaches a steady- state in the middle region showing a semi-round shape. The melt track width increases from approximately 0.22 mm to 0.50 mm. The end zone of the track is flat, and the surface height matches the surface around it.

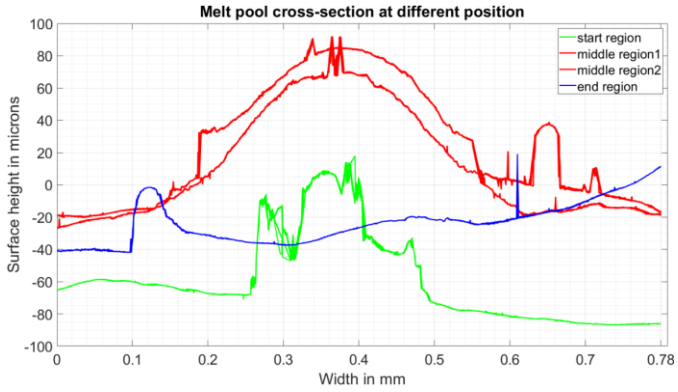

Figure 5.18 Melt track cross-section at the start, the middle (2 points) and the end region.

5.6.3 Transient length in single tracks

The melt track width along the scan length is calculated based on the algorithm implemented in the MATLAB. Width along the scan length was analyzed for all 28 cases, excluding 8 cases of parameters P2 and P3, of replicate 1. Melt track width of tracks with four different scan lengths for parameter P6 is shown in Figure 5.19. The melt track width for tracks with scan lengths of 0.25 and 0.5 mm does not reach a steady width value. The width peaks around 220 µm scan length for both cases. For scan lengths of 1 and 2 mm the melt track width increases up to 410 and 450 µm respectively. This is the transient length (TL) after which the melt track width becomes steady. The melt track width shows slight fluctuation for tracks with scan length 1 mm and 2 mm even in the quasi-steady state. This variation in the melt track width is mostly due to the powder attached to the edges of the melt track. Because of the attached powder particles, we do not observe a constant width value even after the transient length. For this study, the transient length is defined as the position where a second peak width value is located in the scan length vs width graph. The second peak in the graph is the first peak point after the melt track width decreases to its

lowest value and then starts to increase again. Figure 5.20 shows the calculated melt track width along the scan length for a 2 mm scan for 3 replicates. The transient length for the three cases is around 650 µm.

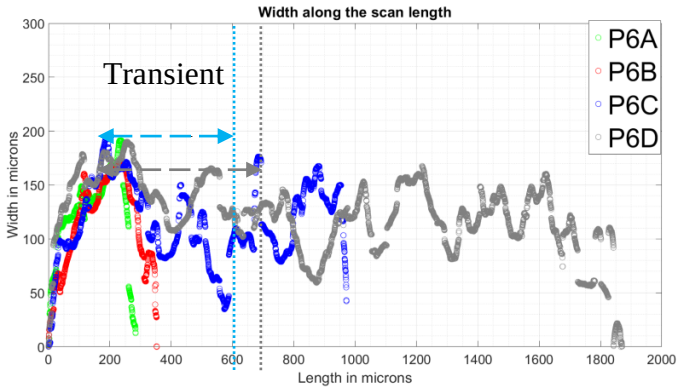

Figure 5.19 Calculated melt track width of tracks for four different scan lengths of parameter case P6.

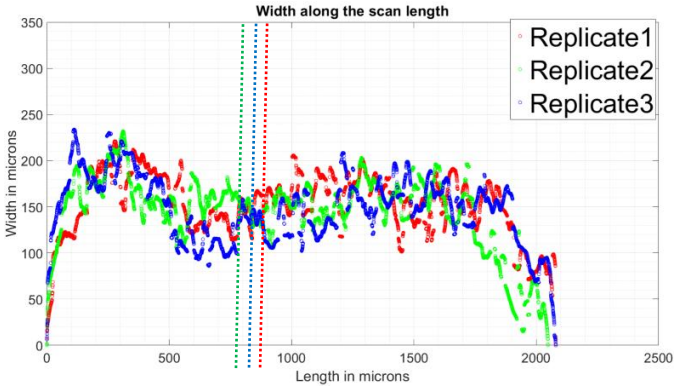

Figure 5.20 Calculated melt track width for 2 mm scan length from 3 replicates for parameter case P5.

The melt track width value of 28 single tracks of replicate 1 is calculated and analyzed. This includes the scan length of 0.25, 0.5, 1 and 2 mm. After reviewing the data, the transient length for some parameter cases was found to be higher than 1 mm. Therefore,

the results from a 2 mm scan length were used to find the transient length for all parameter combinations.

The melt track geometry of the single tracks shows a variation in both the surface height and the melt track width for different process parameters. In addition, the melt track width of a single-track shows variation along the scan length. The variation is more apparent at the start and the end of the single tracks. This is because the melt track is not at a quasi-steady state in that region. Transient length is the scan length from the start of the melt track at which the melt track has achieved a quasi-steady state. In this study, we can observe variation in the melt track width even after the transient length. This is the attribute of the powder attached to the melt track. Only melt track width is considered as the parameter to differentiate between the transient and the quasi-steady state at this stage of the study. The scan length representing the second peak width value in the melt track width vs scan length graph is established as the transient length. The melt track width increases from zero to a certain peak value. After this, the melt track width decreases up to some scan length. It reaches to the lowest width value. Then, there is an increase in the width again. The scan length at this point (peak width value) is identified as the transient length. Although the width value shows some variation (increase and decrease) even after this point. A similar trend is seen for all replicates as shown presented in Figure 5.20 above. The transient length for seven parameter combinations is calculated for nine replicates and the average values with their standard deviation is plotted as shown in Figure 5.21.

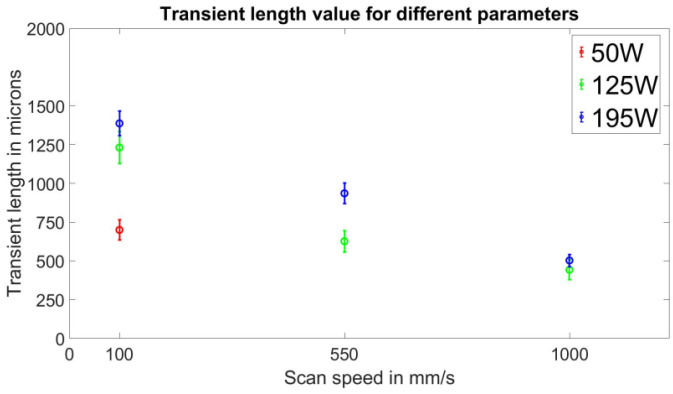

Figure 5.21 Calculated transient length value for seven parameter combinations from nine replicates

The transient length for parameter case P7 is the highest with 1364 microns and P6 is the lowest with 439 microns. The transient length increase with the increase in power for all three scan speeds, whereas the transient length decreases with an increase in speed for all three power cases. Because of the high standard deviation (60 – 100 microns), the transient length values for different parameters show some overlap.

5.6.4 Transient length for constant scan speed

Parameters P10 to P14 corresponds to an increase in power with constant scan speed. The rendered top view of the melt tracks is presented in Figure 5.22. Parameter P 10 does not produce a continuous melt track. The transient length values, presented in Figure 5.23, calculated for P 11 to P14 show that it increases with an increase in the power.

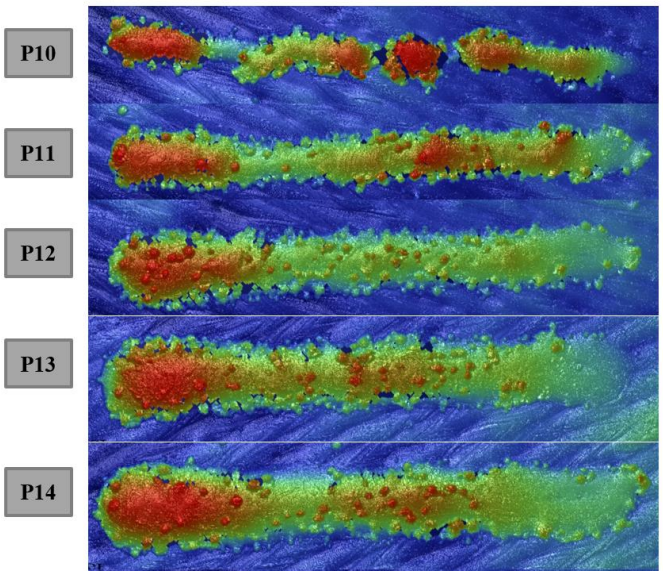

Figure 5.22 Top view of the data restored images (P10-P14) cases obtained from the WLI scans

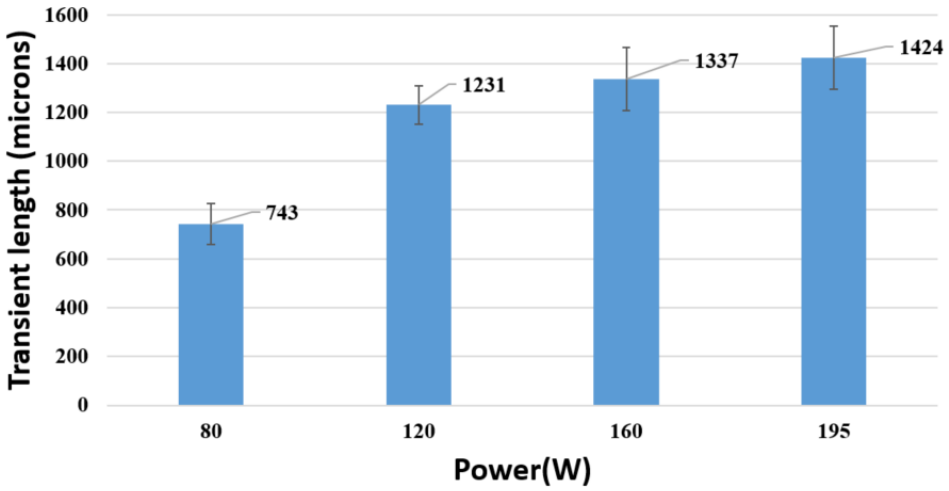

Figure 5.23 Transient length values at a constant scan speed of 200 mm/s for four different power values

5.6.5 Transient length for constant energy density

Parameters P16 to P20 corresponds to constant linear energy density with a change in power and scan speed. Parameter P16 is the same as P10 and does not produce a

continuous melt track. The rendered top view of the melt tracks is presented in Figure 5.24. The transient length values, presented in Figure 5.25, shows that the transient length increases when both the power and scan speed increases for the same linear energy density.

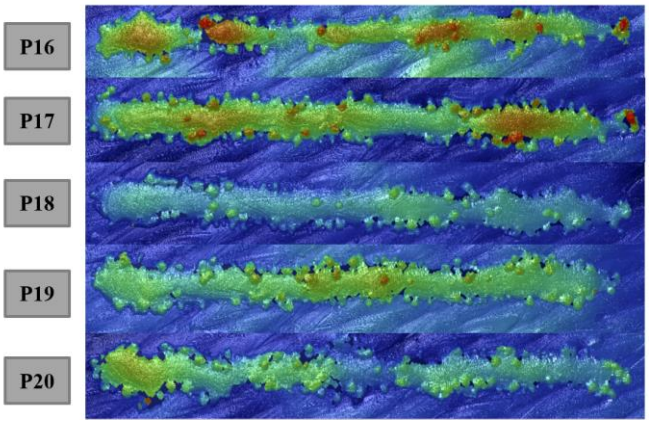

Figure 5.24 Top view of the data restored images (P16-P20) cases obtained from the WLI scans

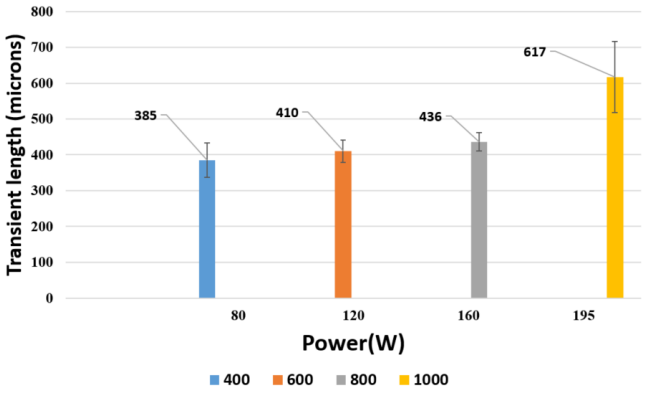

Figure 5.25 Transient length values for a constant linear energy density of 0.2 J/mm.

5.6.6 Transient length for P-V window in EOS machine

There are 19 unique parameters set in the parameter combinations listed in Table 5.2. Among those parameter sets, P2, P3, P10, and P16 did not form a continuous single

track. The transient length for all other parameter cases is presented in Figure 5.26. The transient length is high for high power and low scan speed. The transient length decreased slowly with a decrease in power for a constant scan speed

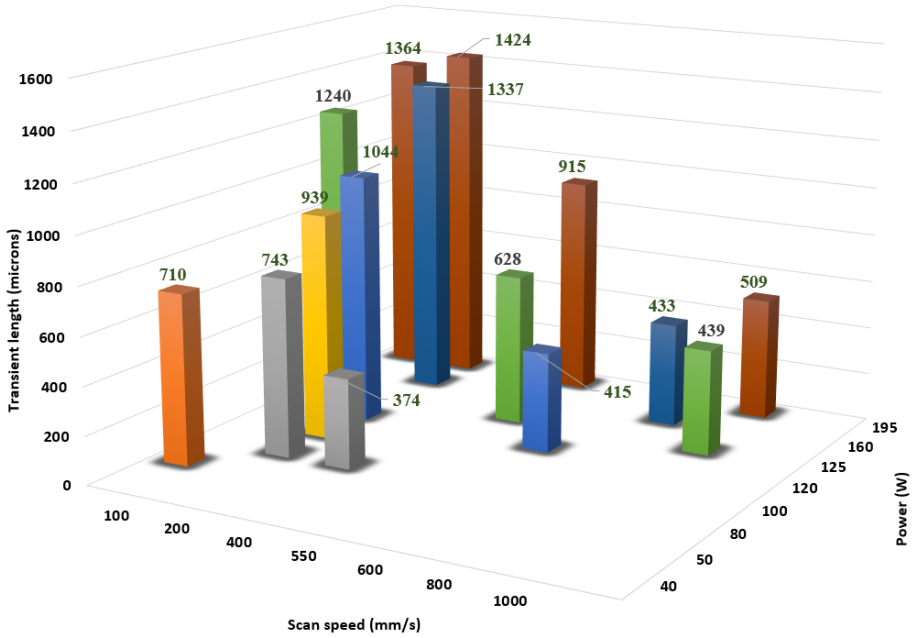

Figure 5.26 Transient length for different power and scan speed

5.7 Conclusion

In this study, single tracks of four scan lengths i.e., 0.25, 0.5,1, and 2 mm are fabricated with Ti-6Al-4V powder particles. Three sets of experiments based on conduction and keyhole mode parameters, constant scan speed parameters, and constant linear energy density parameters were performed. All the single tracks were deposited on semi-cylindrical samples at a height of 6.63 mm from the build plate. WLI scan of the single tracks in as-built conditions were completed to acquire the track geometry information. Melt track cross-section for different parameters at different positions of the

single track is analyzed. An algorithm is implemented in MATLAB to read the data and separate the single tracks from the surface. Melt track width values along the scan length is also generated from the separated data. The transient length is defined and calculated from the processed data. The results obtained can be summarized as

1) A quasi-steady state, as seen in the middle region of the single tracks of 2 mm scan length, is not achieved for smaller scan lengths. The melt pool of 0.25 mm and 0.5mm does not reach a steady state for the process parameters used in this study. Also, some parameter cases do not produce a continuous single track even for 2 mm scan length.

2) The start and the end of the melt tracks are different in terms of both the width and the surface height. Melt track at the start of a single track is a semi-rounded shape with higher surface height. The end of the melt track is almost flat, and the surface height is very low similar to the surface over which the track is deposited.

3) For a constant speed, the increase in power causes an increase in transient length given that other parameters remain unchanged. The relationship is inverse for a constant power i.e., the increase in speed results in a decrease in transient length given that other parameters remain unchanged. Compared to the decreased in power, the increase in scan speed shows a sharper decline in the transient length.

4) The highest value of transient length is 1424 microns for the parameter power 195 W and scan speed 100 mm/s while the lowest value is 315 microns for power 80 W and a scan speed of 400 mm/s.

The powder attached to the melt track adds complexity in separating the single track from the surface. The resolution of the data acquired from WLI is in nanometers while the data for the transient length is in microns. Therefore, the error introduced in the width variation because of the powder particles should not significantly affect the transient length values. In the next step, the uniformity of the melt tracks will be studied in two-dimensional raster-area. Modeling and simulation of the melt track evolution focusing on the start and the end of the tracks will also be carried out.

CHAPTER 6

AN INVESTIGATION INTO MULTI-TRACK DEPOSITION IN LASER POWDER-BED FUSION: TRANSIENT REGIONS ANALYSIS AND SCAN LENGTH EFFECTS

6.1 Introduction

The laser powder bed fusion (L-PBF) process enables the production of complex metallic parts corresponding to layer by layer information from a computer aided design (CAD) model. Each layer of design information is transferred into a machine in which a laser source will melt a layer of 20–100 μm thick metal powder [90]. The process of melting and solidification continues until all the layer's information is completed and a part is built. The properties of that part are highly dependent on the properties of each layer [91]. The layer is basically the raster pattern followed by the laser source in a line [92]. The study of single tracks provides an understanding of the effect of process parameters on the different metal alloys. The study of multiple single tracks with variation in parameters like laser power and scan speed is helpful in finding the optimum process parameters for an alloy [93].

The LPBF process allows a greater degree of freedom in the design of the parts [94] along with the ability to use high grade metal alloys [95]. Furthermore, recent advancement in this technology has enabled the user to create lightweight high-strength [96] and bio-inspired design structures [97], thin walls [98] that cannot be fabricated by conventional

manufacturing processes. Many of these designs can have features with dimensions in the range of 1-2 mm or less. The geometrical accuracy and mechanical properties of these features are different in comparison to the bulk components [99].

The LPBF process involves rapid heating, melting and fluid flow and cooling. There is a complex interaction between the laser and the metallic powder, which is highly affected by the change in process parameters [100] [101]. Wu et al [102] studied the limits of fabricating thin wall structures and explored the factors responsible for the limitations. Tomas et al [103] noticed in their research that the standard stripe scan strategy leads to large deviations in the geometrical accuracy of the thin walled structures. Lu et al [104] studied the warpage in thin-walled structured and concluded that the wall thickness plays an important role on the warpage of the final part. In their study, Yang et al [105] concluded that the longer and taller thin-wall structures are more prone to distortion. The melt pool boundary as well as the microstructures is inconsistent and are not comparable with the bulk components.

The melt pool for long passes will reach a quasi-steady state after the laser beam travels a certain distance provided that the scanning direction is unchanged [106]. The melt pool geometry for small scan length exhibits higher variations. Furthermore, the laser beam goes through a phase of acceleration or deceleration at turn points at which the melt pool exhibits different properties [107].

The presence of a transient region at the start and the end of the laser scan is evident for different materials used with the LPBF process [108-110]. The melt pool geometry in the transient region is different from the quasi-steady region. This difference becomes more

apparent while building structures with thin features in the LBPF process. Many of the small features do not share the same characteristics as the bulk components even if they are built with the same processing parameters. Also, the surface morphology is affected by the transient regions formed during the back-and-forth scanning. This affects the powder layer thickness across the layer during the next layer deposition, which in turn affects the inter-layer fusion. However, there is a lack of study on how the formation of the transient region affects the surface characteristics of different size features. In this regard, a single-layer multi-track experiment is designed to study the formation of the transient regions during raster scanning. Four scan lengths are fabricated with different levels of laser power, scan speed, and hatch spacing values to define the transient length, width, and examine the length effect on the surface characteristics. The surface data is acquired using a white light interferometer and MATLAB is utilized for further analysis.

6.2 Sample Design and Fabrication

The surface characteristics of the raster scan of 2 mm were analyzed in this study. The raster scans were built with Ti-6AL-4V powder particles. Once the parts were built and removed from the build plate, the raster scan information was captured using a white light interferometer. The data acquired from the raster scans were further processed in Matlab.

An experiment was designed to study the effect of power, scan speed, hatch spacing, and scan length on the residual heat effect in the powder bed fusion process. The experiment was carried out in an EOSINT M 270 metal printer. The machine is equipped with a 200 Watt Continuous wave Ytterbium fiber laser. The laser beam diameter in default

conditions is 100 microns. The build was completed with Skywriting ON option. Three levels of power and two levels of scan speed were selected for the experiment. The combination of these power and scan speed produces a continuous track based on the previous experiment of the single tracks [105]. The power and the scan speed along with the linear energy density values is listed in Table 6.1. Four levels of hatch spacing that allows varying degree of overlap on the subsequent tracks over the range of six different linear energy density were included. The powder layer thickness is 30 μm.

Table 6.2 lists the four levels of hatch spacing and four levels of scan lengths used in the experiment. Ninety-six unique raster scans, as presented in Table 6.3 were built from the combination of these parameters.

Table 6.1 Power and scan speed used in the experiment.

	Scan speed (mm/s)	
	550	1000
Power (W)	Linear energy density (J/mm)	
125	0.227	0.125
160	0.291	0.160
195	0.355	0.195

Table 6.2 Hatch spacing values and scan lengths used in the experiment.

Scan length (mm)	0.25	0.5	1	2
Hatch Spacing (μm)	80	100	120	140

Table 6.3 Number of levels of parameters

	Power	Scan speed	Scan length	Hatch spacing	Total unique
Level	3	2	4	4	96

A semi-cylindrical design was chosen to build the raster scans at a certain height instead of on the build plate. The intent was to incorporate the variations of the powder distribution in a powder bed fusion process. Twenty-four unique raster scans from three level of power, two levels of scan speed and four levels of scan lengths were arranged on the surface of the semi-cylindrical sample. During the build, one layer of the raster scan was deposited on the top surface of the semi-cylinder. Figure 6.1 shows the schematic of the arrangement of scans of one hatch spacing case Four semi-cylindrical samples with hatch spacing of 80, 100, 120 and 140 µm were built to include all ninety-six unique scans. All the raster scans were built with six scan lines. Four replicates were built for each hatch spacing case. Figure 6.2 shows the design and the dimension of a representative sample. The sample has raised wall on either side along the length to avoid any accidental contact during the data acquisition process as well as notches to mark the position of the scans. Furthermore, the laser scan direction along the raster was set up in two distinct ways. In the first method, the laser scanned the six lines of a single raster scan of 0.25 mm scan length and then move onto the scan of six lines of raster scan of 0.5 mm. Whereas in the second method, the laser will scan the first line along the entire length of the samples followed by the second line in the alternating direction. The laser scan direction alternates

after each scan, as shown in Figure 6.2. This will result in higher delay time for the second line of raster scans.

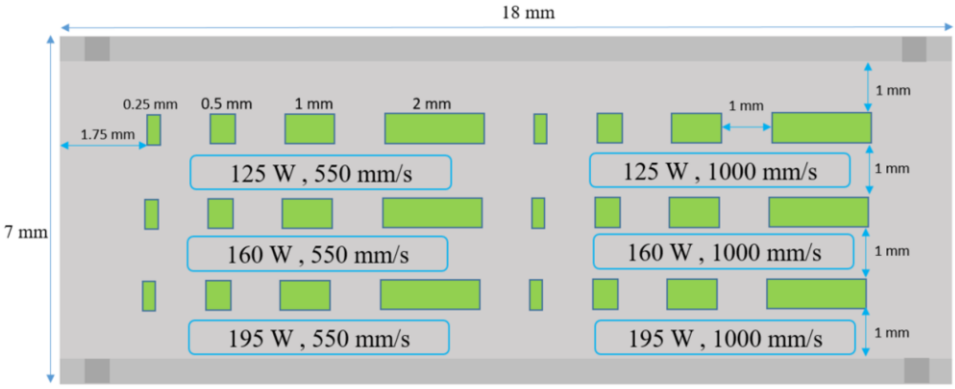

Figure 6.1 Twenty-four raster scan tracks of four different scan lengths arranged on a semi-cylindrical sample for one hatch spacing case.

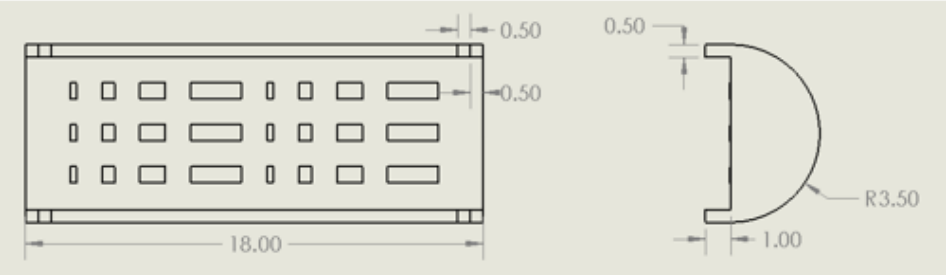

Figure 6.2 Dimension of the semi- cylindrical sample with twenty-four raster scans (Top, and side view).

6.3 Surface data and Acquisition

A non-contact optical profiler, WYKO NT1100 from Veeco Metrology, was used to acquire the surface data of the raster scans. The instrument was calibrated using a 10 µm step-height standard. Vertical scanning interferometry (VSI) measurement mode was

chosen with an objective lens of 50X and a 0.5X field of view lens. This gives an effective field of view of 0.25 mm * 0.19 mm. Therefore, multiple scans had to be done to capture the entire raster area of scan lengths 0.25, 0.5,1, and 2 mm in a single image. The instrument is equipped with a motorized stage for stitching large area measurements. Multiple scans with a back-scan of 250 µm were stitched with a rectangular stitching function to acquire the image of the raster scans. The pixel resolution of the acquired image is approx. 339.5 nm * 396 nm. Figure 6.3 shows the sample setup for measurements. The output data is saved in the WYKO vision analysis software in the form of .opd file extension. The surface height data can be visualized as well as filtered in the vision software. However, the acquired data showed several powder particulates attached to the surface of the raster scans. The data acquired from the scan was filtered using the combination of Vision software and Matlab code to remove the powder particulate from the raster scans. Gaussian filtering with a high pass filter of 0.2 mm was used in the raw data in the vision software. The initial data and the data passed through a high pass filter was compared in MATLAB to obtain the raster scan data without powder particulates. The voids created due to the removal of particulates was filled with a moving median of 500-700. And the edges were be smoothed using median filtering of 50 in MATLAB. The final output in ASCII format was modified to match the. opd format. The output was imported into the vision software to study the metrological difference between the raster scan of different parameters.

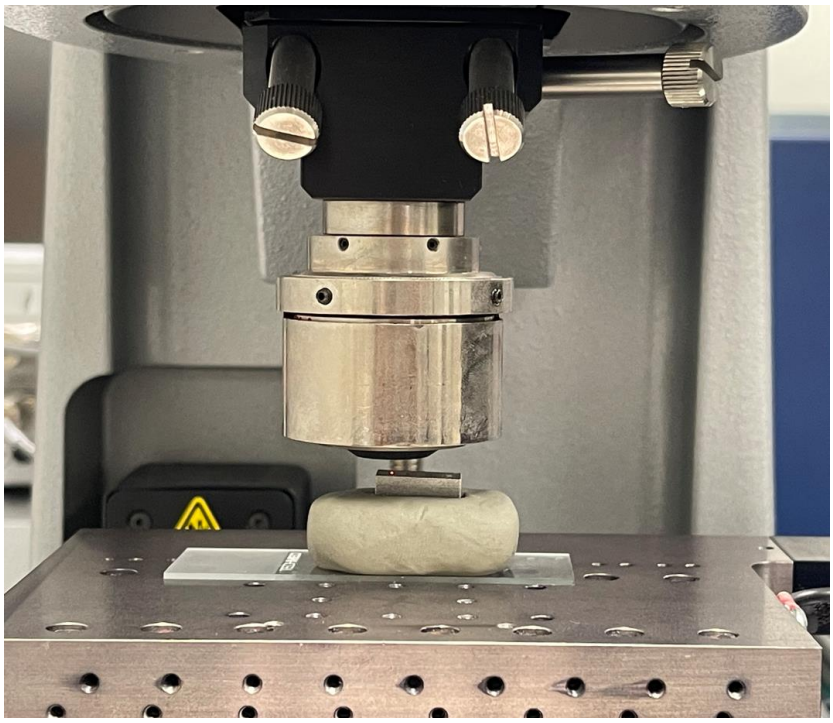

Figure 6.3 Sample setup for the measurement

The optical profiler software provides several options for data filtering. However, selective removal of the powder particles was not possible in one step in the vision software. MATLAB provides more flexibility for data filtering compared to the vision software. The algorithm written in MATLAB was successful in removing the powder particulates and smoothing out the surface height data. The surface height for six lines on the raster scan for all parameter cases was analyzed after importing the filtered data into the vision software. Figure 6.4 shows an example of the raw data obtained from the scan in the optical profiler. The image consists of one data point at every 339.46 nm in the x-direction and 396.05 nm in the y-direction. This sample image has total of 7371 columns and 2783 rows of data points representing the surface height. The black dots on the image are the bad pixel points where the scan could not generate data. The data for those points is filled by using an interpolation of measurement data. An example of the data restored by

using surrounding 35-pixel points is presented in Figure 6.5. Furthermore, the contrast between the tracks and the particulates is observed after the use of a high pass Gaussian filter as shown in Figure 6.6.

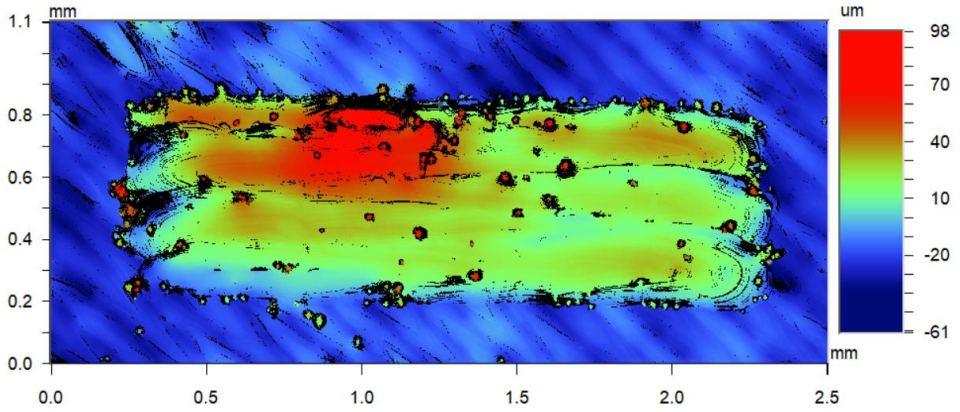

Figure 6.4 Top view of the sample of raw data visualized in the vision software.

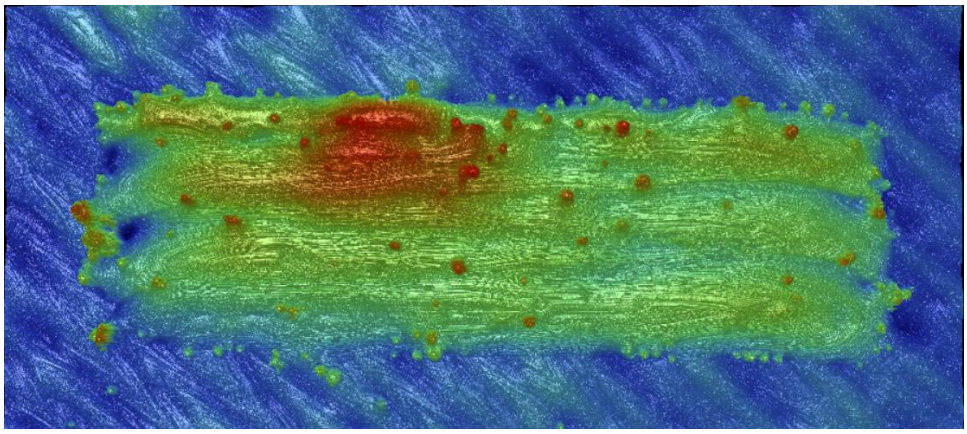

Figure 6.5 Rendered data after restoring the bad pixel points.

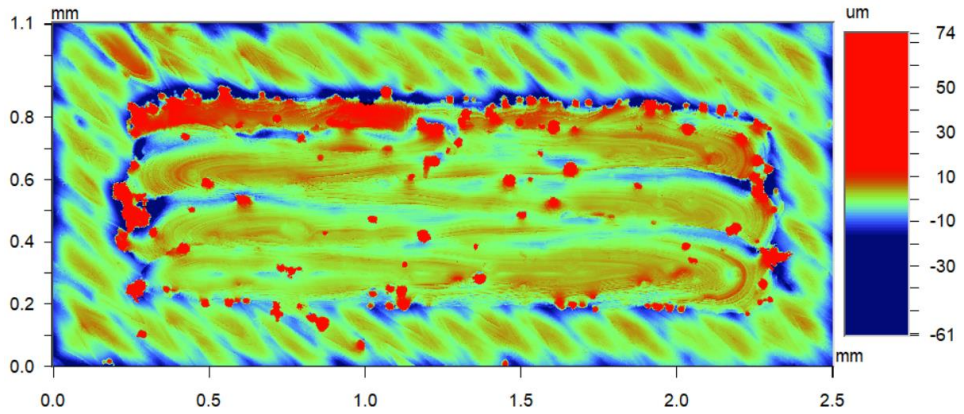

Figure 6.6 Example of high pass Gaussian filtering to contrast the powder particulates.

6.4 Data Smoothing and Filtration

The fabricated multi-tracks consist of randomly distributed powder particles and spatters attached to the surface which affects the surface comparison. Hence, the powder particles are removed to compare the surface statistics. Moreover, the region of interest, in this case, is the six tracks. The six-track region is separated from the substrate, which is the previous layer deposition for the analysis and comparison.

6.4.1 Powder distribution modeling

The surface data is passed through a high pass Gaussian filtering of 0.2 mm. The original surface data and the filtered data is contrasted in MATLAB. A user written code compares the two data and removes the higher surface height using a cutoff value. Figure 6.7 shows the surface data without powder particles plotted in MATLAB. The missing data is filled with a moving median of 500 elements. However, some data spikes are present around the powder particles. To remove the spikes, a third-order one-dimensional median filter of length 50 is applied to the entire data set. The final filtered and smoothed data is

shown in Figure 6.8. This data is then imported into the Vision software for further analysis.

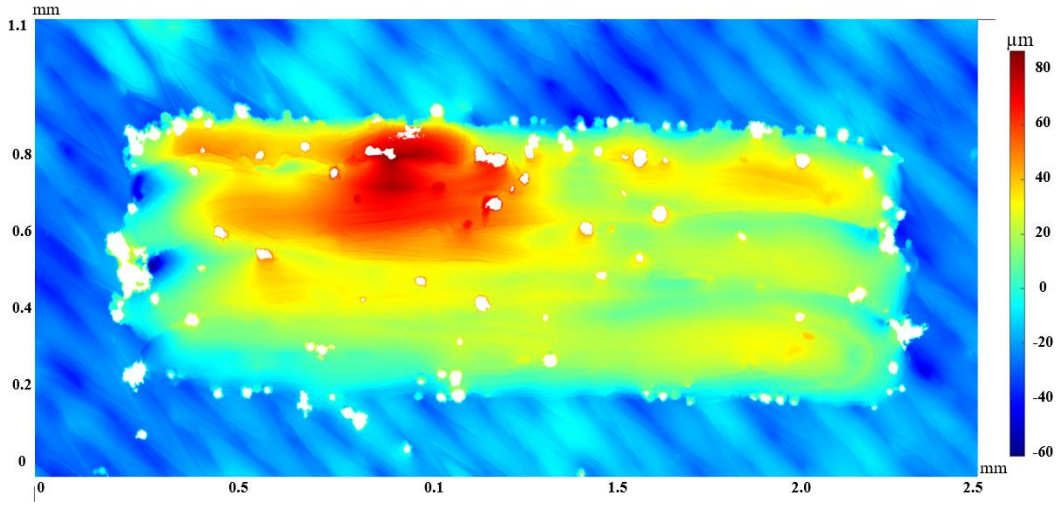

Figure 6.7 Result after the data is removed from the powder particles.

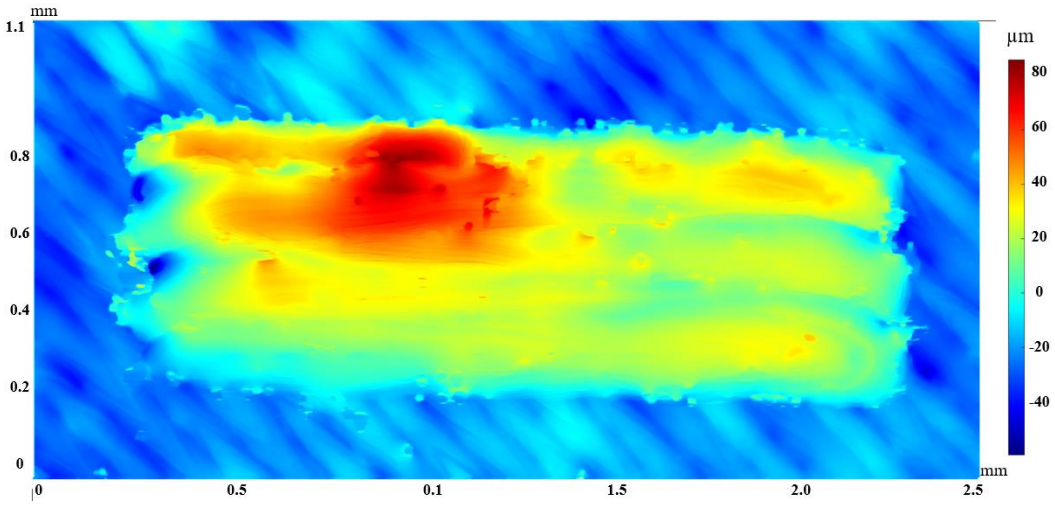

Figure 6.8 Surface height data without the powder particles.

6.4.2 Separating multi-track area from the previous layer data

The multi-track region scanned using the white light interferometer consists of the previous/substrate layer data, which is considered as background in this study. Hence, the background data is removed for the analysis and comparison between different cases. The transition between the two layers is distinct as highlighted in Figure 6.9, which is used as a criterion to separate the six multi-tracks from the background using a MATLAB code.

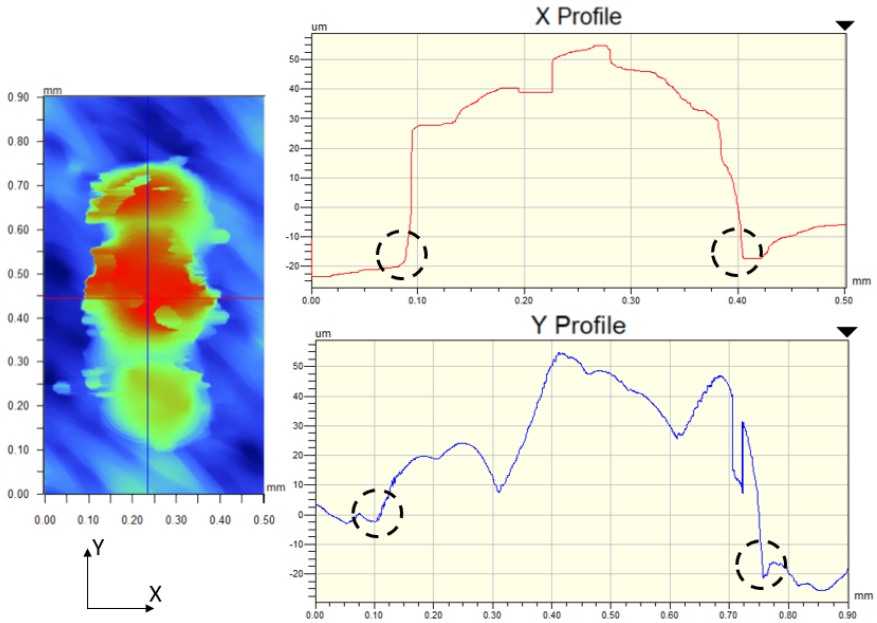

Figure 6.9 Characteristic used to separate the multi-track region from the background.

Four points p1, p2, p3, and p4 are defined, and the search is performed to find the maximum slope for all rows and columns. After identifying the multitrack region based on the slope, the background is then assigned a Nan value. Figure 6.10 shows the separation of the multitrack region from the background for scan lengths of 0.25 mm.

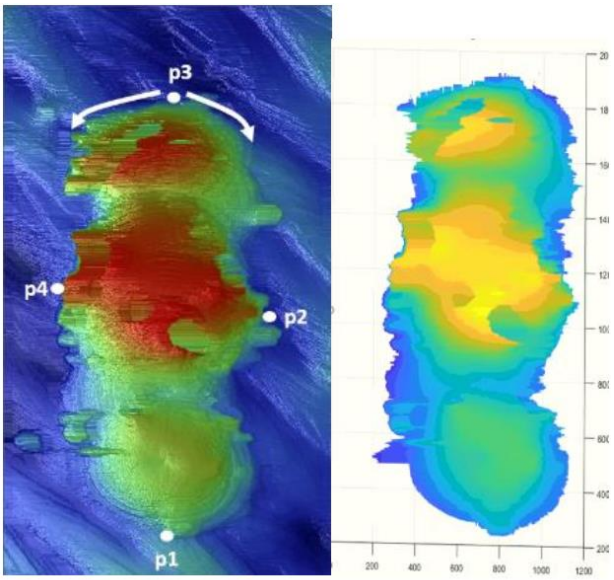

Figure 6.10 Multi-track region isolated from the background using MATLAB for a typical case (125 W laser power, 550 mm/s scan speed, 100 µm hatch spacing, and 0.25 mm scan length)

6.5 Results and Discussion

6.5.1 Length effect on the surface characteristics

After separating the multi-track region, the average area roughness is calculated from all the multi-track data. Figure 6.11 presents the average area roughness along with the standard deviation from four replicates. The effect of laser power, scan speed, and scan length is evident for the 80 µm hatch spacing. In general, the average roughness decreased with increasing scan length, while the roughness increased with increasing power. When the hatch spacing is increased, the trend is not obvious.

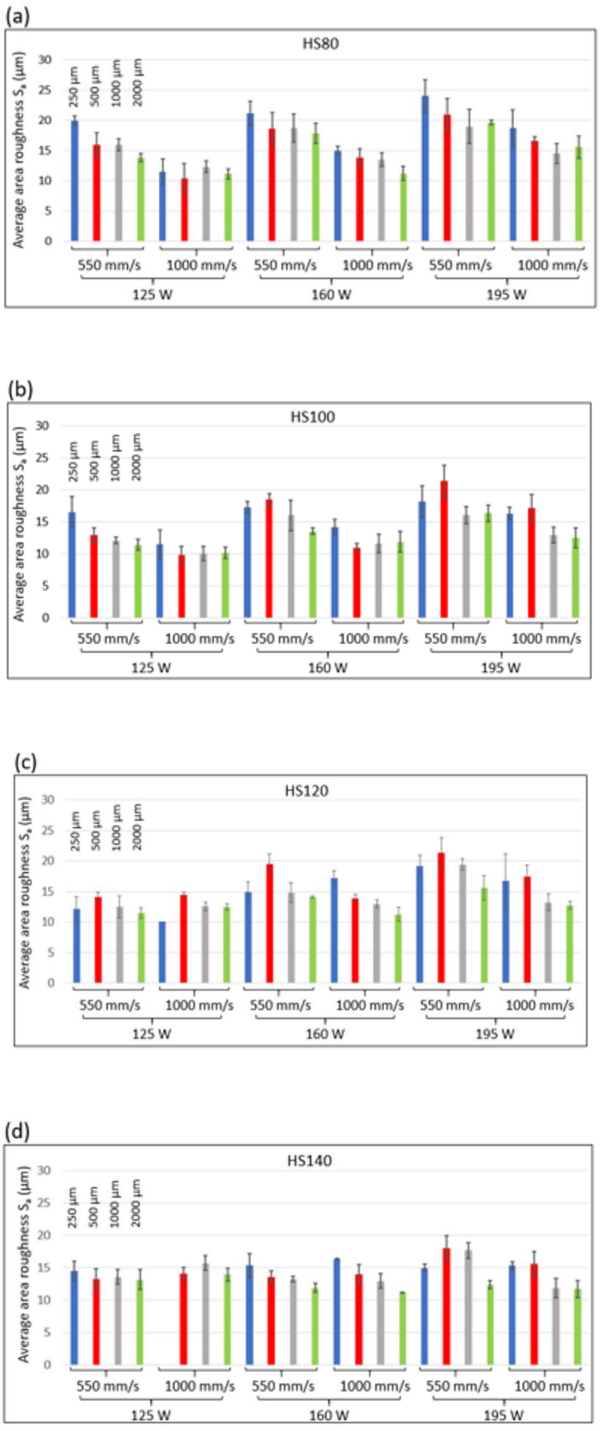

Figure 6.11 Average area roughness at different hatch spacing values: (a) 80 µm, (b) 100 µm, (c) 120 µm, and (d) 140 µm.

The response of the roughness value due to the four different factors was analyzed using the General linear Model in ANOVA with a confidence limit of 95%. The effect of individual factors and their interactions up to 3 levels on the Ra was studied. All four factors have a significant effect on the Ra, based on their zero p-values. The main effects plot shown in Figure 6.12 indicates that an increase in the power maximizes the Ra value while the trend is opposite for the other three factors. However, the hatch spacing (HS) value of 120 μm does not follow the trend. It shows that the Ra value for HS 80 μm will have the highest surface roughness. But HS 120 μm will have higher roughness compared to the HS 100 μm and the HS 140 μm.

The roughness is measured from the six tracks including the transient region. The main effect plot shows that the multi-track roughness is higher for the smaller area with high power and low speed. Single track study showed that the transient length is higher for higher power and lower speed. Thus the result obtained with multi-track provides evidence that the roughness in the multi-track is affected by the formation of transient regions.

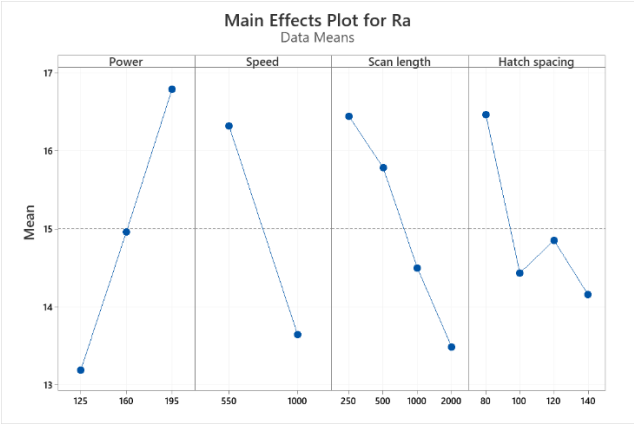

Figure 6.12 Main effect of four factor to the Ra value

The statistical analysis showed the significance of the transient region on the surface roughness of the multi-tracks. The single-track experiment showed that the difference in surface height between transient and steady regions is noticeable [18]. Therefore, the height based comparison is performed. The average transverse height is obtained for all the cases, and Figure 6.13 shows the average height profile along the scan direction for four different scan lengths (195 W laser power, 550 mm/s scan speed, and 80 µm hatch spacing). The area profile shows that the surface is elevated at the center for 0.25 mm and 0.5 mm scan length. However, the elevated surface is present at the two edges in the longer scan lengths. It is also interesting to see that for the majority of the cases, the average height is higher for lower scan lengths. The height of the multi-track would significantly affect the magnitude of the mechanical interaction with the recoater blade during the recoating process. Due to the increased height with smaller feature sizes, the interaction force may be higher, which would only increase the chance of build failure.

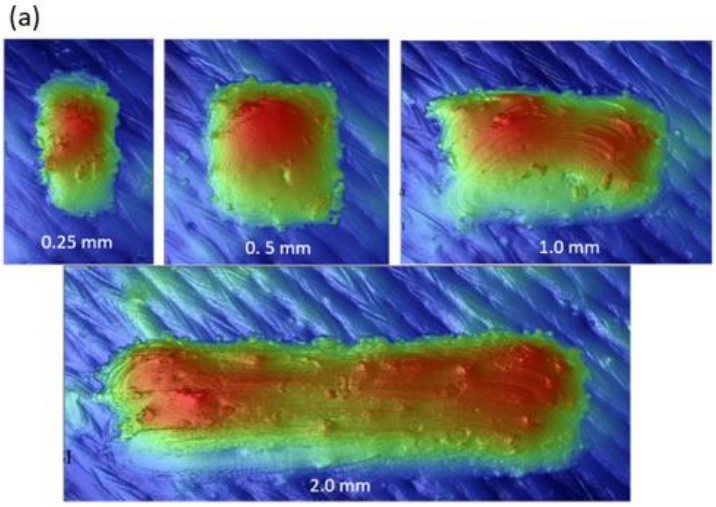

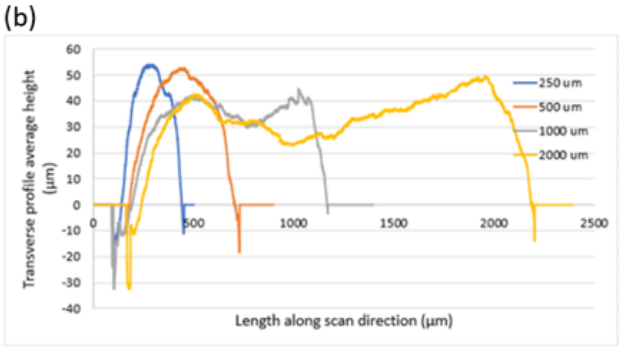

Figure 6.13 (a) Top view and (b) transverse average height along scan direction from 195 W laser power, 550 mm/s scan speed and 80 µm hatch spacing.

Besides the transient region in the scan direction, the presence of transient region along the transverse direction is also of interest for the multi-track. The surface height along the transverse direction is used to identify the transient width. Figure 6.14 shows the top view of the 2 mm long multi-tracks formed with 125 W laser power, 550 mm/s scan speed, and 100 µm hatch spacing. The average height of the longitudinal profiles along the transverse direction is obtained. The error bar indicates the standard deviation. The standard deviation is less than 0.5 for all the profiles.

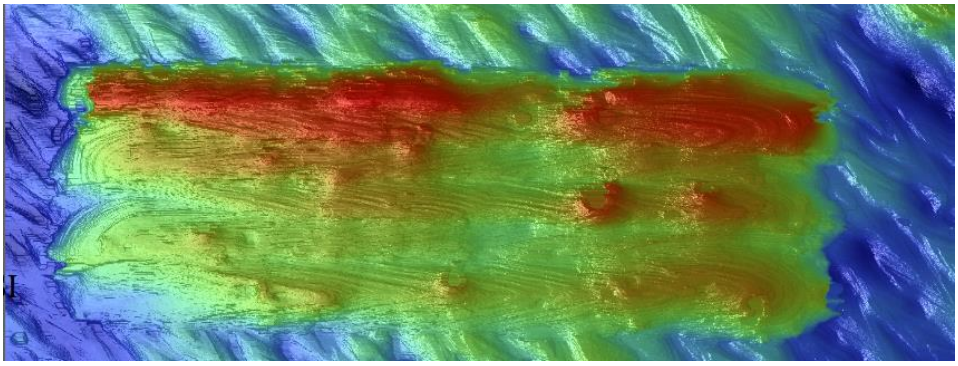

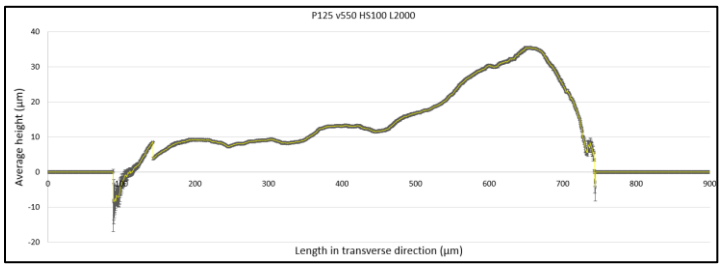

Figure 6.14 Top view of the multitrack and the average height profile obtained from P125 v550 HS100 and L2000.

Figure 6.15 shows the average height profiles from all six power and scan speed combinations with 120 µm hatch spacing. One of the profiles, with the lowest energy density, resulted in a wavy profile. This is due to the presence of a gap between the tracks.

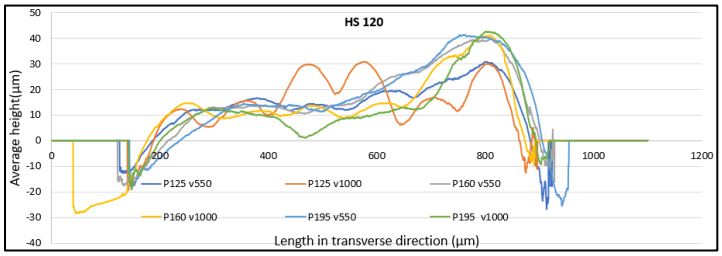

Figure 6.15 Average height profile along transverse direction with 120 µm hatch spacing.

Figure 6.16 presents the top view from all six power and scan speed combinations with 140 µm hatch spacing. Figure 6.17 presents the average height profiles for those cases. In the case of higher hatch spacing, there are more profiles which shows waviness. The tracks with insufficient overlap are removed and the remaining plots are shown in Figure 6.18.

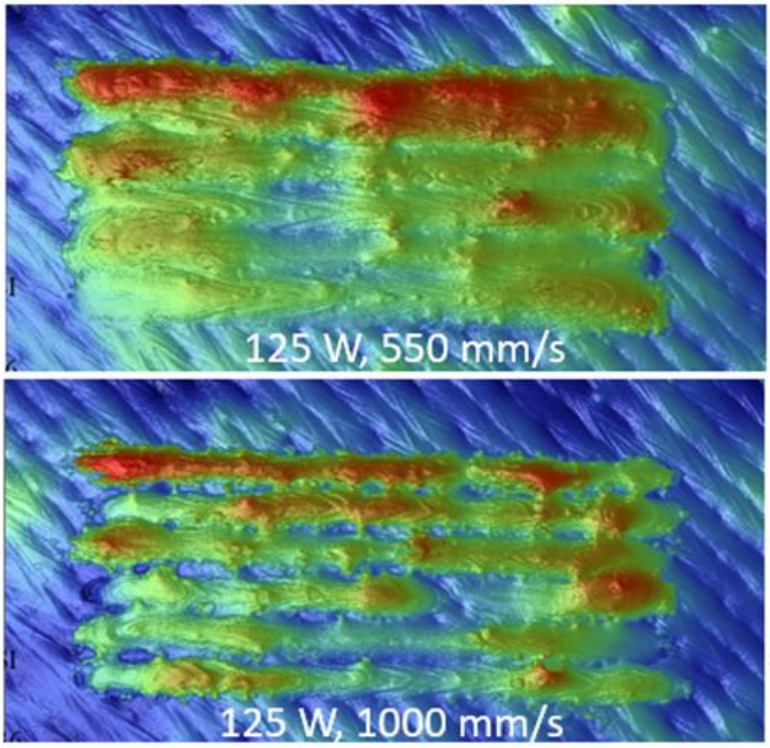
125 W, 550 mm/s
125 W, 1000 mm/s

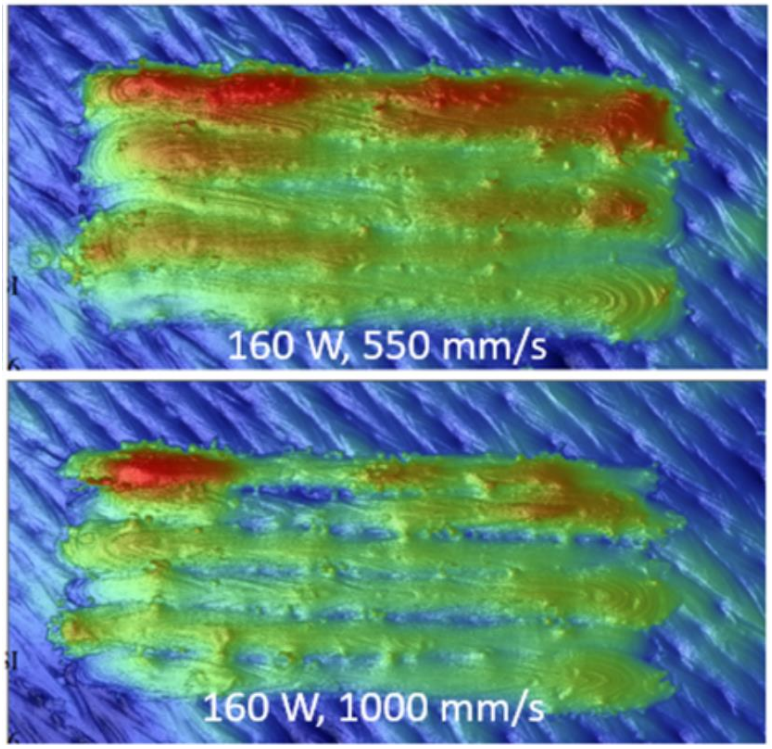
160 W, 550 mm/s
160 W, 1000 mm/s

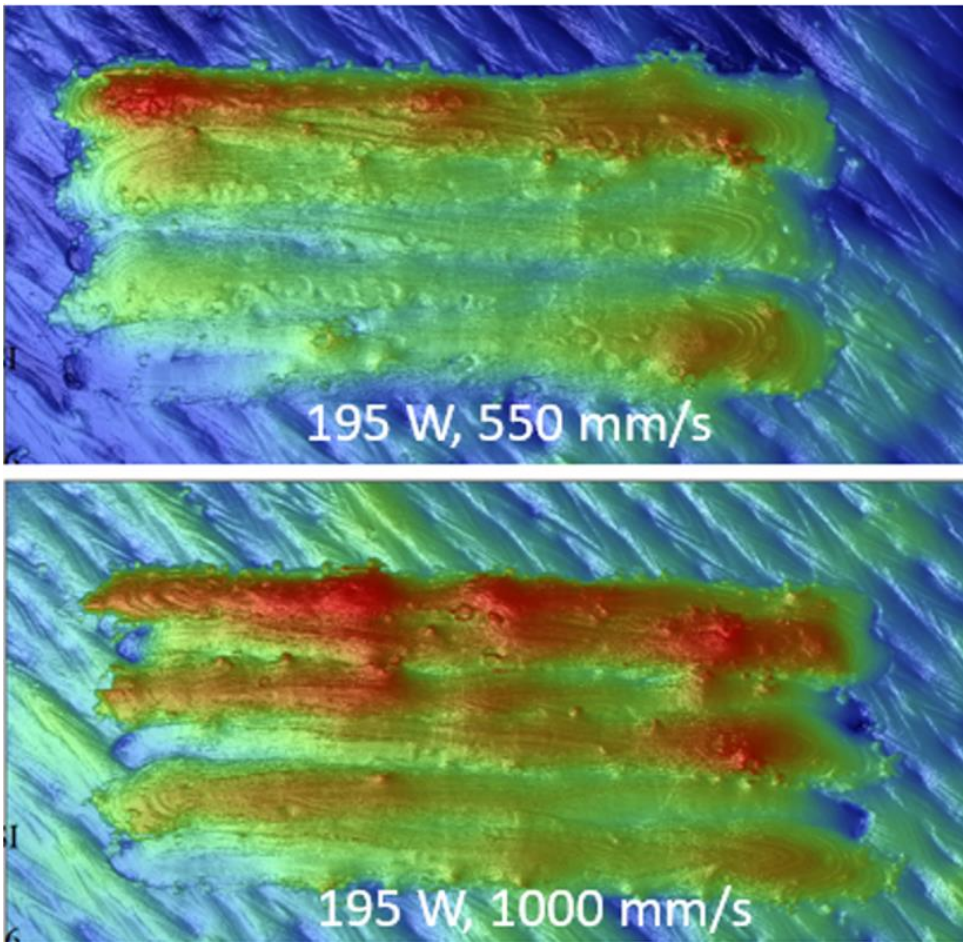

Figure 6.16 Top view of the multitrack with six power and scan speed combination and a hatch spacing of 140 µm.

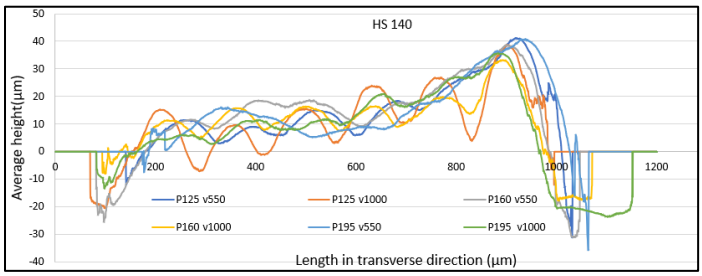

Figure 6.17 The average height profile obtained with 140 µm hatch spacing.

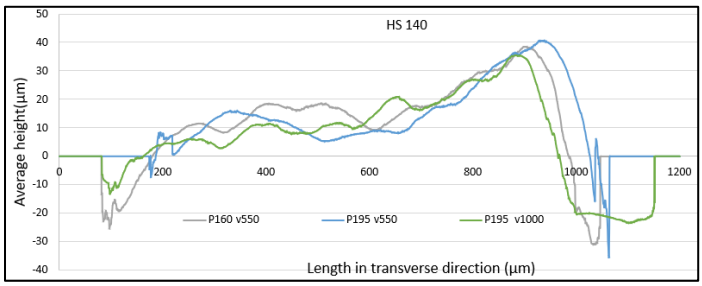

Figure 6.18 Average height profile after removing cases with insufficient overlap between the tracks.

6.5.2 Defining transient region in multi-track

The surface analysis of the multi-tracks showed the presence of transient region in both scan direction and transverse direction. Hence, two terminologies are defined to separate between the transient regions in two directions.

Transient length: The transient region formed along the scan direction is defined as the transient length. The transient length is formed due to the lower initial thermal state of the powder bed. The transient length is higher for higher energy density. Figure 6.19 shows the top view and the average height profile along the scan direction for a typical single-track case. The transient length is identified based on the height. For this case, the transient length is approximately 600 µm.

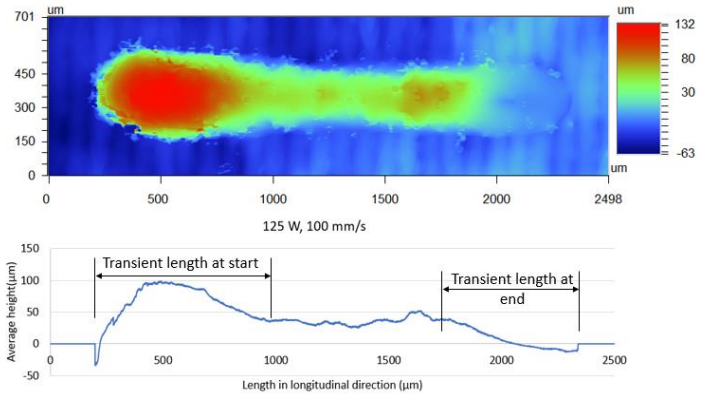

Figure 6.19 Single track transient length

During the back-and-forth multi-track scanning, the transient length observed at the start of laser and end of laser interact together. Hence, the severity of the transiency is reduced at the two ends as shown in Figure 6.20.

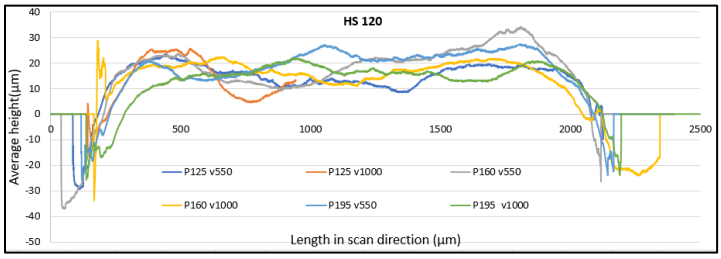

Figure 6.20 Back and forth scanning leads to similar transient region at two ends.

Transient width: The transient region formed along the transverse direction is called transient width in this study. The transient width exists as the surface height of the first track is the maximum which significantly affects the track morphology of the subsequent tracks. The transient width depends on the combination of laser power, scan speed, and hatch spacing. Figure 6.21 shows a typical case with distinct transition from the transient to quasi steady state based on the average height profile.

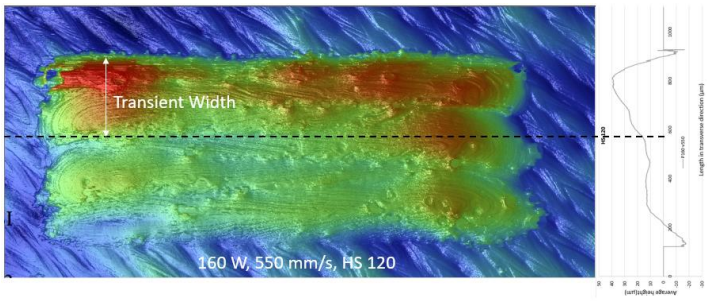

Figure 6.21 Defining the transient width based on the average height.

Figure 6.22 shows that the transient width depends on the hatch spacing. The average heigth did not show the steadiness with lower hatch spacing of 80 µm upto six tracks, which suggested that the steady state may reach at higher track number. The results indicated that the width of the multi-track region may be limited to further analyze the transient width for lower hatch spacing values. Therefore, a new experiment was designed to include multiple number of tracks for lower hatch spacings.

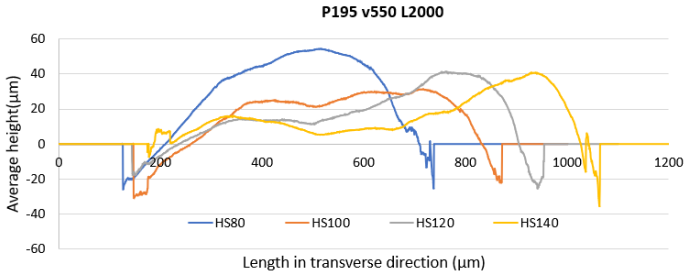

Figure 6.22 Average height profiles with different hatch spacing values.

Measuring the trasient width: An experiement was performed with a raster scan area of 4 mm * 2 mm instead of the six lines raster scan. Two levels of power 160 W and 195 W, two levels of scan speed 550 mm/s and 1000 mm/s and three levels of hatch spacing

80 µm, 100 µm and 120 µm was selected for the scans. The surface data was acquired as mentioned in the section 3. And, the data smoothing mentioned in the sub section 4.1 was used to remove the powder particles. Figure 6.23 shows one of the typical result after the removal of powder particles and the surface height variation along the width of the raster scans in the center. The transient width along the y-axis is defined as the starting positing of the track and the lowest surface height. An example of defining the trasient width is shown in Figure 6.24. The transient width of the twelve paramter combinations was calcualted. The process was repeated for two replicate sets.

Table 6.4 lists the trasient width for two replicate sets. ANOVA analysis of the data shows that the trasient width is affected by all three main parameters i.e., power, scan speeed and the hatch spacing. The main effect plot, presented in Figure 6.25, shows that higher value of power, higher value of scan speed and higher value of hatch spacing leads to the maximum trasient width.

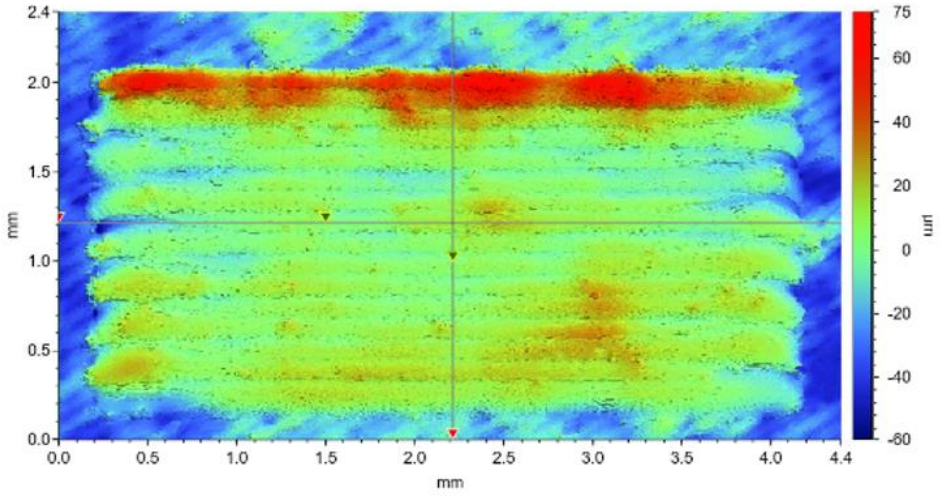

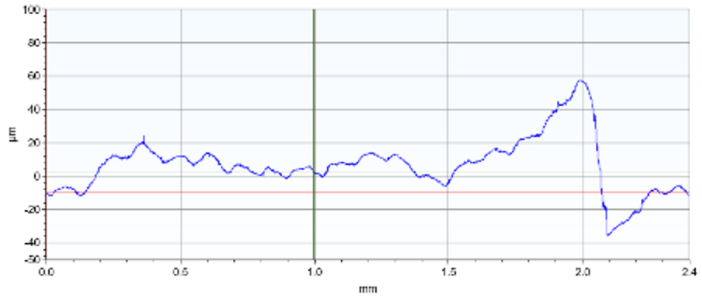

Figure 6.23 Typical result of 4 mm * 2 mm raster scan and surface height variation along the width of the raster scan

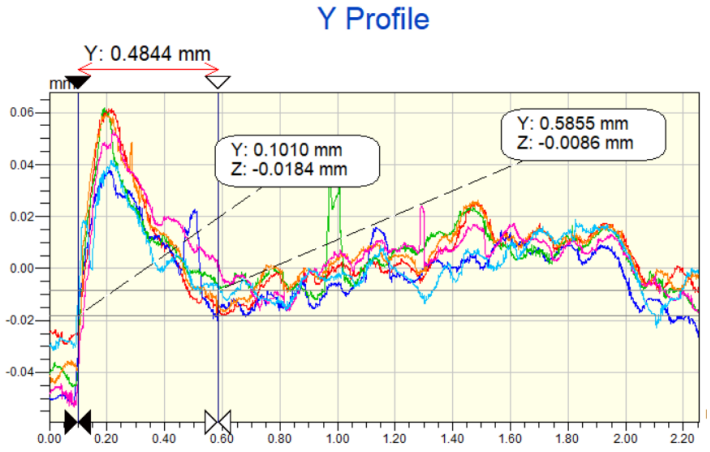

Figure 6.24 Snapshot of the surface height variation at multiple points along the y-axis

Table 6.4 Transient width for the twelve parameter combinations

Power (W)	**Scan speed (mm/s)**	**Hatch Spacing (microns)**	**Transient width (microns)**	
			Replicate 1	**Replicate 2**
160	550	80	340	364
160	1000	80	484	574
195	550	80	464	475
195	1000	80	698	615
160	550	100	371	442
160	1000	100	548	431
195	550	100	429	382
195	1000	100	773	675
160	550	120	624	594
160	1000	120	807	823
195	550	120	680	674
195	1000	120	856	777

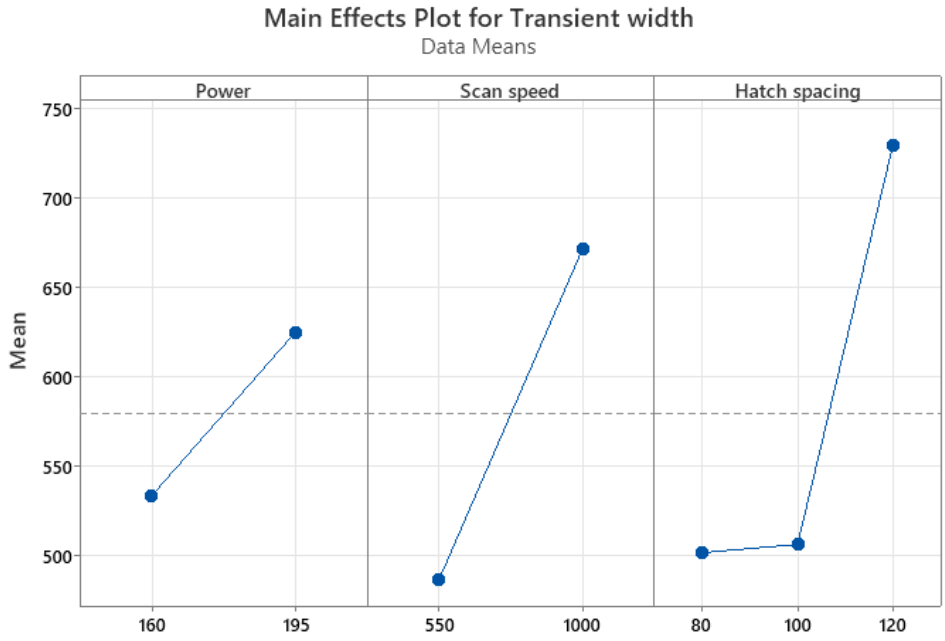

Figure 6.25 Main effect plots of power, scan speed and hatch spacing on the transient width

6.6 Conclusion

This study focuses on identifying the transient regions and investigating its influence on the surface characteristics of the multi-tracks fabricated using the LPBF process. Six back and forth tracks are fabricated using different levels of laser power (125 W, 160 W and 195 W), scan speeds (550 mm/s and 1000 mm/s), hatch spacing (80 µm, 100 µm, 120 µm, and 140 µm), and scan lengths (0.25 mm. 0.5 mm, 1 mm, and 2 mm). The surface formed with different parameters are measured using a white light interferometer and the results and analyses lead to following conclusions:

1. The geometry of the tracks on the raster scans vary along the scan direction as well as the transverse direction. The surface height can be used as a measure to distinguish the transient region and quasi steady state region.

2. The parameters that resulted in larger transient region also resulted in higher surface roughness. The shorter scan lengths which only consisted of transient zone resulted in higher surface roughness. The main effect plot showed that increasing the scan length reduced the average roughness.

3. Transient width is highly affected by the hatch spacing. The transient width could not be identified for lower hatch spacing values as the result showed the quasi-steady state may not have reached over the investigated number of tracks.

4. Large area experiment showed that the transient width is higher for the higher power of 195 W, higher scan speed of 1000 mm/s, and the higher hatch spacing value of 120 microns.

CHAPTER 7

EXPERIMENTAL STUDY OF THE EFFECTS OF PROCESS PARAMETERS ON SINGLE-LAYER RASTER SCANNING SURFACE CHARACTERISTICS IN LASER POWDER BED FUSION PROCESS

7.1 Introduction

Laser-based powder bed fusion (L-PBF) or direct metal laser sintering (DMLS), is one of the most popular types of metal additive manufacturing (AM) that employs metal powders selectively melted in a layer-wise manner by a high-intensity laser beam according to a sliced computer-aided design (CAD) model. L-PBF is widely used in various industries including medical, automotive, and aerospace. Some examples of these applications include patient-specific metal implants [111], turbine blades [112], engine manifolds [113], and lattice structures [114]. The popularity of this manufacturing technique in such industries is due to many advantages that this method offers: design freedom, reduced manufacturing time, minimized material waste, sustainability benefits, etc. [115]. However, L-PBF fabricated parts have several defects in terms of internal pores and surface roughness, which deteriorate the mechanical performance of the components.

Internal pores and defects can be reduced significantly by high-temperature heat treatments, such as hot isostatic pressing (HIP) [116], however, the effect of these

treatments on the fatigue resistance of the parts is negligible since fatigue resistance is largely determined by surface defects, which are the potential crack initiation sites, rather than internal porosities [117]. Manipulating surface roughness is also important in medical implants as the implants need to mimic human bone surface roughness to get the desired interaction between the implant and surrounding tissues. It is imperative, therefore, to be able to manipulate and control the surface roughness of the fabricated parts without requiring additional post-processing techniques. Several parameters are involved in the L-PBF process, e.g., laser beam power and speed, scanning pattern, layer thickness, metal powder size distribution, etc., the choice of which significantly affects the process stability and the quality of the parts, including their surface roughness [118,119]. Researchers have employed mechanical, chemical, and thermal-based methods to improve the surface finish of the as-built L-PBF parts [120]. Yasa et al [121] used different HF:HNO3 chemical combinations to reduce the surface roughness of Ti6Al4V samples from approximately 11 µm to around 2-4 µm. The above-mentioned research studies [122, 123] have reported that laser remelting could improve the surface quality by more than 90%, but had cautioned on the appropriate selection of the re-melting process settings. Nevertheless, surface roughness is one of the common defects inherent in the LPBF process.

Several physical phenomena may contribute to the top surface roughness of the L-PBF fabricated parts. The top surface roughness may be due to the balling effect, lack of fusion, and partially melted powder particles. The laser-material interaction in the LPBF process induces complex melt pool dynamics that occur on a short time scale and is strongly affected by both the individual parameters as well as the interplay between different parameters [122–125]. The laser power, scanning speed, and their combination,

which can be represented as the energy density, are the main parameters affecting the surface roughness in the LPBF-fabricated parts [126]. Yadroitsev et al [127] attributed the balling effect in the high scanning speed to the Plateau–Rayleigh instability, whereby the molten metal breaks into smaller droplets. Whereas the powder particles do not melt completely when there is insufficient energy. The thermal energy dissipated from the melt pool partially melts the surrounding powder particles resulting in a rougher surface [128]. In addition to the laser power and the scanning speed, the top surface roughness can be affected by the hatch spacing, as well. In the study of multi-layer samples of Hastelloy X, Tian et al [129] concluded that the smaller hatch spacing causes an increase in the surface roughness due to the attachment of the partially melted particles on the surface.

Most of the discussed research studies have improved the L-PBF process parameters and optimized the properties of bulk samples. But to further improve these properties, it is required to deeply understand the details of the fabrication and characterization of each layer during the LPBF process. One of the main contributions of this work is to investigate the correlations between surface roughness and the L-PBF process parameters for “single-layer” raster scanning samples, on which there is very limited work in the literature. Single-layer evaluation of samples is significant in layer-wise manufacturing processes, e.g., L-PBF, as the whole part is formed by adding all the single layers. This study aims to thoroughly investigate the influence of laser power, scanning speed, and hatch spacing on surface characteristics of single-layer raster scanning of Ti6Al4V samples through design of experiment. To construct a statistically reliable data set, four replicates were fabricated for each parameter set. The surface roughness data collected from the experiments are then used to train a deep learning model to successfully

predict the surface roughness of single layer raster scanning based on the input process parameters. The intent is to obtain meaningful correlations between the L-PBF process parameters and single-layer surface characteristics that can be extended to the interactions between layers of L-PBF parts fabricated with different parameter sets that can play a significant role in realizing the part quality improvement criterion when additional layers are added.

7.2 Methodology

In this study, a full factorial design of experiments (DoE) of the parameter levels presented in Table 7.1Table 7.1 was used to fabricate 1.5-mm-long single-layer raster scans. The ranges for the process parameters were selected so as to revolve around the manufacturer-recommended values for this machine/material. A full factorial DoE of three levels of the three process parameters, i.e., laser power, scanning speed, and hatch spacing, results in 27 different parameter combinations, out of which three cases were considered as failed as they resulted in no scan tracks due to insufficient energy (a combination of low laser power and high scanning speed). Four different numbers of scan tracks, i.e., 5, 10, 20, and 40 scans, are considered for each parameter combination to account for the possible transient regions formed by the few first and last scan tracks. The scan lengths for all the raster scans are 1.5 mm.

The raster scan areas are built on a single smooth layer over the surface of a semi-cylindrical base, shown in Figure 7.1. The reason for using the single smooth layer underneath the raster scans is to minimize the effects of the previous layer on the surface roughness of the top layer. The parameter set used to achieve this smooth layer was

obtained in a previous study [130] and includes a laser power of 180 W, a scanning speed of 750 mm/s, and a hatch spacing of 50 µm. A layer thickness of 30 µm was used for the fabrication of all parts and samples for this study. The semi-cylinder is built with the default EOS parameters. The schematic of a typical sample is shown in Figure 7.2. Any semi-cylinder has raster scans of four different numbers of scan lines fabricated using one parameter combination. To generate a statistically robust data set, six replicates of each process setting were fabricated and the two replicates with the largest deviations from the mean were considered outliers and excluded from further analysis, thus data from four replicates were studied for each of the parameter combinations. Materialise Magics v. 25.0 was used for STL preparation and support generation. An EOS M270 is used to fabricate the designed specimens using Ti6Al4V powders of particle size 15-45 µm from Carpenter Technology Corporation (Philadelphia, PA, USA). After the completion of the build, the specimens were separated from the build plate using a band saw.

Table 7.1 Parameters used in the design of experiments

Laser power	**Scan speed**	**Hatch Spacing**	**No. of scans**
60	500	50	5
120	1000	100	10
180	1500	150	20
			40

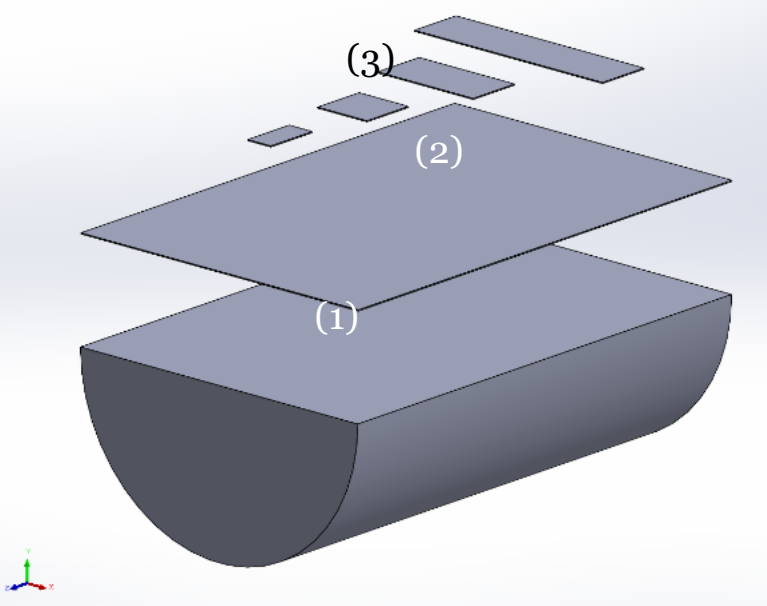

Figure 7.1 3D exploded view of a sample including (1) the semi-cylinder base, (2) the smooth single layer underneath the raster scans, and (3) the raster scanning areas with different numbers of scan lines.

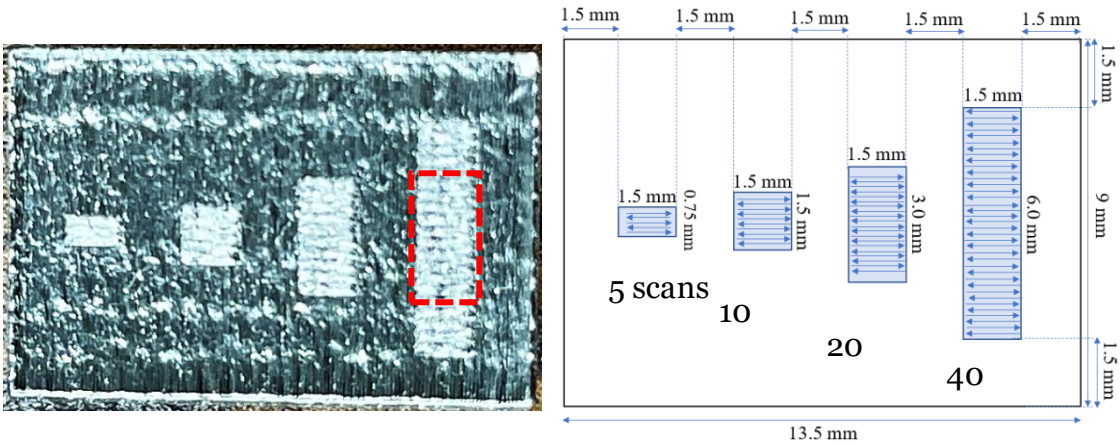

Figure 7.2 (Left) A top view of a sample, (Right) A schematic of the top view of the raster scan of the four different scan line numbers for a typical case with 150µm hatch spacing.

After removing the parts from the build plate, the surface information of the as-built raster scans is captured using a non-contact optical profiler, WYKO NT1100 from Veeco Metrology based on white light interferometry (WLI). The instrument is calibrated using a 10 µm step-height standard. Vertical scanning interferometry (VSI) measurement mode is chosen with an objective lens of 50X and a 0.5X field of view lens. This gives an effective field of view of 250 µm by 190 µm. Therefore, multiple scans were performed to capture the surface data of the raster scans in a single file. A rectangular stitching function is used to acquire the data in a single file with a back scan ranging from 100 - 250 µm for the different raster scan cases. The pixel resolution on the acquired data file is 339.5 nm in the x-direction and 396 nm in the y-direction. Figure 7.3 shows the instrument and the setup for the measurements.

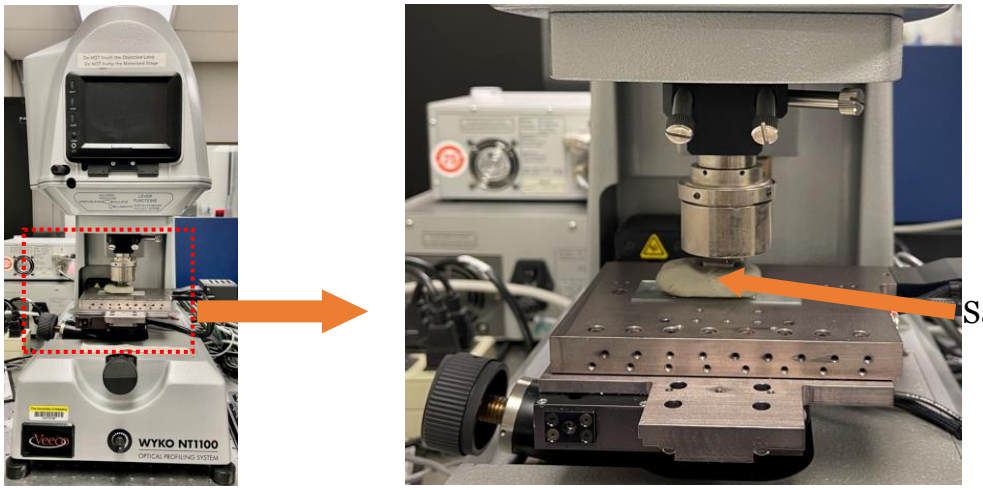

Figure 7.3 The WYKO NT1100 instrument on an air table (left), zoomed view of the scanning platform along with the sample setup (right)

The sample is placed on the clay over a slide to restrict any movement during the measurements. The acquired data is processed in the Vision software v. 3.60. To avoid the

transient regions in the start and the end lines of each scanning area, the middle 20 scan lines of the 40-scan-line region (showed by the red dashed rectangle in Figure 7.3) were selected for measurements of all the parameter sets. Detailed explanations about the selection criteria are presented in the results section.

7.3 Results

To select a reasonable area size for experimental surface characterization that can be efficient in terms of surface scanning time, and also to be a good representative of the larger surfaces manufactured by the selected process parameters, four different numbers of scan tracks i.e., 5, 10, 20, and 40 tracks were fabricated. The investigation of the surface characteristics of the tracks showed that the nature of the few tracks at the start and the end of the scanning regions were different compared to the middle region, as shown in Figure 7.4 and Figure 7.5 for two sets of parameters with different hatch spacing values. The unsteady region width at the start and end of the scanning area was different for different parameter sets. However, for all the samples, it was observed that after four to five scan tracks at the beginning of the scanning and before two to three tracks at the end, the tracks represent the quasi-steady state. Therefore, a region with 20 tracks in the middle of the 40-scan track area was selected as the best representative of the fabricated surface. The quasi-steady data was then processed and measured for the surface roughness.

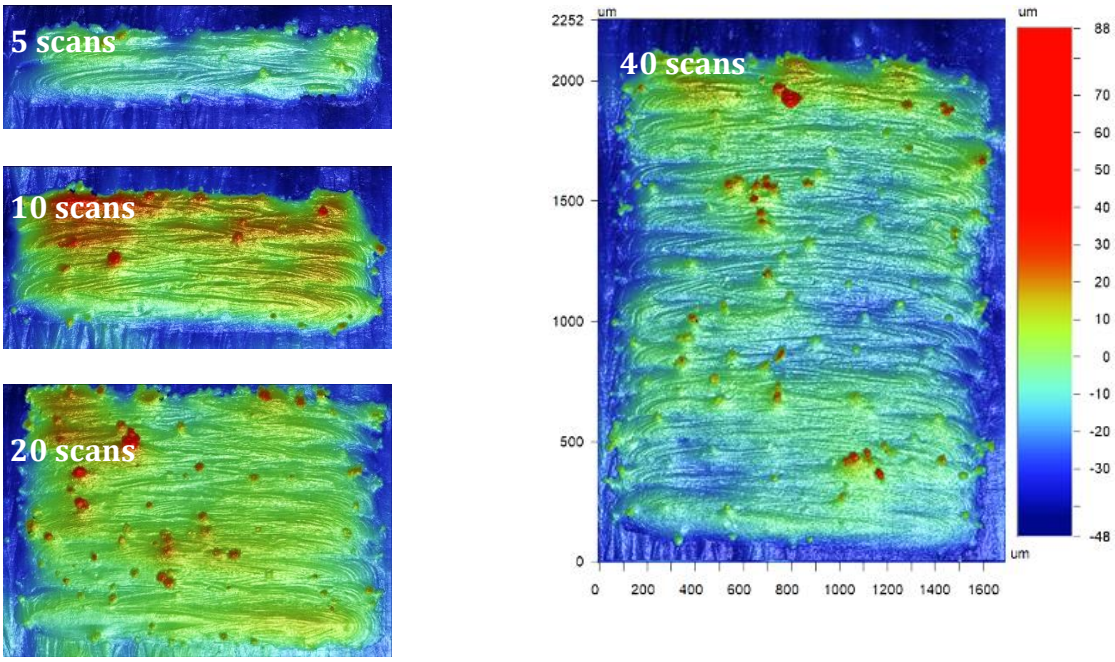

Figure 7.4 Different numbers of scan tracks fabricated with the parameter set of P = 120 W, v = 1000, and h = 50 µm.

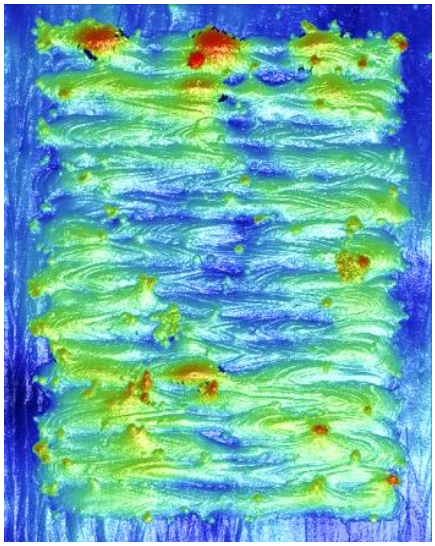

Figure 7.5 Different numbers of scan tracks fabricated with the parameter set of P = 120 W, v = 1000, and h = 100 µm.

The widths of the selected region for surface measurements were 1 mm, 2 mm, and 3 mm for hatch spacing 50 µm, 100 µm, and 150 µm, respectively. Figure 7.6 (a, b) illustrates the selected regions for surface measurements for two cases with different laser power and scanning speed values of hatch spacing of 50 µm. The unsteady regions along the scan lengths were avoided by selecting the middle 1 mm region. There is a high overlap between the subsequent tracks in the hatch spacing of 50 µm as presented in Figure 7.6 (a). The surface roughness for the selected area is calculated for the entire parameter set. This process is repeated for four replicates. Table 7.2 lists the surface roughness for four replicates obtained from the 27 unique parameter combinations of the process parameters.

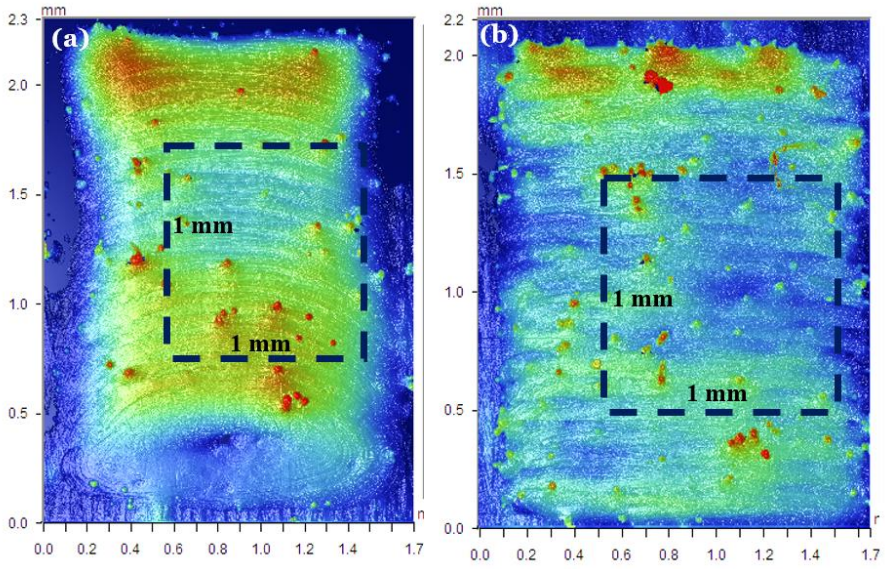

Figure 7.6 Measurement regions are shown by black dash lines to include ~ 20 scan tracks in the middle of the raster scanning of 40 scan tracks. The process parameters for these cases are as follows: (a) laser power: 180 W, speed: 500 mm/s, hatch spacing: 50 µm, (b) laser power: 120 W, speed: 1000 mm/s, hatch spacing: 50 µm.

The in-depth analysis of the raster scans showed some unique characteristics related to certain parameters. For instance, when the VED is lower than 15 J/mm^3, the raster scan area showed melted particles and some signs of the tracks, but a complete raster scan area was not formed. This was observed in three low-energy parameter sets highlighted in Table 7.2 and circled around with a red dash line in Figure 7.7. This figure shows the average surface roughness values plotted versus the volumetric energy density (VED) and follows a decreasing trend of the surface roughness with increasing the VED, similar to what is reported in the literature [130], except for the three above-mentioned cases. The surface roughness values of these cases were not considered in the analysis process.

Table 7.2 Experimental surface roughness results based on different process parameters obtained from the four replicates. The gray cases were excluded from the analysis.

Hatch	**Laser**	**Scan**	**Surface roughness (µm)**					**Energy (J/mm^3)**
			Rep. 1	Rep. 2	Rep. 3	Rep. 4	Average	
50	60	500	10.9	12.0	11.6	12.3	11.7 ±	80.0
		1000	13.6	13.5	15.2	14.7	14.3 ±	40.0
		1500	31.4	32.7	33.6	34.7	33.1 ±	26.7
	120	500	3.9	3.6	4.4	3.4	3.8 ± 0.4	80.0
		1000	6.0	6.4	5.2	4.6	5.6 ± o.8	160.0
		1500	8.0	7.1	7.5	8.6	7.8 ± 0.6	53.3
	180	500	9.1	11.2	11.5	9.9	10.4 ±	240.0
		1000	5.4	4.3	5.1	5.8	5.2 ± 0.6	120.0
		1500	4.0	3.9	6.3	5.6	5.0 ± 1.2	80.0
100	60	500	18.0	15.6	16.0	16.7	16.6 ±	40.0
		1000	29.4	29.2	28.3	28.6	28.9 ±	20.0
		1500	10.0	9.2	8.6	15.1	10.7 ±	13.3
	120	500	7.0	6.6	5.3	6.0	6.2 ± 0.7	80.0
		1000	9.2	9.6	9.5	8.9	9.3 ± 0.3	40.0
		1500	19.8	19.1	19.9	18.2	19.3 ±	26.7
	180	500	12.0	9.1	9.4	11.8	10.6 ±	120.0
		1000	8.5	7.4	11.0	8.2	8.8 ± 1.6	60.0
		1500	14.1	16.0	14.1	12.3	14.1 ±	40.0
		500	25.5	26.3	24.7	26.1	25.7 ±	26.7

150	60	1000	12.3	11.1	23.0	19.0	16.4 ±	13.3
		1500	8.5	6.4	7.9	7.7	7.6 ± 0.9	8.9
	120	500	9.2	9.9	8.7	9.6	9.4 ± 0.5	53.3
		1000	18.3	18.1	19.4	17.0	18.2 ±	26.7
		1500	25.1	24.0	24.2	27.0	25.1 ±	17.8
	180	500	12.9	14.7	11.2	11.3	12.5 ±	80.0
		1000	18.2	19.3	16.9	21.9	19.1 ±	40.0
		1500	20.8	21.1	22.4	20.5	21.2 ±	26.7

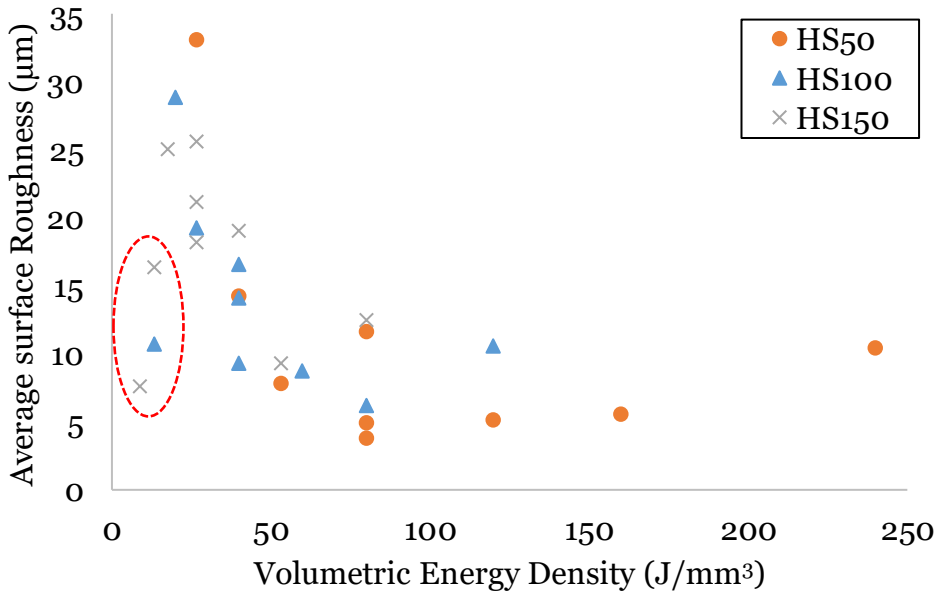

Figure 7.7 Volumetric energy density vs. average surface roughness. The three markers at the left end of the graph represent the cases without scan tracks.

ANOVA of the main factors and their interactions was conducted with a confidence interval of 95% and presented in Table 7.3. Zero p-values indicate that all three factors have significant effects on the surface roughness value. In terms of the percentage contribution, laser power is the major contributor to the surface roughness followed by hatch spacing and scanning speed. Among the three main factors, laser power has the most significant effect on surface roughness. The main effect plot, presented in Figure 7.8, shows

how the change in the individual values of the three main factors affects the surface roughness. The effect of the increase in the scanning speed and the hatch spacing has a clear upward trend in the surface roughness value. However, the surface roughness decreases sharply with the increase in the laser power from 60 W to 120 W. Then, there is a slight increase in the roughness when the laser power is increased to 180 W. Generally, increasing the laser power makes the heat energy in the melt pool contribute to melting the powder particles resulting in a smoother surface. On the other hand, it should be noted that an increase in laser power causes more spatters resulting in more powder particles attached to the raster area, as reported in the literature [131]. Therefore, the surface roughness slightly increases in the raster scans with a higher laser power, which in this case is 180 W. Apart from the powder spattering, the surface height variation range decreases from 99 µm in the 60 W case to 64 µm in 120 W and then follows by an increase to 122 µm in the 180 W case. The surface height variation range can be calculated by subtracting the maximum and minimum values of surface features provided by the scale bars in Figure 7.9. This might be due to the higher bead height in cases with high energy densities [132]. Overall, based on the obtained results, it can be concluded that using the laser power of 120 W, the scanning speed of 500 mm/s, and the hatch spacing of 50 µm results in the smoothest surface that can be obtained by using these parameter levels. This minimum value turned out to be 3.8 ± 0.4 µm in the performed experiments in this study, shown in Table 7.3.

Furthermore, the grouping in the Tukey test presented in Table 7.4 explains the response of the individual values of the factors. The letters A, B, and C indicate the order of significance of the mean effect of the individual parameter values on the surface roughness. The laser power values of 180 W and 120 W sharing similar means are grouped

with the letter B, in contrast to the 60 W. The means of the three values of scanning speed and hatch spacing are independent of each other. They are grouped into three categories with the letters A, B, and C.

Table 7.3 ANOVA analysis for the main factors

Source	DF	Adj SS	Adj	F-	P-	Contribution
Laser power(W)	2	2991.14	1495.57	93.25	0.000	48.3
Scan speed	2	1331.53	665.76	41.51	0.000	21.5
Hatch spacing	2	1867.3	933.65	58.21	0.000	30.2
Error	89	1427.41	16.04			
Lack-of-Fit	17	1341.03	78.88	65.75	0.000	
Pure Error	72	86.38	1.2			
Total	95	6117.33				100.0

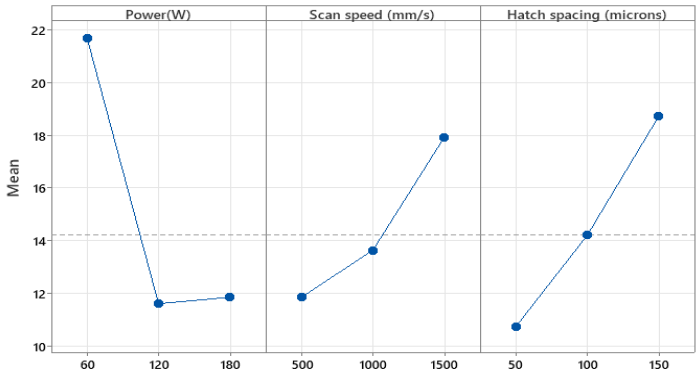

Figure 7.8 Main effect plot for the surface roughness (µm)

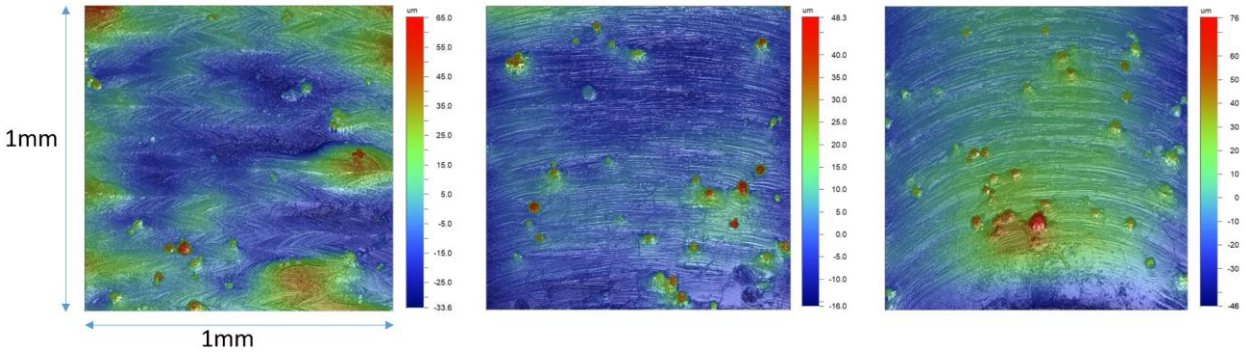

Figure 7.9 1 mm by 1 mm raster scanning areas with the same scanning speed (500 mm/s) and hatch spacing (50 μm), but three different laser power values of 60 W, 120 W, and 180 W, respectively from the left to right.

Table 7.4 Tukey Pairwise Comparisons between process parameter levels. The means that do not share a grouping letter are significantly different.

Laser power (W)	N	Mean	Grouping
60	24	31.5464	A
180	36	11.8619	B
120	36	11.6203	B
Scan speed (mm/s)	N	Mean	Grouping
1500	28	26.4441	A
1000	32	16.7217	B
500	36	11.8628	C
Hatch spacing (μm)	N	Mean	Grouping
150	28	26.0198	A
100	32	18.2616	B
50	36	10.7472	C

In the ANOVA analysis of the main factors and their interactions presented in Table 7.5, the two-way interactions of laser power-scanning speed and laser power-hatch spacing have the most and least effects, respectively, on the surface roughness. The interaction plot

(Figure 7.10) shows the response of the two-way interaction of different values on the surface roughness. For lower laser power of 60 W, the increase in the scanning speed to 1500 mm/s causes a significant increase in the surface roughness. However, at a scanning speed of 1000 mm/s, both laser power values of 120 W and 180 W result in similar surface roughness. The difference in the roughness is minimum for all three hatch spacing cases for laser power values of 120 W and 180 W. This is incongruent with the same grouping of 120 W and 180 W in the Tukey test in Table 7.4. Also, the top-left grid of Figure 7.10, shows unparallel lines for the laser power-scan speed interaction, indicating a dependence between these two parameters. This interaction is also reflected in the highest contribution (11.3%) among all the parameter interactions in the last column of Table 7.5.

Table 7.5 ANOVA analysis for the main factors and their two-way interactions

Source	DF	Adj SS	Adj MS	F-Value	P-	Contribution
Power (W)	2	3424.33	1712.16	981.61	0.000	34.9
Speed (mm/s)	2	2111.99	1056	605.42	0.000	21.5
Hatch (µm)	2	2404.37	1202.18	689.23	0.000	24.5
Power (W) * Speed	4	1107.72	276.93	158.77	0.000	11.3
Power (W) * Hatch	4	273.29	68.32	39.17	0.000	2.8
Speed (mm/s) * Hatch	4	481.66	120.41	69.04	0.000	4.9
Error	77	134.31	1.74			
Lack-of-Fit	5	47.93	9.59	7.99	0.000	
Pure Error	72	86.38	1.2			
Total	95	6117.33				100.0

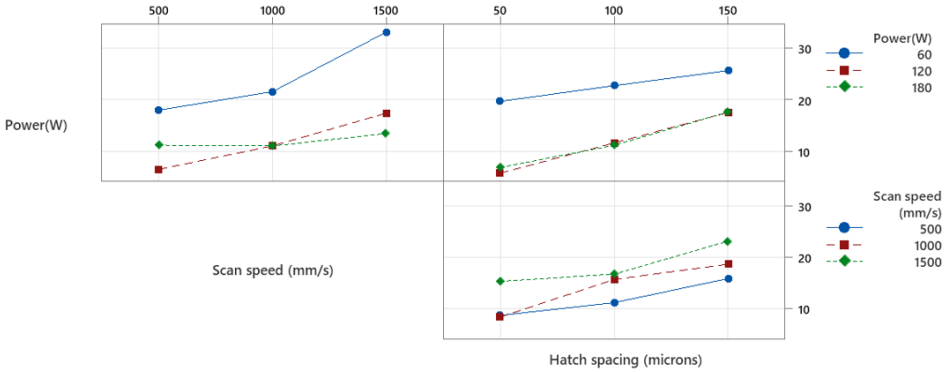

Figure 7.10 Two-way interaction plots for average surface roughness (µm)

7.4 Conclusions

The influences of the L-PBF process parameters, including laser power, scanning speed, and hatch spacing, on the surface characteristics of "single-layer" raster scanning of Ti6Al4V samples were thoroughly investigated through design of experiment and multiple replicates. The experimental data from quasi-steady regions of the samples was acquired by white-light interferometry (WLI). One of the challenges encountered during the study was the selection of a reasonable area (size- and location-wise) for surface characterization of raster scans. Below are the major findings:

- Higher surface roughness was observed on raster scan areas with lower laser power, higher scanning speed, and higher hatch spacing, which result in lower volumetric energy density (VED).
- Raster scan areas with a VED lower than 15 J/mm^3 only showed some partially melted powder particles and lacked the formation of complete scan tracks.

- Among the three main parameters, laser power played the most significant role in determining the surface roughness value.
- With constant scanning speed and hatch spacing, surface roughness decreased sharply with the increase in laser power from 60 W to 120 W, which was consistent with its decrease with the VED increment. However, it slightly increased when the laser power was further increased to 180 W. The further increment of the laser power was attributed to delivering excess thermal energy to the melt pool resulting in higher powder spattering and more convex scan tracks and thus higher surface roughness.
- At high scanning speeds, balling effect resulted in higher surface roughness values.
- At lower hatch spacing, a larger overlap between the subsequent tracks decreased the surface roughness.

CHAPTER 8

CONCLUSION AND FUTURE WORK

8.1 Conclusion

This dissertation presents a detailed study of the melt pool dynamics, exploring its behavior across a wide range of process parameters independently as well as multiple process parameter combination. The melt pool geometry is studied at different length scales using one and two dimensional samples printed using the L-PBF process. The printed samples are also analyzed for the porosity and their surface characteristics. The conclusion of this dissertation are:

The quality of parts produced in the powder bed fusion process is significantly influenced by the properties of the powder particles. The distribution of the particle sizes in the powder bed affects the evolution and progression of melt pool during the laser to material interaction. A powder bed containing smaller diameter particles promoted a continuous and smoother flow during the melting and the fusion process. The developed model incorporated with temperature dependent parameters, surface tension gradient, and volume of fluid flow can be applied to predict the effect of key process parameters including the scan speed, power, and laser absorptivity on the melt pool dimensions. The model was successfully applied for quantitative analysis of the track width for various scan speed at a constant power.

The presence of keyhole pores in parts fabricated using the L-PBF process can significantly impact the mechanical properties of the printed components. The level of porosity in the parts tends to increase with higher energy density during the printing process. Among all the samples, the one built vertically at location A, with a power setting of 150 W and a velocity of 600 mm/s, displayed the highest porosity of 0.52 percent. Despite similar porosity levels to the samples built at an angle, the vertically built sample demonstrated higher ultimate tensile strength. Upon analyzing the fractured samples, it was observed that not only the pores surrounding the fractured region increased in volume, but the pores throughout the entire sample also increased in volume.

Single tracks are the unidirectional individual paths created by the laser scans as it melts the powder particles to build up on a single layer. There exists a region at the start and at the end of the single tracks which have different surface height and track width compared to the middle region of the scan. The region in the middle was referred as the quasi-steady region and the regions in the start and the middle were defined as the transient region. Depending on the length of the single tracks, they may or may not achieve a quasi-steady state. For the Ti-6Al-4V powder material, it was observed that the transient length at the start will vary depending on the power and scan speed used to deposit the single tracks. Single tracks with lengths of 0.25mm, 0.5 mm, 1 mm, and 2 mm were printed and analyzed. The maximum transient length was 1424 microns, for a power of 195 W and a scan speed of 100 mm/s. Conversely, the minimum transient length observed was 315 microns, for a power of 80 W and a scan speed of 400 mm/s. The increase in power causes an increase in transient length given that other parameters remain unchanged. The

relationship is inverse for a constant power i.e., the increase in speed results in a decrease in transient length given that other parameters remain unchanged.

The raster scans were printed by tracing a series of parallel lines by moving the laser in alternate direction along the X-axis. Six back-and-forth tracks were created, involving three levels of laser power (125 W, 160 W, and 195 W), two levels of scan speeds (550 mm/s and 1000 mm/s), four levels of hatch spacing (80 µm, 100 µm, 120 µm, and 140 µm), and four levels of scan lengths (0.25 mm, 0.5 mm, 1 mm, and 2 mm). The transient zone exist in both x- and y-direction within the raster scans. The surface height was used as a measure to distinguish the transient region from the quasi steady state region. Raster scans with shorter scan lengths, which did not reach the quasi-steady state and only consisted of the transient zone, led to higher surface roughness. The transient width was not clearly distinguishable for lower hatch spacing values as the result showed the quasi-steady state may not have reached over the investigated six number of tracks. The analysis of a new large area experiment, comprising multiple number of tracks, revealed that the transient width increased with higher power of 195 W, higher scan speed of 1000 mm/s, and hatch spacing values of 120 microns.

An experiment was designed to investigate the surface characteristics of the raster scans. During data analysis, only the quasi-steady state region was taken into account, deliberately excluding the transient region in both the x- and y-directions. Raster scan regions with lower laser power, higher scanning speed, and increased hatch spacing exhibited higher surface roughness. Among the three primary parameters, laser power exerted the most substantial influence on determining the surface roughness. While

maintaining constant scanning speed and hatch spacing, a significant reduction in surface roughness was observed with the increment in laser power from 60 W to 120 W. There was a slight increase in surface roughness when the laser power was further raised to 180 W. This increase was attributed to an excessive delivery of thermal energy to the melt pool, leading to more powder spattering, formation of more convex scan tracks, and ultimately resulting in higher surface roughness.

8.2 Future work

This dissertation includes detailed study of the melt pool geometry and its variations using a combination of experimental and computational methods. It investigates the melt pool dynamics with various parameter combinations and at different length scales. The findings obtained from these studies can be used as a basis for exploring new research topics.

The results obtained from the Fluent simulations demonstrate the significance of powder particle size and particle size distribution in influencing the melt pool evolution during the L-PBF process. This model assumed perfectly spherical powder particles and included a simplified recoater design, which may not fully capture the complexities present in actual experimental conditions. Parameters such as particle flowability and particle bed packing density can also impact the powder bed distribution. Future studies could delve deeper into the impacts of these parameters and interaction between different designs of recoater blades with the powder particles.

The CT scan results confirm the expansion of pores present throughout the gage region in the fractured samples with the application of tensile force on the as-built samples. A prospective study can explore if there is a potential correlation between pore distribution along the samples and the location of failure. Such a study could analyze the fractured surfaces to understand the mechanism and contribution of the pores in the failure and compare the fractographic features of materials with varying porosity levels to determine the relationship between porosity percentage and fracture behavior.

In the future, this study conducted on transient region in metal additive manufacturing processes can be extended to include other materials. By comparing the transient lengths of different materials, the study can identify patterns, trends, and variations that may exist. Such study may pave the way for formulating general equations that can estimate the transient length under a range of process conditions for different materials. It can be extended to include two and three-dimensional analyses of the transient region with a new powder material. The results from new material will help to assess whether the findings obtained from the Ti64 powder material remain consistent when applied to the new material.

The high fidelity computational setup in Flow 3D was capable of predicting the melt pool dynamics in the powder bed fusion process for various process parameter conditions. The model does not replicate the movement of the powder particles as observed in the experimental conditions. The future modeling techniques should leverage coupled modeling techniques to include the powder particle movement in the thermo-fluid simulation. Through the implementation of a coupled modeling approach that considers

the interactions between the laser, gas flow, and powder particles, the computational model will represent more realistic scenario of the powder bed fusion process.

REFERENCES

[1] Li, C., Fu, C., Guo, Y., and Fang, F., 2016, "A multiscale modeling approach for fast prediction of part distortion in selective laser melting," Journal of Materials Processing Technology, 229, pp. 703-712.

[2] Thijs, L., Verhaeghe, F., Craeghs, T., Van Humbeeck, J., and Kruth, J.-P., 2010, "A study of the microstructural evolution during selective laser melting of Ti–6Al–4V," Acta Materialia, 58(9), pp. 3303-3312.

[3] http://www.arcam.com/technology/electron-beam-melting/.

[4] Konda Gokuldoss, P., Kolla, S., & Eckert, J. Additive Manufacturing Processes: Selective Laser Melting, Electron Beam Melting and Binder Jetting—Selection Guidelines

[5] Mukherjee, Tuhin & Zhang, W & Debroy, Tarasankar. (2017). "An improved prediction of residual stresses and distortion in additive manufacturing". Computational Materials Science.

[6] Cheng-JuiLiabTsung-WenTsaibChien-ChouTsenga, "Numerical Simulation for Heat and Mass Transfer During Selective Laser Melting of Titanium alloys Powder", Physics Procedia,Volume 83, 2016, Pages 1444-1449.

[7] Hussein, A., Hao, L., Yan, C., and Everson, R., 2013, "Finite element simulation of the temperature and stress fields in single layers built without-support in selective laser melting," Materials & Design, 52, pp. 638-647.

[8] Patil N, Pal D, Khalid Rafi HH, et al. A Generalized Feed Forward Dynamic Adaptive Mesh Refinement and Derefinement Finite Element Framework for Metal Laser Sintering—Part I: Formulation and Algorithm Development. ASME. J. Manuf. Sci. Eng. 2015;137(4):041001-041001-15.

[9] Spears, Thomas G. and Gold, Scott A., In-process sensing in selective laser melting (L-PBF) additive manufacturing

[10] Spierings, Adriaan & Herres, Nikolaus & Levy, G. (2011). Influence of the particle size distribution on surface quality and mechanical properties in AM steel parts. Rapid Prototyping Journal - RAPID PROTOTYPING J. 17. 195-202. 10.1108/13552541111124770.3

[11] Turker, M., Godlinski, D., and Petzoldt, F., 2008, "Effect of production parameters on the properties of IN 718 superalloy by three-dimensional printing," Materials characterization, 59(12), pp. 1728-1735.

[12] Zhang, Q.-L., Yao, J.-H., and Mazumder, J., 2011, "Laser direct metal deposition technology and microstructure and composition segregation of Inconel 718 superalloy," Journal of Iron and Steel Research, International, 18(4), pp. 73-78.

[13] Song, B., Dong, S., Zhang, B., Liao, H., and Coddet, C., 2012, "Effects of processing parameters on microstructure and mechanical property of selective laser melted Ti6Al4V," Materials & Design, 35, pp. 120-125.

[14] Wang, Z., Guan, K., Gao, M., Li, X., Chen, X., and Zeng, X., 2012, "The microstructure and mechanical properties of deposited-IN718 by selective laser melting," Journal of Alloys and Compounds, 513, pp. 518-523.

[15] Strondl, A., Lyckfeldt, O., Brodin, H., and Ackelid, U., 2015, "Characterization and control of powder properties for additive manufacturing," JOM, 67(3), pp. 549-554.

[16] Roland Berger, April 2016, Additive Manufacturing next generation

[17] Zhengdong Liu, 2017, Economic Comparison of Selective Laser Melting and Conventional Subtractive Manufacturing Processes

[18] Nesma T. Aboulkhair , Nicola M. Everitt, Ian Ashcroft, Chris Tuck, 2014, “Reducing porosity in AlSi10Mg parts processed by selective laser melting”, Journal of Additive Manufacturing 1-4, pp 77–86

[19] S. Das “Physical aspects of process control in selective laser sintering of metals” Adv. Eng. Mater., 5 (2003), pp. 701-711

[20] Reutzel, E. W., and Nassar, A. R., 2015, "A survey of sensing and control systems for machine and process monitoring of directed-energy, metal-based additive manufacturing," Rapid Prototyping Journal, 21(2), pp. 159-167.

[21] Clijsters, S., Craeghs, T., Buls, S., Kempen, K., and Kruth, J.-P., 2014, "In situ quality control of the selective laser melting process using a high-speed, real-time melt pool monitoring system," The International Journal of Advanced Manufacturing Technology, 75(5-8), pp. 1089-1101.

[22] Craeghs, T., Bechmann, F., Berumen, S., and Kruth, J.-P., 2010, "Feedback control of Layerwise Laser Melting using optical sensors," Physics Procedia, 5, pp. 505-514.

[23] Saad A. Khairallah, Andy Anderson, “Mesoscopic simulation model of selective laser melting of stainless steel powder”, In Journal of Materials Processing Technology, Volume 214, Issue 11, 2014,

[24] Jay Dunbar,” Analysis Of The Laser Powder Bed Fusion Additive Manufacturing Process Through Experimental Measurement And Finite Element Modeling”, A Dissertation in Mechanical Engineering, 2016, The Pennsylvania State University

[25] Song, B., Dong, S., Zhang, B., Liao, H., and Coddet, C., 2012, "Effects of processing parameters on microstructure and mechanical property of selective laser melted Ti6Al4V," Materials & Design, 35, pp. 120-125.

[26] C. Y. Yap, 2015, “Review of selective laser melting: Materials and applications”, Applied Physics Reviews

[27] Kaaufui V. Wong et al., 2012, “A Review of Additive Manufacturing”, International Scholarly Research Network

[28] E.O. Olakanmi, et al., 2015, “A review on selective laser sintering/melting (SLS/L-PBF) of aluminium alloy powders: Processing, microstructure, and properties”, Progress in Materials Science

[29] Bias CT. In, “Hybrid laser-arc welding”, 2009, Woodhead Publishing Ltd

[30] Campbell J., 1991, “Complete casting handbook: metal casting processes”, metallurgy, techniques and design

[31] S. Das, 2003, “Physical Aspects of Process Control in Selective Laser Sintering of Metals”

[32]Amato, K., Gaytan, S., Murr, L., Martinez, E., Shindo, P., Hernandez, J., Collins, S., and Medina, F., 2012, "Microstructures and mechanical behavior of Inconel 718 fabricated by selective laser melting," Acta Materialia, 60(5), pp. 2229-2239

[33] Shifeng, W., Shuai, L., Qingsong, W., Yan, C., Sheng, Z., and Yusheng, S., 2014, "Effect of molten pool boundaries on the mechanical properties of selective laser melting parts," Journal of Materials Processing Technology, 214(11), pp. 2660-2667.

[34] Vrancken, B., Thijs, L., Kruth, J.-P., and Van Humbeeck, J., 2012, "Heat treatment of Ti6Al4V produced by selective laser melting: microstructure and mechanical properties," Journal of Alloys and Compounds, 541, pp. 177-185

[35] Thomas, D. S., and Gilbert, S. W., 2014, "Costs and Cost Effectiveness of Additive Manufacturing."

[36] Sames, W. J., List, F. A., Pannala, S., Dehoff, R. R., and Babu, S. S., 2016, "The metallurgy and processing science of metal additive manufacturing," International Materials Reviews, 61(5), pp. 315-360.

[37] Kruth, J. P., Levy, G., Klocke, F., and Childs, T. H. C., 2007, "Consolidation phenomena in laser and powder-bed based layered manufacturing," CIRP Annals - Manufacturing Technology, 56(2), pp. 730-759.

[38] Kou, S., and Wang, Y. H., 1986, "Three-dimensional convection in laser melted pools," Metallurgical Transactions A, 17(12), pp. 2265-2270.

[39] Lee, Z., 2015, "Mesoscopic Simulation of Heat Transfer and Fluid Flow in Laser Powder Bed Additive Manufacturing.pdf," (Proceedings of the Solid Freeform Fabrication Symposium, Austin, TX, 1154-1165).

[40] Yuan, P., and Gu, D., 2015, "Molten pool behaviour and its physical mechanism during selective laser melting of TiC/AlSi10Mg nanocomposites: simulation and experiments," Journal of Physics D: Applied Physics, 48(3).

[41] Khairallah, S. A., Anderson, A. T., Rubenchik, A., and King, W. E., 2016, "Laser powder-bed fusion additive manufacturing: Physics of complex melt flow and formation mechanisms of pores, spatter, and denudation zones," Acta Materialia, 108, pp. 36-45.

[42] Lee, W.-H., Zhang, Y., and Zhang, J., 2017, "Discrete element modeling of powder flow and laser heating in direct metal laser sintering process," Powder Technology, 315, pp. 300-308.

[43] Liu B, W. R., Tuck C, Ashcroft I, Hague R, 2011, "Investigation the effect of particle size distribution on processing parameters optimisation in selective laser melting process " (Proceedings of the Solid Freeform Fabrication Symposium, Austin, TX, 227-238).

[44] Spierings AB, L. G., 2009, "Comparison of density of stainless steel 316L parts produced with selective laser melting using different powder grades.," (Proceedings of the Solid Freeform Fabrication Symposium, Austin, TX, 342-353.).

[45] Panwisawas, C., Perumal, B., Ward, R. M., Turner, N., Turner, R. P., Brooks, J. W., and Basoalto, H. C., 2017, "Keyhole formation and thermal fluid flow-induced porosity during laser fusion welding in titanium alloys: Experimental and modelling," Acta Materialia, 126, pp. 251-263.

[46] "APC Brochure Montage," http://advancedpowders.com/wp-content/uploads/APC_Brochure_Montage.pdf(2018),

[47] Mills, K. C., 2002, "Recommended values of thermophysical properties for selected commercial alloy," Aircraft Engineering and Aerospace Technology, 74(5),

[48] Boivineau, M., Cagran, C., Doytier, D., Eyraud, V., Nadal, M.-H., Wilthan, B., and Pottlacher, G., 2006, "Thermophysical Properties of Solid and Liquid Ti-6Al-4V (TA6V) Alloy," International Journal of Thermophysics, 27(2), pp. 507-529.

[49] Kobayashi, M., Otsuki, M., Sakate, H., Sakuma, F., and Ono, A., 1999, "System for Measuring the Spectral Distribution of Normal Emissivity of Metals with Direct Current Heating," International Journal of Thermophysics, 20(1), pp. 289-298.

[50] Shrestha, S., Rauniyar, S., and Chou, K., 2018, "Thermo-Fluid Modeling of Selective Laser Melting: Single-Track Formation Incorporating Metallic Powder," Journal of Materials Engineering and Performance.

[51] Slotwinski, J. A., Garboczi, E. J. & Hebenstreit, K. M. Porosity Measurements and Analysis for Metal Additive Manufacturing Process Control. 119, (2014). DOI: 10.6028/jres.119.019

[52] Dilip, J. J. S. *et al.* Influence of processing parameters on the evolution of melt pool, porosity, and microstructures in Ti-6Al-4V alloy parts fabricated by selective laser melting. *Prog. Addit. Manuf.* 2, 157–167 (2017).

[53] Kasperovich, G., Haubrich, J., Gussone, J. & Requena, G. Correlation between porosity and processing parameters in TiAl6V4 produced by selective laser melting. *Materials and Design* 105, 160–170 (2016).

[54] S.R Stock, N.K Naik, A.P Wilkinson, K.E Kurtis, X-ray microtomography (microCT) of the progression of sulfate attack of cement paste, Cement and Concrete Research, Volume 32, Issue 10, 1673-1675, (2002)

[55] Maire, E. & Withers, P. J. Quantitative X-ray tomography. *Int. Mater. Rev.* 59, 1–43 (2013). Thompson, A., Maskery, I. & Leach, R. K. X-ray computed tomography for additive manufacturing: A review. Meas. Sci. Technol. 27, (2016).

[56] Thompson, A., Maskery, I. & Leach, R. K. X-ray computed tomography for additive manufacturing: A review. *Meas. Sci. Technol.* 27, (2016).

[57] S. Leuders, M. Thöne, A. Riemer, T. Niendorf, T. Tröster, H.A. Richard, H.J. Maier, On the mechanical behaviour of titanium alloy TiAl6V4 manufactured by selective laser melting: Fatigue resistance and crack growth performance, International Journal of Fatigue, 300-307, (2013)

[58] Spierings, A. B., Schneider, M. & Eggenberger, R. Comparison of density measurement techniques for additive manufactured metallic parts. *Rapid Prototyp. J.* 17, 380–386 (2011).

[59] Wits, W. W., Carmignato, S., Zanini, F. & Vaneker, T. H. J. Porosity testing methods for the quality assessment of selective laser melted parts. *CIRP Annals - Manufacturing Technology* 65, 201–204 (2016).

[60] Siddique, S. *et al.* Computed tomography for characterization of fatigue performance of selective laser melted parts. *Materials and Design* 83, 661–669 (2015).

[61] Maskery, I. *et al.* Quantification and characterisation of porosity in selectively laser melted Al-Si10-Mg using X-ray computed tomography. *Materials Characterization* 111, 193–204 (2016).

[62] du Plessis, A. & le Roux, S. G. Standardized X-ray tomography testing of additively manufactured parts: A round robin test. *Additive Manufacturing* 24, 125–136 (2018).

[63] Gong, H. *et al.* Influence of defects on mechanical properties of Ti-6Al-4V components produced by selective laser melting and electron beam melting. *Materials and Design* 86, 545–554 (2015).

[64] Cunningham, R., Narra, S. P., Montgomery, C., Beuth, J. & Rollett, A. D. Synchrotron-Based X-ray Microtomography Characterization of the Effect of Processing Variables on Porosity Formation in Laser Power-Bed Additive Manufacturing of Ti-6Al-4V. *JOM* 69, 479–484 (2017).

[65] Shrestha, S., Starr, T., and Chou, K., 2019, "A Study of Keyhole Porosity in Selective Laser Melting: Single-Track Scanning with Micro-CT Analysis," J. Manuf. Sci. Eng. Trans. ASME, 141(7).

[66] Martin, A. A. *et al.* Dynamics of pore formation during laser powder bed fusion additive manufacturing. *Nature Communications.* 10, 1–10 (2019).

[67] ASTM E8/E8M-11, Standard Test Method for Tension Testing of Metallic Materials. ASTM International, West Conshohocken, PA, 2013.

[68] Zhang, S., Rauniyar, S., Shrestha, S., Ward, A. & Chou, K. An experimental study of tensile property variability in selective laser melting. *Journal of Manufacturing Processes* (2019). DOI: 10.1016/j.jmapro.2019.03.045

[69] Gong, H., Rafi, K., Gu, H., Starr, T., & Stucker, B. (2014). Analysis of defect generation in Ti-6Al-4V parts made using powder bed fusion additive manufacturing processes. In Additive Manufacturing (Vol. 1, pp. 87–98). https://doi.org/10.1016/j.addma.2014.08.002

[70] Schmidt, M., Merklein, M., Bourell, D., Dimitrov, D., Hausotte, T., Wegener, K., Overmeyer, L., Vollertsen, F., and Levy, G. N., 2017, "Laser Based Additive Manufacturing in Industry and Academia," CIRP Ann., 66(2), pp. 561–583.

[71] du Plessis, A., Yadroitsava, I., and Yadroitsev, I., 2018, "Ti6Al4V Lightweight Lattice Structures Manufactured by Laser Powder Bed Fusion for Load-Bearing Applications," Opt. Laser Technol., 108, pp. 521–528.

[72] Lin, K., Yuan, L., and Gu, D., 2019, "Influence of Laser Parameters and Complex Structural Features on the Bio-Inspired Complex Thin-Wall Structures Fabricated by Selective Laser Melting," J. Mater. Process. Technol., 267(November 2018), pp. 34–43.

[73] Calignano, F., Cattano, G., and Manfredi, D., 2018, "Manufacturing of Thin Wall Structures in AlSi10Mg Alloy by Laser Powder Bed Fusion through Process Parameters," J. Mater. Process. Technol., 255(February), pp. 773–783.

[74] Saltzman, D., Bichnevicius, M., Lynch, S., Simpson, T. W., Reutzel, E. W., Dickman, C., and Martukanitz, R., 2018, "Design and Evaluation of an Additively Manufactured Aircraft Heat Exchanger," Appl. Therm. Eng., 138(November 2017), pp. 254–263.

[75] Yang, L., Gong, H., Dilip, S., and Stucker, B., 2014, "An Investigation of Thin Feature Generation in Direct Metal Laser Sintering Systems," Proc. 26th Annu. Int. Solid Free. Fabr. Symp., pp. 714–731.

[76] Bidare, P., Bitharas, I., Ward, R. M., Attallah, M. M., and Moore, A. J., 2018, "Fluid and Particle Dynamics in Laser Powder Bed Fusion," Acta Mater., 142, pp. 107–120.

[77] Matthews, M. J., Guss, G., Khairallah, S. A., Rubenchik, A. M., Depond, P. J., and King, W. E., 2017, "Denudation of Metal Powder Layers in Laser Powder-Bed Fusion Processes," Addit. Manuf. Hand b. Prod. Dev. Def. Ind., 114, pp. 677–693.

[78] Anam, A., Dilip, J. J. S., Pal, D., and Stucker, B., 2014, "Effect of Scan Pattern on the Microstructural Evolution of Inconel 625 during Selective Laser Melting," Int. Solid Free. Fabr. Symp. – An Addit. Manuf. Conf., pp. 363–376.

[79] Scipioni Bertoli, U., Wolfer, A. J., Matthews, M. J., Delplanque, J. P. R., and Schoenung, J. M., 2017, On the Limitations of Volumetric Energy Density as a Design Parameter for Selective Laser Melting," Mater. Des., 113, pp. 331–340.

[80] Martin, A. A., Calta, N. P., Khairallah, S. A., Wang, J., Depond, P. J., Fong, A. Y., Thampy, V., Guss, G. M., Kiss, A. M., Stone, K. H., Tassone, C. J., Nelson Weker, J., Toney, M. F., van Buuren, T., and Matthews, M. J., 2019, "Dynamics of Pore Formation during Laser Powder Bed Fusion Additive Manufacturing," Nat. Commun., 10(1), pp. 1–10.

[81] Birnbaum, A., Aggarangsi, P., and Beuth, J., 2003, “Process Scaling and Transient Melt Pool Size Control in Laser-Based Additive Manufacturing Processes,” Proc. 14th Solid Free. Fabr. Symp., pp. 328–339.

[82] Aggarangsi, P., Beuth, J. L., and Gill, D. D., 2004, “Transient Changes in Melt Pool Size in Laser Additive Manufacturing Processes,” Proc. 15th Solid Free. Fabr. Symp., pp. 163–174.

[83] Soylemez, E., Beuth, J. L., and Taminger, K., 2010, “Controlling Melt Pool Dimensions over a Wide Range of Material Deposition Rates in Electron Beam Additive Manufacturing,” 21st Annu. Int. Solid Free. Fabr. Symp. - An Addit. Manuf. Conf. SFF 2010, (January 2010), pp. 571–582.

[84] Fox, J., and Beuth, J., 2013, “Process Mapping of Transient Melt Pool Response in Wire Feed E-Beam Additive Manufacturing of Ti-6Al-4V,” 24th Int. SFF Symp. - An Addit. Manuf. Conf. SFF 2013, pp. 675–683.

[85] Cheng, B., and Chou, K., 2015, “Melt pool evolution study in selective laser melting,” 26th Annu. Int. Solid Free. Fabr. Symp. - An Addit. Manuf. Conf. SFF 2015, August 10–12 (2015), pp. 1182-1194

[86] Obidigbo, C. N., 2017, “A Numerical and Experimental Investigation of Steady-State and Transient Melt Pool Dimensions in Additive Manufacturing of Invar 36.”

[87] Vilardell, A. M., Takezawa, A., du Plessis, A., Takata, N., Krakhmalev, P., Kobashi, M., Yadroitsava, I., and Yadroitsev, I., 2019, “Topology Optimization and Characterization of Ti6Al4V ELI Cellular Lattice Structures by Laser Powder Bed Fusion for Biomedical Applications,” Mater. Sci. Eng. A, 766(June), p. 138330

[88] Gong, H., Christiansen, D., Beuth, J., & Lewandowski, J. J. (2014). Melt Pool Characterization for Selective Laser Melting of Ti-6Al-4V Pre-alloyed Powder. Solid Freeform Fabrication Symposium, July 2015, 256–267.

[89] Rauniyar, S, & Chou, K. "Transient Melt Pool Formation in Laser-Powder Bed Fusion Process." Proceedings of the ASME 2020 15th International Manufacturing Science and Engineering Conference. Volume 1: Additive Manufacturing; Advanced Materials Manufacturing

[90] Wang, D., Yang, Y., Su, X. & Chen, Y. Study on energy input and its influences on single-track, multi-track, and multi-layer in SLM. Int. J. Adv. Manuf. Technol. 58, 1189–1199 (2012).

[91] I. Yadroitsev, A. Gusarov, I. Yadroitsava, I. Smurov, Single track formation in selective laser melting of metal powders, J. Mater. Proc. Technol., 210, 1624-1631 (2010)

[92] Dilip, J. J. S., Anam, A., Pal, D. & Stucker, B. A short study on the fabrication of single track deposits in SLM and characterization. Solid Free. Fabr. Symp. 1644–1659 (2016).

[93] Gaikwad A, Giera B, Guss GM, Forien JB, Matthews MJ, Rao P. Heterogeneous sensing and scientific machine learning for quality assurance in laser powder bed fusion – A single-track study. Addit Manuf.

[94] Liu B, Wildman R, Tuck C, Ashcroft I, Hague R. Investigaztion the effect of particle size distribution on processing parameters optimisation in selective laser melting process. 22nd Annu Int Solid Free Fabr Symp - An Addit Manuf Conf SFF 2011. 2011;(January):227-238.

[95] Sing SL, Yeong WY. Laser powder bed fusion for metal additive manufacturing: perspectives on recent developments. Virtual Phys Prototyp. 2020;15(3):359-370. doi:10.1080/17452759.2020.1779999/

[96] du Plessis, A., Yadroitsava, I., and Yadroitsev, I., 2018, "Ti6Al4V Lightweight Lattice Structures Manufactured by Laser Powder Bed Fusion for Load-Bearing Applications," Opt. Laser Technol., 108, pp. 521–528.

[97] Lin, K., Yuan, L., and Gu, D., 2019, "Influence of Laser Parameters and Complex Structural Features on the Bio-Inspired Complex Thin-Wall Structures Fabricated by Selective Laser Melting," J. Mater. Process. Technol., 267(November 2018), pp. 34–43.

[98] Calignano, F., Cattano, G., and Manfredi, D., 2018, "Manufacturing of Thin Wall Structures in AlSi10Mg Alloy by Laser Powder Bed Fusion through Process Parameters," J. Mater. Process. Technol., 255(February), pp. 773–783.

[99] Yang, L., Gong, H., Dilip, S., and Stucker, B., 2014, "An Investigation of Thin Feature Generation in Direct Metal Laser Sintering Systems," Proc. 26th Annu. Int. Solid Free. Fabr. Symp., pp. 714–731.

[100] Bidare, P., Bitharas, I., Ward, R. M., Attallah, M. M., and Moore, A. J., 2018, "Fluid and Particle Dynamics in Laser Powder Bed Fusion," Acta Mater., 142, pp. 107–120.

[101] Matthews, M. J., Guss, G., Khairallah, S. A., Rubenchik, A. M., Depond, P. J., and King, W. E., 2017, "Denudation of Metal Powder Layers in Laser Powder-Bed Fusion Processes," Addit. Manuf. Hand b. Prod. Dev. Def. Ind., 114, pp. 677–693

[102] Wu Z, Narra SP, Rollett A. Exploring the fabrication limits of thin-wall structures in a laser powder bed fusion process. Int J Adv Manuf Technol. 2020;110(1-2):191-207. doi:10.1007/S00170-020-05827-4/FIGURES/14

[103] Tomas J, Hitzler L, Köller M, et al. The dimensional accuracy of thin-walled parts manufactured by laser-powder bed fusion process. J Manuf Mater Process. 2020;4(3). doi:10.3390/JMMP4030091

[104] Lu X, Chiumenti M, Cervera M, Tan H, Lin X, Wang S. Warpage analysis and control of thin-walled structures manufactured by laser powder bed fusion. Metals (Basel). 2021;11(5). doi:10.3390/met11050686

[105] Yang T, Xie D, Yue W, Wang S, Rong P, Shen L, Zhao J, Wang C. Distortion of Thin-Walled Structure Fabricated by Selective Laser Melting Based on Assumption of Constraining Force-Induced Distortion. Metals. 2019; 9(12):1281. https://doi.org/10.3390/met9121281

[106] Scipioni Bertoli, U., Wolfer, A. J., Matthews, M. J., Delplanque, J. P. R., and Schoenung, J. M., 2017, "On the Limitations of Volumetric Energy Density as a Design Parameter for Selective Laser Melting," Mater. Des., 113, pp. 331–340.

[107] Martin, A. A., Calta, N. P., Khairallah, S. A., Wang, J., Depond, P. J., Fong, A. Y., Thampy, V., Guss, G. M., Kiss, A. M., Stone, K. H., Tassone, C. J., Nelson Weker, J., Toney, M. F., van Buuren, T., and Matthews, M. J., 2019, "Dynamics of Pore Formation during Laser Powder Bed Fusion Additive Manufacturing," Nat. Commun., 10(1), pp. 1–10.

[108] Rauniyar, S. and K. Chou. Transient Melt Pool Formation in Laser-Powder Bed Fusion Process. in ASME 2020 15th International Manufacturing Science and Engineering Conference. 2020. American Society of Mechanical Engineers Digital Collection.

[109] Shrestha, S. and K. Chou, A study of transient and steady-state regions from single-track deposition in laser powder bed fusion. Journal of Manufacturing Processes, 2021. 61: p. 226-235.

[110] Bertoli, U.S., et al., On the limitations of volumetric energy density as a design parameter for selective laser melting. Materials & Design, 2017. 113: p. 331-340.

[111] J. Li, J. Hu, Y. Zhu, X. Yu, M. Yu, H. Yang, Surface roughness control of root analogue dental implants fabricated using selective laser melting, Additive Manufacturing. 34 (2020) 101283. https://doi.org/10.1016/J.ADDMA.2020.101283.

[112] S. Torres-Carrillo, H.R. Siller, C. Vila, C. López, C.A. Rodríguez, Environmental analysis of selective laser melting in the manufacturing of aeronautical turbine blades, Journal of Cleaner Production. 246 (2020) 119068. https://doi.org/10.1016/J.JCLEPRO.2019.119068.

[113] Z. Sajedi, R. Casati, M.C. Poletti, M. Skalon, M. Vedani, Thermal fatigue testing of laser powder bed fusion (L-PBF) processed AlSi7Mg alloy in presence of a quasi-static

tensile load, Materials Science and Engineering: A. 789 (2020) 139617. https://doi.org/10.1016/J.MSEA.2020.139617.

[114] L. Zhang, B. Song, J.J. Fu, S.S. Wei, L. Yang, C.Z. Yan, H. Li, L. Gao, Y.S. Shi, Topology-optimized lattice structures with simultaneously high stiffness and light weight fabricated by selective laser melting: Design, manufacturing and characterization, Journal of Manufacturing Processes. 56 (2020) 1166–1177. https://doi.org/10.1016/J.JMAPRO.2020.06.005.

[115] M. Mehrpouya, A. Vosooghnia, A. Dehghanghadikolaei, B. Fotovvati, The benefits of additive manufacturing for sustainable design and production, Sustainable Manufacturing. (2021) 29–59. https://doi.org/10.1016/B978-0-12-818115-7.00009-2.

[116] E. Liverani, A.H.A. Lutey, A. Ascari, A. Fortunato, The effects of hot isostatic pressing (HIP) and solubilization heat treatment on the density, mechanical properties, and microstructure of austenitic stainless steel parts produced by selective laser melting (SLM), International Journal of Advanced Manufacturing Technology. 107 (2020) 109–122. https://doi.org/10.1007/S00170-020-05072-9/FIGURES/17.

[117] B. Fotovvati, N. Namdari, A. Dehghanghadikolaei, Fatigue performance of selective laser melted Ti6Al4V components: state of the art, Materials Research Express. 6 (2018) 012002. https://doi.org/10.1088/2053-1591/AAE10E.

[118] Z. Hu, Y. Qi, B. Nagarajan, X. Nie, H. Zhang, H. Zhu, X. Zeng, Top surface roughness evolution during selective laser melting of AlCu5MnCdVA aluminum alloy, Journal of Manufacturing Processes. 64 (2021) 1180–1195. https://doi.org/10.1016/J.JMAPRO.2021.01.051.

[119] T. Yang, T. Liu, W. Liao, E. MacDonald, H. Wei, X. Chen, L. Jiang, The influence of process parameters on vertical surface roughness of the AlSi10Mg parts fabricated by selective laser melting, Journal of Materials Processing Technology. 266 (2019) 26–36. https://doi.org/10.1016/J.JMATPROTEC.2018.10.015.

[120] E. Yasa, J.P. Kruth, J. Deckers, Manufacturing by combining Selective Laser Melting and Selective Laser Erosion/laser re-melting, CIRP Annals. 60 (2011) 263–266. https://doi.org/10.1016/J.CIRP.2011.03.063.

[121] E. Yasa, J. Deckers, J.P. Kruth, The investigation of the influence of laser re-melting on density, surface quality and microstructure of selective laser melting parts, Rapid Prototyping Journal. 17 (2011) 312–327. https://doi.org/10.1108/13552541111156450/FULL/PDF.

[122] C.L.A. Leung, S. Marussi, R.C. Atwood, M. Towrie, P.J. Withers, P.D. Lee, In situ X-ray imaging of defect and molten pool dynamics in laser additive manufacturing, Nature Communications 2018 9:1. 9 (2018) 1–9. https://doi.org/10.1038/s41467-018-03734-7.

[123] C. Qiu, C. Panwisawas, M. Ward, H.C. Basoalto, J.W. Brooks, M.M. Attallah, On the role of melt flow into the surface structure and porosity development during selective laser melting, Acta Materialia. 96 (2015) 72–79. https://doi.org/10.1016/J.ACTAMAT.2015.06.004.

[124] S.A. Khairallah, A.T. Anderson, A. Rubenchik, W.E. King, Laser powder-bed fusion additive manufacturing: Physics of complex melt flow and formation mechanisms of pores, spatter, and denudation zones, Acta Materialia. 108 (2016) 36–45. https://doi.org/10.1016/J.ACTAMAT.2016.02.014.

[125] S.A. Khairallah, A.T. Anderson, A. Rubenchik, W.E. King, Laser powder-bed fusion additive manufacturing: Physics of complex melt flow and formation mechanisms of pores, spatter, and denudation zones, Acta Materialia. 108 (2016) 36–45. https://doi.org/10.1016/J.ACTAMAT.2016.02.014.

[126] J.P. Kruth, L. Froyen, J. van Vaerenbergh, P. Mercelis, M. Rombouts, B. Lauwers, Selective laser melting of iron-based powder, Journal of Materials Processing Technology. 149 (2004) 616–622. https://doi.org/10.1016/J.JMATPROTEC.2003.11.051.

[127] I. Yadroitsev, A. Gusarov, I. Yadroitsava, I. Smurov, Single track formation in selective laser melting of metal powders, Journal of Materials Processing Technology. 210 (2010) 1624–1631. https://doi.org/10.1016/J.JMATPROTEC.2010.05.010.

[128] M.J. Matthews, G. Guss, S.A. Khairallah, A.M. Rubenchik, P.J. Depond, W.E. King, Denudation of metal powder layers in laser powder bed fusion processes, Acta Materialia. 114 (2016) 33–42. https://doi.org/10.1016/J.ACTAMAT.2016.05.017.

[129] Y. Tian, D. Tomus, P. Rometsch, X. Wu, Influences of processing parameters on surface roughness of Hastelloy X produced by selective laser melting, Additive Manufacturing. 13 (2017) 103–112. https://doi.org/10.1016/J.ADDMA.2016.10.010.

[130] F. Attarzadeh, B. Fotovvati, M. Fitzmire, E. Asadi, Surface roughness and densification correlation for direct metal laser sintering, International Journal of Advanced Manufacturing Technology. 107 (2020) 2833–2842. https://doi.org/10.1007/S00170-020-05194-0/FIGURES/6.

[131] K. Mumtaz, N. Hopkinson, Top surface and side roughness of Inconel 625 parts processed using selective laser melting, Rapid Prototyping Journal. 15 (2009) 96–103. https://doi.org/10.1108/13552540910943397/FULL/PDF.

[132] C. Kusuma, S.H. Ahmed, A. Mian, R. Srinivasan, Effect of Laser Power and Scan Speed on Melt Pool Characteristics of Commercially Pure Titanium (CP-Ti), Journal of Materials Engineering and Performance. 26 (2017) 3560–3568. https://doi.org/10.1007/S11665-017-2768-6/FIGURES/15.

CURRICULUM VITAE

Santosh K. Rauniyar

Department of Industrial Engineering
J.B. Speed School of Engineering
University of Louisville
Louisville, KY, 40292

EDUCATION

PhD, Department of Industrial Engineering, University of Louisville, Louisville, KY, USA

Dissertation Title: Experimental and Numerical Studies of Laser Powder-Bed Fusion Process with Ti-6Al-4V Powder: (1) Porosity and Mechanical Properties, and (2) Transient Phenomena in One- and Two-Dimensional Fabrications

Advisor: Dr. Kevin Chou, Professor, Industrial Engineering Department, University of Louisville, KY, USA.

Master of Science, Department of Industrial Engineering, University of Louisville, Louisville, KY, USA

MS Project Title: Study of "Single tracks" deposits in In625 from Laser Powder Bed Fusion Process

Bachelors in Mechanical Engineering, Institute of Engineering, Pulchowk Campus, Lalitpur, Nepal

Undergraduate Project Title: Fabrication and Testing of fiberglass wind turbine blades

RESEARCH EXPERIENCE

01/2020 – 08/2023 **Research Assistant,** University of Louisville

- Designed, fabricated, and analyzed metal AM samples for the study of transient nature in the laser powder bed fusion process (L-PBF) using EOS M270 machine
- Utilized white light interferometer equipment and wrote MATLAB code to study the track geometry and surface height variations in the built parts
- Pioneered research work in quantification of the transient length and transient area for the entire power-scan speed process window of Ti64

- Provided critical information regarding surface roughness, mechanical strength and porosity in fabrication of small length scale structures in the powder bed fusion process
- Developed a model for the powder spreading using discrete element method (DEM) in LIGGGHTS
- Developed a high-fidelity thermo-fluid model using FLOW-3D to explain the transient nature of the L-PBF process in short scans
- Study of the single tracks and raster area scan and three dimensional structures

- Designed and fabricated samples to investigate the surface characteristics of raster scans in multiple process parameters conditions
- In depth explanation about different scenarios that is responsible for the surface roughness variations

08/2017 – 12/2019 **Graduate Assistant**, University of Louisville

- Quantitative study of single tracks geometry of IN625 fabricated with and without powder particles
- Conducted non-destructive (micro-ct) and destructive (metallography) tests on the sample
- Explained the transition window from conduction mode to keyhole mode and quantified the track geometry for the tracks fabricated with and without powder particles.
- Porosity analysis of tensile samples using micro-ct technique.
- Part of a broader research work that provided insights into fabricating high strength samples without porosity defects.
- Study of change in pore morphology of tensile sample after fracture and qualitative comparison of porosity before and after fracture
- Provided insights into the pore size range that is critical to the failure of the samples
- Developed a model for random powder generation and powder bed distribution
- Created user defined function in ANSYS Fluent for thermo-fluid simulation
- Predicted the change in the melt pool dynamics with different powder size distribution and corroborated with the experimental result
- Fabrication of the dendrite structure and dimensional accuracy comparison using Coordinate measuring machine

WORK EXPERIENCE

11/2012 – 07/2017 CAE Engineer, E&T Nepal Pvt. Ltd., E&T Co., Ltd. (Thailand) and E&T Co. Ltd. (Japan)

- Worked in the capacity of project team leader in collaboration with Yachiyo Industry Co. Ltd. Japan
- Project - Wind Throb Noise Analysis in partially open cavity using Lagrangian method to optimize the noise from sunroof of an automobile
- Worked in the capacity of project team leader in collaboration with Yachiyo Industry Co. Ltd. Japan
- Aerodynamic design optimization of a various components of a Paralympic wheelchair including helmet, tires, handle and the entire wheelchair
- Aerodynamic study of a Paralympic Wheelchair (1/3 scaled prototype) using Particle Image Velocimetry
- Official trainer on mathematical modeling and simulation software operation and development at E&T Co. Ltd. Japan
- Worked in the capacity of sub-leader in two projects in collaboration with HONDA R&D Asia Pacific Co. Ltd. (HRAP), Bangkok, Thailand
- Development of Synchronized Physical and Virtual Software for (i) Cabin Duct Design and Cabin Air Temperature Optimization and (ii) Defroster Duct Design optimization and front glass defrosting correlation
- Utilized Lagrangian approach to develop an in-house solver and validated the simulation results with the experimental results

REFERRED JOURNAL ARTICLES

1. **Rauniyar S.**, Chou K., 2019. Melt Pool Analysis and Mesoscale Simulation of Laser Powder Bed Fusion Process (L-PBF) with Ti-6Al-4V Powder Particles. *Jom*. Pp.938-945.
2. Zhang S., **Rauniyar S.**, Shrestha S., Ward A., and Chou, K., 2019. An experimental study of tensile property variability in selective laser melting. *Journal of Manufacturing Processes*.
3. Shrestha S., **Rauniyar S**., and Chou K., 2019. Thermo-Fluid Modeling of Selective Laser Melting: Single-Track Formation Incorporating Metallic Powder. *Journal of Materials Engineering and Performance*, *28*(2), pp.611-619.
4. Lane B., Zhirnov I., Mekhontsev S., Grantham S., Ricker R., **Rauniyar S.,** and Chou K., 2020. Transient Laser Energy Absorption, Co-axial Melt Pool Monitoring, and Relationship to Melt Pool Morphology. *Additive Manufacturing*.
5. Fotovvati B., **Rauniyar S**., Arnold JA., and Chou K., 2022. Experimental, Computational, and Data-Driven Study of the Effects of Selective Laser Melting

(SLM) Process Parameters on Single-Layer Raster Scanning Surface Characteristics. *The International Journal of Advanced Manufacturing Technology*

REFERRED CONFERENCE PROCEEDINGS

1. **Rauniyar S.**, and Chou K., 2019, November. Porosity analysis and pore tracking of metal AM tensile specimen by Micro-CT. In *Proceedings of 2019 International Solid Freeform Fabrication Symposium*.
2. **Rauniyar S.**, and Chou K., 2020, November. Transient Melt Pool Formation in Laser-Powder Bed Fusion Process. In *Proceedings of International Manufacturing Science and Engineering Conference,* MSEC2020-8345
3. **Rauniyar S.**, Shrestha S., and Chou K., 2022, An Investigation Into Multi-Track Deposition in Laser Powder-Bed Fusion: Transient Regions Analysis and Scan Length Effects. *In Proceedings of the ASME 2022 17th International Manufacturing Science and Engineering Conference,* MSEC2022-85746
4. Le Trong-Nhan**, Rauniyar S.**, V H Nismath., and Chou K., 2022, An Investigation Into Multi-Track Deposition in Laser Powder-Bed Fusion: Transient Regions Analysis and Scan Length Effects. *51st SME North American Manufacturing Research Conference*

PRESENTATIONS

1. Poster presentation on *"Melt pool analysis and meso-scale simulation of laser powder bed fusion process (L-PBF)"* in Speed Research Exposition (2018)
2. Oral presentation *on "Melt pool analysis and meso-scale simulation of laser powder bed fusion process (L-PBF)"* in Kentucky Nano + AM symposium (2018)
3. Poster presentation on "*Study of "Single tracks" deposits in Inconel 625 from Laser Powder Bed Fusion Process"* in Speed Research Exposition (2019)
4. Poster presentation on *"Porosity Analysis and Pore Tracking of Tensile Specimen by Micro-CT*" in ASME MSEC (2019)
5. Virtual Presentation on *"3d Transient Zone In Conduction And Keyhole Mode Melting In Laser Powder Bed Fusion Process"* in International Solid Freeform Fabrication Symposium. (2021)
6. Poster presentation on*" Investigation of Transient Region and Scan Length Effect in Powder Bed Fusion Process"* in NNCI NANO + AM Summit (2022)

AWARDS

- National Science Foundation Student Travel award to attend Manufacturing Science and Engineering Conference in 2019.
- NAMRC 49 / MSEC 2021 NSF Student Support Award
- Graduate Student Council Travel Award for 2019 and 2021 annual international solid freeform fabrication symposium
- College Fellow Scholarship and Freeship recipient during Bachelor's in Mechanical Engineering at Pulchowk Campus, Lalitpur, Nepal.

ACTIVITIES

- Mentored undergraduate students on the optical profiler, micro-ct and other equipment in the lab (2020-2022)
- Reviewed two journal papers for Optics and Laser Technology
- Secretary of the Nepalese Student Association, University of Louisville for two calendar years (2018/2019)